

EXCLUSIVE PRODUCTION OF QUARKONIA AND GENERALIZED PARTON DISTRIBUTIONS

A Dissertation
Submitted to
the Temple University Graduate Board

In Partial Fulfillment
of the Requirements for the Degree of
Doctor of Philosophy

by
John Paul Koempel
May, 2015

Examining Committee Members:

Andreas Metz, Advisory Chair, Department of Physics
Theodore Burkhardt, Department of Physics
Zein-Eddine Meziani, Department of Physics
Peter Riseborough, Department of Physics
Leonard Gamberg, External Member, Physics Department, Penn State Berks

ABSTRACT

The understanding of the nucleon is as of yet not complete. In particular, the contribution of the gluon content is not well understood. Utilizing the framework of Generalized Parton Distributions enables predictions to be made if some information on them is known. We investigated exclusive photo and electroproduction of heavy vector mesons (the quarkonia J/ψ and Υ), which can give access to the currently poorly constrained gluon distribution E^g . For this reason, we implemented a model for it with several variants in order to represent a spread of plausible distributions. We used current experimental results for exclusive ϕ and ρ^0 production to test our variants for E^g . For quarkonium production, the analytic calculation of the Leading Order production amplitudes was performed, verifying results published previously, in particular confirming that in the non-relativistic collinear approximation there is no access to the polarized or gluon helicity flip distributions, i.e. \tilde{H}^g and H_T^g . Numerical results for both the Leading Order and, in the case of photoproduction, also Next-to-Leading Order amplitudes were calculated, based on our Leading Order amplitudes and already existing Next-to-Leading Order expressions. The observables we looked at are the unpolarized cross section, spin density matrix elements, and two spin-asymmetries — the transverse single-spin asymmetry A_N , and a newly discussed double-spin asymmetry A_{LS} , which we identified as a very promising observable for measuring E^g . We find that in the case of J/ψ photoproduction higher order corrections seem not well under control, while for Υ production the numerical results become much more stable.

To Melissa
my love, my life, my all

ACKNOWLEDGEMENTS

I am a man of few words, and there have been many individuals who have helped me through my academic journey. Therefore, I will extend a personal "thank you" to only a few — those who have given the most help and support.

First, I would never be where I am without my amazing family. From the beginning, my parents, John and Ann, have always been there for me and helped to shape me into the man I am today. I also would like to thank my sisters, Annie and Debbie, who have always helped to keep me grounded. Special thanks goes to my wife Melissa, who has always been at my side and has never lost faith in me, and my son Everett, who has shown me more joy than I thought possible.

On the more academic side of things, all the professors I came into contact with during my time at Temple have helped me to become a better scientist. I will finish with thanking my advisor Andreas, who has helped me through countless struggles and pushed me to perform better in all my pursuits. Without his consistent guidance and immense patience, this work would not exist.

TABLE OF CONTENTS

	Page
ABSTRACT	ii
DEDICATION	iii
ACKNOWLEDGEMENTS	iv
LIST OF TABLES	vii
LIST OF FIGURES	x
1 INTRODUCTION	1
2 GENERALIZED PARTON DISTRIBUTIONS	6
2.1 Background	6
2.2 Encoded Information	11
2.2.1 Form Factors	11
2.2.2 Spin Sum Rule	12
2.2.3 Impact Parameter Space	13
2.3 Evolution	14
2.4 Models for E^g	15
3 VECTOR MESON PRODUCTION AND GPDS	22
3.1 Background	22
3.2 Kinematics	23

	vi
3.3 Production Amplitudes	24
3.3.1 Leading Order	24
3.3.2 Next to Leading Order	34
3.3.3 Light Mesons	37
4 OBSERVABLES: ANALYTICAL RESULTS	40
4.1 Cross Sections	40
4.2 Spin Density Matrix Elements	41
4.3 Asymmetries	45
4.4 Next to Leading Order	48
4.5 Light Mesons	48
5 OBSERVABLES: NUMERICAL RESULTS	49
5.1 GPDs and Evolution	49
5.2 Next to Leading Order	52
5.3 Production Amplitudes	55
5.4 Cross Sections	66
5.5 Spin Density Matrix Elements	75
5.6 Asymmetries	80
6 CONCLUSION	90
BIBLIOGRAPHY	94
A MODELING H	98
B SPINOR ALGEBRA	100
C NEXT TO LEADING ORDER	103
C.1 Gluon Amplitude	103
C.2 Quark Amplitude	113

LIST OF TABLES

Table	Page
2.1 Gluon and sea quark model parameters	19
5.1 Results for the SSA A_N for ϕ electroproduction	80
5.2 Results for A_N for ρ^0 production, integrated over t	81
5.3 Results for A_N for ρ^0 production for a single kinematic point	81
A.1 Parameters of q_{val}^a , q^s , and g at the scale $\mu = 2$ GeV	99

LIST OF FIGURES

Figure	Page
2.1 Graphical representation of the correlators for gluon and quark GPDs. . . .	7
2.2 5 GPD variants, including H^g	16
2.3 The five GPD variants for E^g , along with H^g , at the initial scale.	20
2.4 Distribution of gluons in impact parameter space at $x = 0.005$	21
2.5 Distribution of gluons in impact parameter space at $x = 0.1$	21
3.1 One of the 6 diagrams describing the LO gluon contribution to exclusive quarkonium production.	25
3.2 The 6 possible leading order subprocess amplitudes	26
3.3 Two example diagrams showing the emission of a soft gluon from the on-shell antiquark line in the subprocess	35
3.4 An example of the quark exchange NLO contribution at the level of the full process	35
3.5 The LO quark exchange diagram for production of light vector mesons . . .	38
5.1 LO and NLO non-flip amplitudes for production of a J/ψ , separated into real and imaginary components.	56
5.2 Imaginary and Real parts of the NLO non-flip amplitude for J/ψ photoproduction	57
5.3 LO and NLO spin-flip amplitudes for production of a J/ψ	58
5.4 Imaginary and Real parts of the NLO spin-flip amplitude for J/ψ photoproduction	59

5.5	Effect of chosen variant on LO spin-flip amplitudes for J/ψ photoproduction	60
5.6	Effect of chosen variant on NLO spin-flip amplitudes for J/ψ photoproduction	61
5.7	LO and NLO non-flip amplitudes for production of a Υ	62
5.8	Imaginary and Real parts of the NLO non-flip amplitude for Υ photoproduction	63
5.9	LO and NLO spin-flip amplitudes for production of a Υ	64
5.10	Imaginary and Real parts of the NLO spin-flip amplitude for Υ photoproduction	64
5.11	Effect of chosen variant on LO spin-flip amplitudes for Υ photoproduction .	65
5.12	Effect of chosen variant on NLO spin-flip amplitudes for Υ photoproduction	65
5.13	LO and NLO results for J/ψ photoproduction at $t = 0$	66
5.14	LO and NLO results for J/ψ photoproduction at 3 different t values	67
5.15	Differential J/ψ electroproduction as a function of cm-energy for 3 different values of t	68
5.16	LO differential cross section results for J/ψ production as a function of Q^2 at $W = 90$ GeV and 4 different values of t	69
5.17	LO and NLO differential cross section results for photoproduction as a function of $-t$	70
5.18	Differential J/ψ photoproduction as a function of the momentum transfer to the nucleon at $W = 90$ GeV, for 3 different values of photon virtuality . .	71
5.19	LO and NLO integrated cross section results for J/ψ photoproduction . . .	72
5.20	LO integrated cross section results for J/ψ production at 4 different values of Q^2	73
5.21	LO integrated cross section results for J/ψ electroproduction as a function of Q^2	73
5.22	LO and NLO integrated cross section results for photoproduction of Υ as a function of W	74
5.23	W dependence of two SDMEs for which there is experimental data available	75

5.24	Q^2 dependence of five SDMEs for which there is experimental data available	78
5.25	t dependence of five SDMEs for which there is experimental data available	79
5.26	LO and NLO SSA A_N results for J/ψ photoproduction as a function of W	82
5.27	LO and NLO DSA A_{LS} results for J/ψ photoproduction as a function of W	83
5.28	LO and NLO SSA A_N results for J/ψ photoproduction as a function of t	84
5.29	LO and NLO DSA A_{LS} results for J/ψ photoproduction as a function of t	85
5.30	A_N and A_{LS} results for J/ψ production as a function of Q^2	86
5.31	LO and NLO SSA A_N results for Υ photoproduction as a function of W	87
5.32	LO and NLO DSA A_{LS} results for Υ photoproduction as a function of W	88
5.33	LO and NLO SSA A_N results for Υ photoproduction as a function of t	89
5.34	LO and NLO DSA A_{LS} results for Υ photoproduction as a function of t	89

CHAPTER 1

INTRODUCTION

The search for knowledge about what makes up the universe has been a focus of mankind for thousands of years, though sometimes theory has considerably outpaced experiment. The concept of atoms, for example, where matter can be broken down only so far, was originally proposed thousands of years ago in ancient Greece. While these atoms didn't have much relation to what we think of as atoms today, the idea formed the groundwork of more modern atomic theories. It wasn't until the early 1800s when John Dalton used the concept of atoms to explain why elements always react in ratios of small whole numbers that we start to approach our modern understanding. At this time, atoms were still thought to be indivisible, however. It took almost another hundred years until J. J. Thomson discovered the electron and came to the conclusion that they were a part of every atom [1]. As time has progressed, we've gotten better and better at smashing apart the building blocks of the universe to see what's inside. The present time is very exciting — we have technology capable not only of investigating what's inside atoms, but also what makes up these atomic constituents.

It became obvious that atoms had an internal, and often complex structure, consisting of electrons orbiting a much larger nucleus [2]. This nucleus was determined to be made up of protons and neutrons, collectively referred to as nucleons [3]. In the 1950s, advances in nuclear physics lead to experiments generating many never before seen particles; so many, in fact, that questions began to arise as to how they could be organized and classified. In the early 1960s, a new theory positing additional, smaller, building blocks was

developed [4–7]. These building blocks were termed quarks, and they were originally considered as largely mathematical objects, as opposed to real particles which could be freely observed [5]. They did a very good job at sorting the so-called "particle zoo," however there was still a problem. The observed Δ^{++} baryon had to be made of 3 up quarks with parallel spins, but this combination should have been forbidden by the Pauli exclusion principle. The solution to this dilemma was that the quarks also had to carry an additional quantum number [8, 9], which was eventually termed color. By the late 1960s there was experimental evidence that protons had an internal structure [10, 11]. This gave credence to the idea that quarks were not mere abstract concepts, but actual particles. The quarks in a nucleon interact with each other through the exchange of gluons, the force carriers of the strong interaction. This interaction is described by Quantum Chromodynamics (QCD), the generally accepted microscopic theory of the strong interaction, which was discovered in the early 1970s [12, 13].

One important aspect of QCD is that of factorization. This importance can best be seen in analogy to Quantum Electrodynamics (QED), which studies the interaction of electrically charged particles (such as electrons) and photons, the carrier of the electromagnetic force. In QED, computations can be performed perturbatively; because the coupling constant is small ($\alpha \approx 1/137$ for small scales, and only increasing slightly at larger ones) it can be used as an expansion parameter. In QCD, on the other hand, the coupling (α_s) becomes sufficiently weak only at high energies/scales, such that, as a matter of principle, perturbative calculations are possible only for high-energy processes or reactions involving a particle with a heavy mass. This suppression of the coupling constant at large scales depends on an aspect of the theory known as asymptotic freedom [14–17]. The minimum required energy scale for perturbative calculations in QCD to become meaningful is about the mass of the nucleon or in other words 1 GeV. One has to keep in mind though that even for high energies many scattering processes cannot be computed completely in perturbative QCD. The reason is that in those processes there is still sensitivity to non-perturbative physics. However, often QCD factorization allows one to separate the (calculable) perturbative part of the cross section from the non-perturbative component [18]. It is not

guaranteed for any given process to be able to be factorized; however, in many common processes factorization does indeed hold.

One set of objects that are used to parameterize the non-perturbative part of a process are the ordinary parton distribution functions (PDFs). These functions appear in many processes, such as deep inelastic scattering, where a high energy lepton interacts with a proton (for example), and transfers enough energy such that the proton is broken apart. PDFs can give us some idea of the internal structure of the nucleon, but in only one dimension. Generally, when talking about PDFs, we think about them in terms of a nucleon which has a large momentum. They can give the distribution of the longitudinal momenta carried by the partons in the nucleon. This is nice, but even better would be if we could gather some additional information about the nucleon structure. Since nucleons are three-dimensional objects, we want to know more about the partons than PDFs can give. In other words, we want a full three-dimensional picture of the inside of a nucleon.

One way of getting this additional information is via generalized parton distributions (GPDs). They have been considered an important development for about the past 2 decades [19–25] and can help us understand more about the nucleon than simple PDFs can. GPDs give us information about where the partons are located, in effect giving us a look at a transverse slice of the nucleon [26]. They can also give us information about the angular momenta of partons, which enter into the spin sum rule for the nucleon, which describes how the angular momentum and spin of quarks and gluons can generate the total nucleon spin of $1/2$ [20]. Besides being able to use factorization to separate the GPD from the perturbative interaction, GPDs are convenient because they are universal. Besides being able to use factorization to separate the GPD from the perturbative interaction, GPDs are known to be universal in those processes where they appear after factorization. Generally, universality means that the same non-perturbative objects appear in more than one process, which allows cross checks and, in particular, also gives predictive power. In the case of GPDs, for example, experiments investigating deep-virtual Compton scattering (DVCS) off the nucleon can give us insight into the same GPDs that we have in hard exclusive meson production (HEMP). In the present work we also make use of universality since

we take the unpolarized gluon GPD H^g , which was fitted to data for light vector meson production, in order to compute quarkonium production.

Chapter 2 contains information regarding the GPDs. Additional detail is given regarding these objects, beginning with some background information including useful notation and the actual definitions of the GPDs relevant in this work. More explicit information regarding the usefulness of GPDs follows this discussion, detailing some of the information we can glean from them. Additionally, there is another aspect of GPDs that hasn't been discussed so far — they also depend on a renormalization scale which is typically set to be on the order of the general energy/mass scale of the process. This scale dependence can be computed in QCD, order by order in perturbation theory. The resulting LO evolution equations have been solved [19], and a code which computes the evolution quickly has also been developed [27]. In this chapter we discuss our models for the GPD E^g , numerically evolve both H^g and E^g , and discuss the contribution of E^g to the nucleon spin sum rule and the transverse imaging of the nucleon [28]. Our models for E^g will later, in Chapter 5, be confronted with experimental data for the transverse target spin asymmetry for light vector meson production.

Chapter 3 introduces the process we investigate in order to access the GPDs — exclusive photo- and electroproduction of vector mesons off the proton. We address specifically the J/ψ and Υ mesons. These are both heavy mesons, which will give us the hard scale that we need to factorize the process. The J/ψ meson consists of a charm and anti-charm quark bound together, while the Υ is a bottom anti-bottom bound state. The investigated process has been considered useful for probing the gluonic structure of the nucleon for some time now [29,30], since it is very clean, especially at leading order (LO) in perturbation theory, where only the gluon exchange is pertinent. For the leading order calculation we confirm existing results according to which, in the non-relativistic approximation for the vector meson, only the GPDs H^g and E^g can be addressed [31]. There is no sensitivity to the remaining six leading twist gluon GPDs, neither for photo- nor for electroproduction. We additionally discuss the next-to-leading order (NLO) corrections applicable to photoproduction of quarkonia [32]. Finally, we give the results for electroproduction of

light vector mesons which we use later on for our numerics.

In Chapter 4, we obtain analytical results for the observables we investigate in terms of helicity amplitudes for the process. The first observable we have been interested in is the unpolarized cross section for the process. We also look at spin-density matrix elements that have been measured for unpolarized J/ψ production at HERA. While in general those observables give additional information, it turns out that in our LO calculation they merely depend on kinematical factors and have no sensitivity to the GPDs. If one wants to get real sensitivity to the GPD E^g one has to look at transverse target polarization. For this reason, we turn to two asymmetries; first, the transverse single-spin asymmetry A_N (also referred to as A_{UT}), in which the target polarization is transverse (or normal) to the reaction plane; second, a (new) double spin asymmetry [28], A_{LS} , where the target is longitudinally polarized, and the outgoing nucleon is transversely polarized ("sideways" in the reaction plane). Searching for an alternative to the "classic" A_N for addressing E^g was motivated by the numerical results from the LO calculation.

In Chapter 5, we present details of the numerical calculations performed. Some information regarding the computer code and procedure for numerically evolving the GPDs is given, along with some discussion of nontrivial issues which had to be overcome. Additionally, details regarding the computation of the NLO corrections are also presented. One of our main findings is that in the case of J/ψ , at least for photo-production, the perturbative expansion does not seem to converge very well. For the cross section this general result was already obtained previously [32]. Somewhat surprisingly even the aforementioned spin asymmetries are also not stable upon inclusion of higher order corrections. The situation clearly improves for Υ production.

This work ends with a series of Appendices, giving information useful to the reader, but not necessary to include in the main body. First, Appendix A details how the GPD H is modeled, which is similar to that of E . Then, Appendix B introduces the spinor algebra used in the definitions of the GPDs. Finally, Appendix C presents in explicit detail a number of equations needed for the numerical computation of the NLO terms for photo-production.

CHAPTER 2

GENERALIZED PARTON DISTRIBUTIONS

2.1 Background

While GPDs give us more information than PDFs, the trade-off is that they also depend on a larger number of variables. PDFs depend only on the longitudinal momentum fraction, x . This parameter describes the fraction of the nucleon's momentum that the active parton possesses. GPDs explicitly depend not only on this quantity (which acquires a slightly different meaning), but also two others — the so-called skewness ξ , and the invariant momentum transfer to the hadron t ; we can then write $F = F(x, \xi, t)$, for an unspecified GPD F . When taken together, x and ξ describe the momentum fraction of the active parton, see Fig. 2.1; the skewness and invariant momentum transfer are given by

$$\xi = \frac{p^+ - p'^+}{p^+ + p'^+}, \quad t = (p' - p)^2. \quad (2.1)$$

where p and p' are the 4-momenta of the initial and final nucleon, and we have used light-cone coordinates

$$a^\pm = \frac{1}{\sqrt{2}} (a^0 \pm a^3) \quad \mathbf{a} = (a^1, a^2), \quad (2.2)$$

for a generic 4-vector a . While ξ can lie in the region $[-1, 1]$, known processes in which we can measure GPDs are limited to non-negative ξ [25]. As a matter of convenience, we also

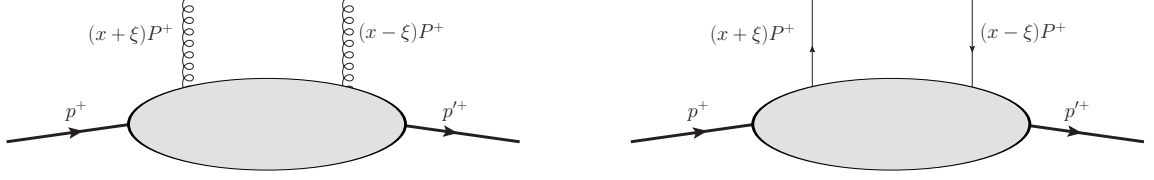


Figure 2.1: Graphical representation of the correlators for gluon (left) and quark (right) GPDs. The plus momenta of the initial and final hadron and parton are indicated, where we use $P = (p + p')/2$. The shaded oval regions represent spectator partons and their interaction.

define the 4-vectors

$$P = \frac{p + p'}{2}, \quad \Delta = p' - p \quad (2.3)$$

which then leads to a more compact definition for the skewness

$$\xi = -\frac{\Delta^+}{2P^+}. \quad (2.4)$$

In addition to the explicit dependence on x , ξ , and t , GPDs also depend on a renormalization scale, μ . We discuss this dependence in more detail in Section 2.3.

GPDs are defined as matrix elements of quark and gluon operators; following the conventions in [25, 33], we can define the unpolarized quark and gluon distributions for the case where the parton helicity does not change:

$$\begin{aligned} F^q &= \frac{1}{2} \int \frac{dz^-}{2\pi} e^{ixP^+z^-} \left\langle p'(\nu') \left| \bar{q} \left(-\frac{1}{2}z \right) \gamma^+ q \left(\frac{1}{2}z \right) \right| p(\nu) \right\rangle_{|z^+=0, \mathbf{z}=0} \\ &= \frac{1}{2P^+} \left[H^q(x, \xi, t) \bar{u}(p') \gamma^+ u(p) + E^q(x, \xi, t) \bar{u}(p') \frac{i\sigma^{+\alpha} \Delta_\alpha}{2m} u(p) \right] \end{aligned} \quad (2.5)$$

$$\begin{aligned} F^g &= \frac{1}{P^+} \int \frac{dz^-}{2\pi} e^{ixP^+z^-} \left\langle p'(\nu') \left| G^{+\mu} \left(-\frac{1}{2}z \right) G_\mu^+ \left(\frac{1}{2}z \right) \right| p(\nu) \right\rangle_{|z^+=0, \mathbf{z}=0} \\ &= \frac{1}{2P^+} \left[H^g(x, \xi, t) \bar{u}(p') \gamma^+ u(p) + E^g(x, \xi, t) \bar{u}(p') \frac{i\sigma^{+\alpha} \Delta_\alpha}{2m} u(p) \right], \end{aligned} \quad (2.6)$$

where we have specified the helicities ν and ν' for the initial and final nucleon, respectively.

We additionally include the definitions for the "polarized" gluon GPDs

$$\begin{aligned}\tilde{F}^g &= \frac{1}{P^+} \int \frac{dz^-}{2\pi} e^{ixP^+z^-} \left\langle p'(\nu') \left| G^{+\mu} \left(-\frac{1}{2}z \right) \tilde{G}_\mu^+ \left(\frac{1}{2}z \right) \right| p(\nu) \right\rangle_{|z^+=0, \mathbf{z}=0} \\ &= \frac{1}{2P^+} \left[\tilde{H}^g(x, \xi, t) \bar{u}(p') \gamma^+ \gamma_5 u(p) + \tilde{E}^g(x, \xi, t) \bar{u}(p') \frac{\gamma_5 \Delta^+}{2m} u(p) \right],\end{aligned}$$

and the parton helicity flip GPDs [25]

$$\begin{aligned}\frac{1}{P^+} \int \frac{dz^-}{2\pi} e^{ixP^+z^-} \left\langle p'(\nu') \left| \mathbf{S} G^{+i} \left(-\frac{1}{2}z \right) G^{j+} \left(\frac{1}{2}z \right) \right| p(\nu) \right\rangle_{|z^+=0, \mathbf{z}=0} \\ = \mathbf{S} \frac{1}{2P^+} \frac{P^+ \Delta^j - \Delta^+ P^j}{2mP^+} \bar{u}(p') \left[H_T^g(x, \xi, t) i\sigma^{+i} + \tilde{H}_T^g \frac{P^+ \Delta^i - \Delta^+ P^i}{m^2} \right. \\ \left. + E_T^g \frac{\gamma^+ \Delta^i - \Delta^+ \gamma^i}{2m} + \tilde{E}_T^g \frac{\gamma^+ P^i - P^+ \gamma^i}{m} \right] u(p),\end{aligned}$$

where \mathbf{S} indicates symmetrization of uncontracted Lorentz indices and removal of the trace. The GPDs are valid in the range $-1 \leq x \leq 1$, which can be broken into three regions depending on what the values of x and ξ are (we use quark exchange as an example) [25]:

- 1.) $\xi \leq x \leq 1$: Since both momentum fractions ($x + \xi$ and $x - \xi$) are positive, this corresponds to emission and reabsorption of a quark.
- 2.) $-\xi \leq x \leq \xi$: The first momentum fraction ($x + \xi$) is positive, corresponding to quark emission, while the second ($x - \xi$) is negative, which can be understood as the emission of an antiquark from the initial nucleon.
- 3.) $-1 \leq x \leq -\xi$: Both momentum fractions are now negative, so we have the emission and reabsorption of antiquarks.

The definitions in Eqs. (2.5) and (2.6) can be simplified by performing the spinor algebra; the details of which can be found in Appendix B. This algebra results in the following expressions for the case of the initial and final nucleon having the same helicity, along with the case of their helicities being opposite (flipped):

$$F_{++} = F_{--} = \sqrt{1 - \xi^2} \left[H - \frac{\xi^2}{1 - \xi^2} E \right] \quad (2.7)$$

$$F_{+-} = -[F_{-+}]^* = \frac{\sqrt{t_0 - t}}{2m} E, \quad (2.8)$$

where t_0 is the minimal value of t ,

$$t_0 = -\frac{4\xi^2 m^2}{1 - \xi^2}. \quad (2.9)$$

These relations hold for both the quark and the gluon GPDs. Since typical values of ξ are small, it is clear that if we want to get more information on E , and in particular E^g , then it is useful to obtain information on the nucleon helicity flip term.

The number of relevant GPDs can be reduced somewhat based on parity constraints and whether the helicity of the nucleon changes. As an example we can take the process we investigate, and which will be described in detail in Chapter 3, $\gamma + p \rightarrow V + p'$, where V represents a vector meson. At leading order only two GPDs enter — H and E , and only the ones describing gluons, since only gluon exchange is relevant. At next-to-leading order (NLO) the quark versions of H and E also enter the calculation, whereas they are only needed at LO if evolution is taken into account. The evolution equations in this case mix the gluon and quark GPDs (as will be seen later), so if we want to evolve the gluon distributions, we must also know the quark distributions.

We already have a decent amount of information about the GPD H , for both quarks and gluons. This is due to the fact it has a number of constraints, e.g. PDFs and nucleon form factor data. Additionally, at small x_B — the fraction of the nucleon's momentum that the active parton carries, ρ^0 and ϕ production are dominated by H , allowing all other GPDs to be ignored [34]. On the other hand, things are not so certain for E , especially for gluons. There is no possible form factor information, and it is largely suppressed in the cross section. Spin asymmetries seem to be the main source of information for E^g , and what little data currently exists for this is characterized by large error bars.

We can consider the forward limit of GPDs; to do so, we take the case of the skewness and invariant momentum transfer being zero; in this limit, the GPDs H reduce to their respective PDFs, e.g. $H^q(x, 0, 0) = q(x)$. Things are not quite so simple for the other GPDs.

Other important properties are the polynomiality and symmetry relations for GPDs. The polynomiality requirement is rooted in Lorentz invariance and requires the x integrals of the quantities $x^n H$ and $x^n E$ to be polynomials in ξ , of order $n + 1$, e.g. [24]

$$\begin{aligned} \int_{-1}^1 x^N H^q(x, \xi) dx &= h_0^{q(N)} + h_2^{q(N)} \xi^2 + \dots + h_{N+1}^{q(N)} \xi^{N+1} \\ \int_{-1}^1 x^N E^q(x, \xi) dx &= e_0^{q(N)} + e_2^{q(N)} \xi^2 + \dots + e_{N+1}^{q(N)} \xi^{N+1} \end{aligned} \quad (2.10)$$

Besides this, the coefficients for the highest power in the series are related, $e_{N+1}^{q(N)} = -h_{N+1}^{q(N)}$. The result of this is that if we look at the combination $H + E$, we are left with a polynomial of order n instead of $n + 1$. The double distribution method which we use satisfies this requirement automatically.

The symmetry relations which hold for a change in sign of x are simpler for gluons than they are for quarks since gluons are their own antiparticles — H^g and E^g are both even functions in x . The quark GPDs, on the other hand, in general are neither even nor odd, but there are two combinations that are useful, the so-called singlet and non-singlet combinations given, respectively, by:

$$\begin{aligned} H^{q(+)} &= H^q(x, \xi, t) - H^q(-x, \xi, t) \\ H^{q(-)} &= H^q(x, \xi, t) + H^q(-x, \xi, t). \end{aligned} \quad (2.11)$$

The singlet combination is the one which enters into the evolution equations governing the gluon evolution. Therefore, this is the one which enters into our calculations; the two combinations are generally found in different processes, and there is no mixing between them during evolution. Time reversal invariance also leads to a set of simple relations [25]:

$$H(x, -\xi, t) = [H(x, \xi, t)]^* = H(x, \xi, t), \quad (2.12)$$

for both quarks and gluons, and with the same relations also holding for E . These relations

can be obtained by going to the matrix element definition of the GPDs, Eqs. (2.5) and (2.6). Changing the sign of ξ is reasonable, since time reversal would switch the initial and final momenta, leading to an overall sign change in the definition of ξ , Eq. (2.1). The result of these relations is that the GPDs are fully real valued.

2.2 Encoded Information

GPDs were born from the desire to learn more about the nucleon than the existing theory allowed. Processes such as virtual Compton scattering and meson production were found to be useful in this venture. PDFs, as has already been mentioned, were developed to learn about the momentum of the partons inside the nucleon. Another quantity which was, and still is, commonly used in nucleon studies are the nucleon form factors. These quantities can tell us about the distribution of electric and magnetic densities. GPDs, in some ways, supersede these other measurements; however, GPDs do not replace them completely, as it can be easier to measure the PDFs or form factors, especially depending on the processes available. In this way, measurements of the PDFs and form factors can help to constrain GPDs, and vice versa.

There are a few other quantities that GPDs can give us more information about. One application of GPDs has to do with learning about the angular momentum of the partons in the nucleon. This is useful for determining how the spin of the nucleon is generated. There is evidence that besides the valence quarks, gluons also play a sizable role in generating the nucleon spin [28,35–37]. GPDs can also be used to build a picture of the distribution of partons in transverse, or impact parameter, space. This can help to give us insight into how the quarks are arranged inside the nucleon, and what factor gluons play in the nucleon's internal structure.

2.2.1 Form Factors

If we integrate the GPDs over the variable x , we get a quantity that is dependent only on t , the invariant momentum transfer. Specifically, if we take H^q and E^q , we get the Dirac and

Pauli form factors:

$$\int_{-1}^1 dx H^q(x, \xi, t) = F_1^q(t) \quad \text{and} \quad \int_{-1}^1 dx E^q(x, \xi, t) = F_2^q(t); \quad (2.13)$$

which are defined for each separate quark flavor. Analogous relations hold also for the gluon GPDs and form factors, which means that knowledge about the distributions leads directly to knowledge regarding the form factors. This in turn helps us to learn more about the nucleon's structure, since these can be used to determine the electric and magnetic form factors,

$$G_E = F_1 - \frac{Q^2}{4m^2} F_2 \quad \text{and} \quad G_M = F_1 + F_2, \quad (2.14)$$

where F_1 and F_2 are obtained by summing the individual quark form factors.

2.2.2 Spin Sum Rule

Another interest in GPDs stems from the fact that they can be exploited to garner information about the makeup of the nucleon spin, as noted in [20]. Originally, it was expected that the spin of the constituent quarks was the only thing that determined the spin of the nucleon. It was determined through muon scattering, however, that the quark intrinsic spin actually contributed very little to the nucleon spin [38]. The understanding now is that the nucleon contains not only quarks, but also gluons, and they are both able to move around inside the nucleon. Thus, the actual spin of the quarks are not the only contributing factors, but also the orbital angular momentum of both the quarks and gluons. In other words, the total nucleon spin should be the sum of the total quark and gluon angular momenta, i.e. $\frac{1}{2} = \sum_q J^q + J^g$. For the proton, there is some evidence that the valence quarks, particularly the up quarks, play a large role in generating the proton spin (see, e.g. [37]). As previously mentioned, gluons may also have a large contribution to the spin, which makes them an important object of study. We can calculate the angular momentum of the

gluons inside the nucleon in terms of the gluon GPDs through

$$J^g = \frac{1}{2} \int_0^1 dx \left(H^g(x, \xi, 0) + E^g(x, \xi, 0) \right). \quad (2.15)$$

Clearly, if we want to have a more accurate idea of the contribution from the gluon angular momentum, we need information on not just H^g , but also E^g . Since this information is currently lacking, there is quite a bit of uncertainty inherent in any prediction of J^g .

2.2.3 Impact Parameter Space

Since we know that the nucleon is an extended object, we can ask how the constituent partons are arranged. Fortunately, GPDs can be used to obtain information about the impact parameter (b_\perp) space of the nucleon. This can give us a look at a "slice" of the nucleon, and tell us if the partons are clumped together in the center, as in analogy to the nucleus of an atom, or more spread out, as the atomic electrons tend to be.

In order to access this information, we must transform the GPDs to impact parameter space through their Fourier transforms. This gives us \mathcal{H}^g and \mathcal{E}^g , which we use in order to determine the density of partons in impact parameter space for a nucleon with transverse polarization (along the X direction) [39]. If we insert the appropriate operator between states which are superpositions of the positive and negative helicities, we obtain

$$\mathcal{H}^{g,X}(x, \mathbf{b}_\perp) = \int \frac{d^2 \Delta_\perp}{(2\pi)^2} e^{-i \Delta_\perp \cdot \mathbf{b}_\perp} \left[H^g(x, 0, -\Delta_\perp^2) + i \frac{\Delta_y}{2m} E^g(x, 0, -\Delta_\perp^2) \right]. \quad (2.16)$$

We notice that this leaves us with the Fourier transforms of the two GPDs H^g and E^g . Some slight rewriting gives us the following result,

$$\mathcal{H}^{g,X}(x, \vec{b}_\perp) = \mathcal{H}^g(x, \vec{b}_\perp^2) - \frac{b_\perp^Y}{m} \frac{\partial}{\partial \vec{b}_\perp^2} \mathcal{E}^g(x, \vec{b}_\perp^2). \quad (2.17)$$

Just as in the case of the angular momentum due to gluons, this result will also be fairly unconstrained, due to the range of possibilities for E^g , and thus also \mathcal{E}^g .

2.3 Evolution

Another aspect of GPDs is that of evolution. GPDs depend also on the factorization scale of the process, μ . Evolving the GPDs is a nontrivial exercise. Sometimes, therefore, instead of applying the full evolution rules to the GPDs, it is instead taken into account in an approximate way, for example, through a scale dependent term in the PDF model, c.f. [37,40–42].

For this work, the GPDs have been evolved numerically, according to the evolution equations [25]:

$$\begin{aligned} & \mu^2 \frac{d}{d\mu^2} \begin{pmatrix} (2n_f)^{-1} \sum_q^{n_f} H^{q(+)}(x, \xi, t) \\ H^g(x, \xi, t) \end{pmatrix} \\ &= \int_{-1}^1 dx' \frac{1}{|\xi|} \begin{pmatrix} V^{qq} \left(\frac{x}{\xi}, \frac{x'}{\xi} \right) & \frac{1}{\xi} V^{qg} \left(\frac{x}{\xi}, \frac{x'}{\xi} \right) \\ \xi V^{gq} \left(\frac{x}{\xi}, \frac{x'}{\xi} \right) & V^{gg} \left(\frac{x}{\xi}, \frac{x'}{\xi} \right) \end{pmatrix} \begin{pmatrix} (2n_f)^{-1} \sum_q^{n_f} H^{q(+)}(x, \xi, t) \\ H^g(x, \xi, t) \end{pmatrix}, \end{aligned} \quad (2.18)$$

where V refers to the evolution kernels. These are complicated expressions, and including them here would not provide additional insight. If interested, the kernels are readily available, see for instance [27,43]. In order to perform the evolution calculations, we utilize the routine developed by Vinikov [27], which produces acceptable results while also being fairly fast computationally. Since the quark singlet and the gluon GPDs mix under evolution (note the V^{qg} and V^{gq} terms) we need GPDs for the valence and sea quarks along with the gluons.

GPD evolution can be broken up into two regions, which evolve the GPDs differently. The two regions are each named in connection with the evolution equations which govern the GPDs there. Specifically, in the forward limit of $\xi \rightarrow 0$, we obtain the DGLAP equation, which was developed separately by Dokshitzer, Gribov and Lipatov, and Altarelli and Parisi [44–47]; it governs the evolution of parton densities. The ERBL equation is recovered

in the limit $\xi \rightarrow \pm 1$ and was established by Efremov and Radyushkin, and Brodsky and Lepage [48,49]; it describes the evolution of meson distribution amplitudes. Based on these limits, we denote the region $\xi \leq |x|$ as DGLAP, and $\xi \geq |x|$ as ERBL.

In this work, we utilize a code which is able to quickly evolve the GPDs while keeping the precision at an appropriate level [27]. We begin with an initial scale of $\mu_0 = 2.0$ GeV, and evolve the distributions to a scale appropriate for the process, viz. $\mu = \sqrt{Q^2 + m_V^2}$. Plots showing the GPDs at three scales — the initial scale, the mass of the J/ψ and the mass of the Υ , are shown in Fig. 2.2. Though it may not be noticeable in the plots, it is worth noting that Variant 1, which started at zero, contains a node once evolved to larger scales.

2.4 Models for E^g

As mentioned previously, there is already a good amount of information regarding the distributions H^q and H^g . We exploit this wealth of information by using models that have already been developed [41,42]. These models utilize the double distribution method of constructing the GPDs. We use this same basic method for E^g ; however, there is much less information known about this distribution. There are two constraints, but even when taking them into account, there is still a very large amount of uncertainty left in E^g . We focus here on the model for E ; the specifics of modeling H can be found in Appendix A. The double distribution approach models the GPDs through [50]

$$F^i(x, \xi, t) = \int_{-1}^1 d\beta \int_{-1+|\beta|}^{1-|\beta|} d\alpha \delta(\beta + \xi\alpha - x) f^i(\beta, \alpha, t) \quad (2.19)$$

$$f^i(\beta, \alpha, t) = F^i(|\beta|, 0, 0) e^{bt} |\beta|^{-\alpha't} \frac{\Gamma(2n_i + 2)}{2^{2n_i+1} \Gamma^2(n_i + 1)} \frac{[(1 - |\beta|)^2 - \alpha^2]^{n_i}}{(1 - |\beta|)^{2n_i+1}}. \quad (2.20)$$

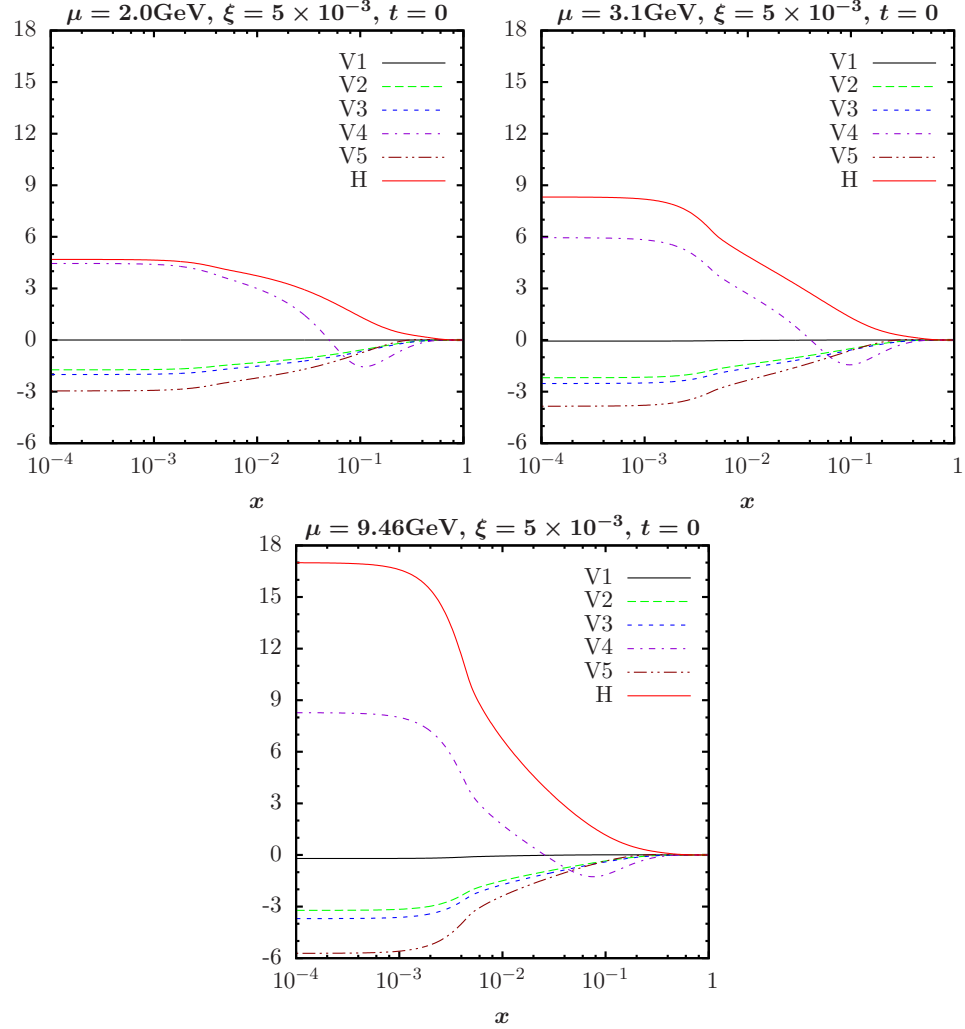


Figure 2.2: 5 GPD variants (see Table 2.1), including H^g , at the initial scale of 2 GeV (top left), evolved to the J/ψ mass (top right), and evolved to the Υ mass (bottom center).

The variable n depends on which GPD we are interested in, with $F^i(|\beta|, 0, 0)$ and n given by [41, 51]

$$\begin{aligned}
 E_{val}^q(|\beta|, 0, 0) &= e^{val}(\beta) & n_{val} &= 1 \\
 E_{sea}^q(|\beta|, 0, 0) &= e^{sea}(\beta) & n_{sea} &= 2 \\
 E^g(|\beta|, 0, 0) &= |\beta| e^g(\beta) & n_g &= 2.
 \end{aligned}
 \tag{2.21}$$

These values of n are chosen to yield the asymptotic forms for quark and gluon distribution amplitudes. This is not unreasonable, since one can view the α dependence as similar to a meson distribution amplitude. Similarly, the dependence of the double distribution on β

should appear similar to a parton density.

For the valence quarks, E^q is based on analysis of the Dirac and Pauli form factor data for the proton [52, 53] and is given by

$$E_{\text{val}}^a(x, 0, 0) = N_a \kappa_a x^{-\alpha_{\text{val}}(0)} (1-x)^{\beta_{\text{val}}^a} (1 + \gamma_q \sqrt{x}). \quad (2.22)$$

The normalization factor, N_a , is calculated according to

$$\int_0^1 dx e_a^q(x) = \kappa_a \quad (2.23)$$

The parameters as determined in [37, 52, 53] are

$$\begin{aligned} \kappa_u = 1.67 & & \kappa_d = -2.03 & & \gamma_u = 4 & & \alpha_{\text{val}}(0) = 0.603 & & (2.24) \\ \beta_{\text{val}}^u = 4.65 & & \beta_{\text{val}}^d = 5.25 & & \gamma_d = 0 & & & & \end{aligned}$$

While β_{val}^u and β_{val}^d do have some freedom and result in reasonable fits to the data, the values repeated here give the best fit [53].

For the gluons and sea quarks, we use:

$$e^g(x) = \begin{cases} N^g x^{-1-\delta_e} (1-x)^{\beta_e^g} \\ N^g x^{-1-\delta_e} (1-x)^{\beta_e^g} \tanh(1-x/x_0) \end{cases} \quad (2.25)$$

$$e^s(x) = N^s x^{-1-\delta_e} (1-x)^{\beta_e^s}. \quad (2.26)$$

The two gluon variations are similar to the model used for H , but the second one has a node, located at $x = x_0$. The case of a node being present is not currently ruled out (see, for example, contribution by M. Diehl in [54]), and in fact, when evolved to higher scales, Variant 1 (in which E^g is initially zero) actually develops a node. We take a flavor symmetric sea, so at the initial scale, all the sea quark distributions are equal ($e^{\bar{q}} \equiv e^{\bar{u}} = e^{\bar{d}} = e^{\bar{s}} = e^s$).

There are two main constraints used in fixing the parameters of e^g and $e^{\bar{q}}$. The first one

is obtained by combining the momentum sum rule for unpolarized parton distributions with Ji's spin sum rule. This gives us

$$e_{20}^g = - \sum_q e_{20}^{qval} - 2 \sum_q e_{20}^{\bar{q}}, \quad (2.27)$$

$$\text{where } e_{n0}^i \equiv \int_0^1 dx x^{n-1} e^i(x). \quad (2.28)$$

The other constraint is a positivity bound which is derived from the density interpretation of GPDs in the impact parameter space [39]; for an exponential t dependence of the double distributions, described by the profile functions for E^i and H^i respectively:

$$\begin{aligned} g_s &= g_g = b_g^e - \alpha'_g \log x \\ f_s &= f_g = b_g - \alpha'_g \log x, \end{aligned} \quad (2.29)$$

the bounds are [37]:

$$\begin{aligned} \frac{\left(e^s(x)\right)^2}{\left(s(x)\right)^2 - \left(\Delta s(x)\right)^2} &\leq 4 m_n^2 e^{1+\log 2} \left[\frac{g_s(x)}{f_s(x)}\right]^3 [f_s(x) - g_s(x)] \\ \frac{\left(e^g(x)\right)^2}{\left(g(x)\right)^2 - \left(\Delta g(x)\right)^2} &\leq 4 m_n^2 e^{1+\log 2} \left[\frac{g_g(x)}{f_g(x)}\right]^3 [f_g(x) - g_g(x)]. \end{aligned} \quad (2.30)$$

By combining the profile functions and the bounds, we can find [37]

$$\begin{aligned} \beta_e^i &\geq 6 & b_g^e &< b_g \\ \delta_e &\leq \delta_h & \alpha'_e &< \alpha'_h \end{aligned} \quad (2.31)$$

There are no other constraints on the value of b_g^e , so we follow [37, 55] and use a value of $b_g^e = 0.9 b_g$, with b_g given by Eq. (A.4). We take values of $\beta_e^g = 6$, $\beta_e^s = 7$, and $\delta_e = 0.1$. Of the relations for b_g^e and α'_e in Eq. (2.31), one could actually be an equality instead. We exploit this fact by exploring both possibilities for our choice of α'_e , which, in part, distinguishes our variants from one another, see Table 2.1. To determine the normalization

Var.	α'_e	N^g	x_0	e_{20}^g	J^g	$N^{\bar{q}}$	$2J^{\bar{q}}$
1	0.15	0		0	0.214	-0.042	0.008
2	0.15	-1.050		-0.196	0.116	0.156	0.041
3	0.10	-1.189		-0.222	0.103	0.182	0.045
4	0.10	3.526	0.05	-0.222	0.103	0.182	0.045
5	0.10	-2.308	0.3	-0.222	0.103	0.182	0.045

Table 2.1: Gluon and sea quark model parameters. All parameters are for e^g and $e^{\bar{q}}$ at the scale $\mu = 2 \text{ GeV}$. For gluons, the Variants 1,2,3 refer to the first ansatz in (2.25), while Variants 4,5 refer to the second. Also shown is the second moment e_{20}^g , and values for the angular momenta as defined in (2.15).

constants N^s and N^g , we first choose our parameters β_e, b_e, δ_e , and α'_e . We then saturate the positivity bound for the strange quarks, and finally utilize the momentum sum rule to determine the gluon normalization, which is then checked to be sure that it also satisfies the positivity bound.

The GPDs at the initial scale can be seen in Fig. 2.3. From the plot, it can be seen that the magnitude of the normalization parameter N^g has a direct influence on the magnitude of the GPD itself, which is understandable if we remember that the ansatz depends on this normalization directly. We also point out that the location of the node has a large effect on the size of the GPD as well. This aspect comes directly from the constraints placed on E^g — since the positivity constraints (2.30) depend on the forward distributions, this behavior is also expected.

The second moments and the angular momentum contribution of the gluons and sea quarks to the nucleon spin are also able to be seen in Table 2.1. We see that the nodal variants preserve both these quantities. This is just what we expect, since the first step in obtaining the gluon normalization is to use the positivity constraint to normalize the sea quark distribution. Once that is done, we then go to the momentum sum rule, and determine what value the second moment of the forward gluon distribution must be to satisfy it. Only then are we able to calculate the gluon normalization. This results in the fact that the sea quark parameterization should not be taken lightly, since it has such a large effect on that of the gluon.

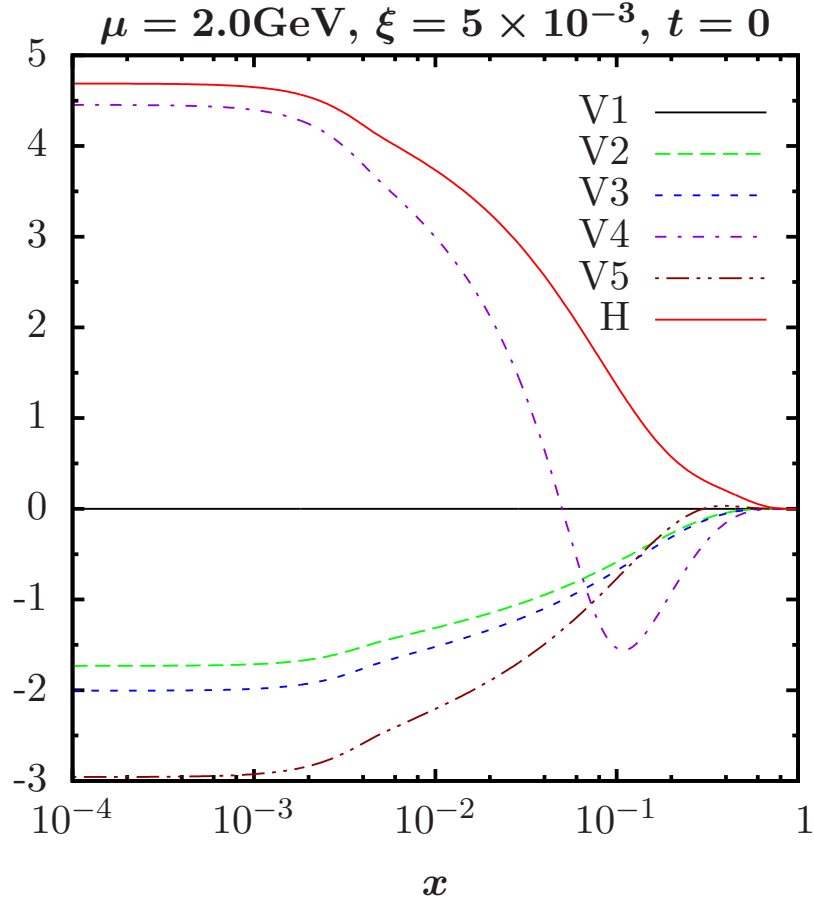


Figure 2.3: The five GPD variants for E^g , along with H^g , at the initial scale.

We can now use the variants to take a look at how the distribution of gluons in impact parameter space of a transversely polarized nucleon (see Eq. (2.17)) changes based on our variants. Figures 2.4 and 2.5 show this distribution for two of them, Variant 2 and Variant 4. These two were chosen to represent a range of possible parameterizations for E^g ; Variant 2 represents a very small, non-zero, contribution from E^g , while Variant 4 represents a large one. We can see that since Variant 2 has such a small contribution, the center of the distribution is shifted away from zero only a very small amount, while Variant 4 results in a much larger shift. Less noticeable is the fact that the shape of the distribution for Variant 4 is less circular than Variant 2. It is interesting to note that according to Figs. 2.4 and 2.5, the gluons are not evenly distributed throughout the nucleon, but instead are concentrated near the center, with a shift determined by the size of E^g .

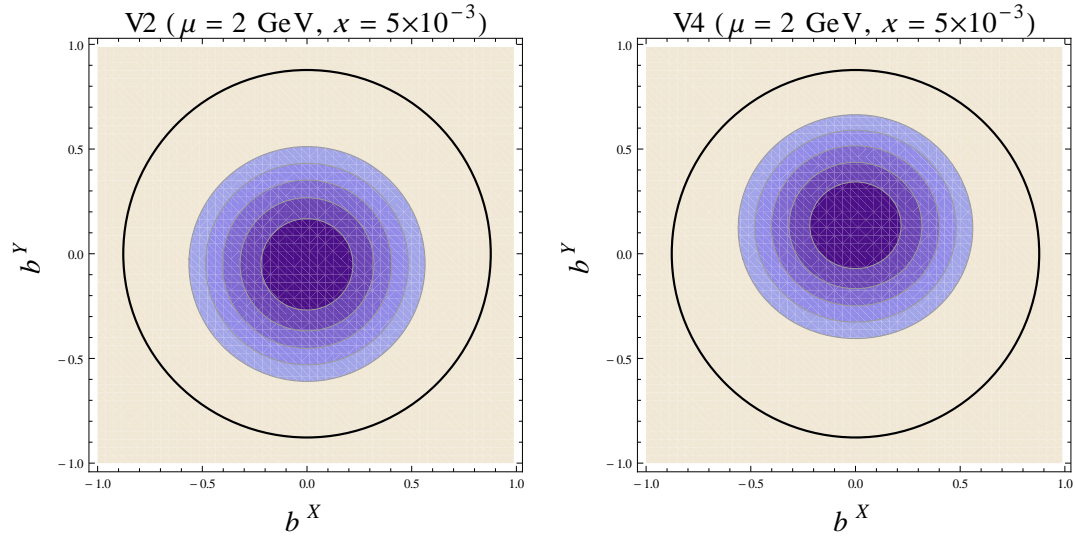


Figure 2.4: Distribution of gluons in impact parameter space of the nucleon for Variant 2 (left) and Variant 4 (right). They are plotted at our initial scale of $\mu = 2 \text{ GeV}$, and $x = 0.005$. The outer contour ring denotes half of the maximum density, and the final ring denotes the approximate size of the proton.

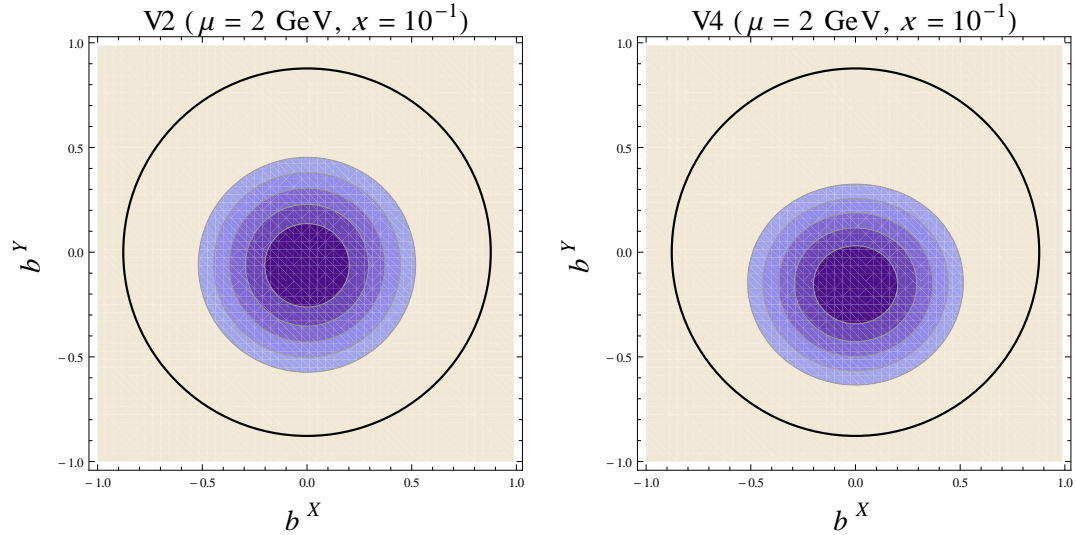


Figure 2.5: Distribution of gluons in impact parameter space of the nucleon for Variant 2 (left) and Variant 4 (right). They are plotted at our initial scale of $\mu = 2 \text{ GeV}$, and $x = 0.1$. The outer contour ring denotes half of the maximum density, and the final ring denotes the approximate size of the proton.

CHAPTER 3

VECTOR MESON PRODUCTION AND GPDs

3.1 Background

As mentioned in Chapter 1, GPDs appear in two processes: Deep Virtual Compton Scattering (DVCS) and hard exclusive meson production. Since we are most interested in advancing knowledge of the gluon distribution, the more useful process is that of Meson Production. Specifically, we explore exclusive vector meson production, focusing efforts on the J/ψ , but also investigating Υ and ϕ production – the former since the results should be better under control, and the latter due to the amount of experimental data already available.

Hard exclusive meson production is investigated based on its usefulness for our purposes. Specifically, the fact that the gluon exchange is dominant — at LO, quark exchange does not enter at all. The result of this situation is that at LO, information regarding the gluon GPDs appear by themselves in any observables, i.e. it is not necessary to separate gluon and quark GPDs in the observables.

If we want to access the GPDs, factorization must hold for our process, $\gamma^{(*)}p \rightarrow Vp$. An all order proof of factorization for this process has been shown in the case of Q^2 being much larger than all other scales in the process [56]. It can be expected for factorization to hold in quarkonium production even at arbitrary values of Q^2 , if the mass of the quark can provide a sufficiently large scale; NLO photoproduction calculations are consistent with factorization [32].

3.2 Kinematics

In order to be precise, the investigated process is

$$\gamma^{(*)}(q, \mu) + p(p, \nu) \rightarrow V(q', \mu') + p'(p', \nu'), \quad (3.1)$$

with the specified 4-momenta and helicities. Additionally, we use $Q^2 = -q^2$, $m^2 = p^2 = p'^2$, $m_V^2 = q'^2$, $t = (p - p')^2$, and $W^2 = (p + q)^2$, where t is the squared invariant momentum transfer from the nucleon, and W is the photon-nucleon center of mass energy. The skewness is written as

$$\xi = \frac{\tilde{x}_B}{2 - \tilde{x}_B}, \quad \text{with} \quad \tilde{x}_B = \frac{m_V^2 + Q^2}{W^2 + Q^2}. \quad (3.2)$$

Expressing the skewness in this way makes more clear its dependence on our kinematic variables, and applies equally to both photo and electroproduction. It is worth noting that at large Q^2 , $m_V \ll Q^2$, one has $\tilde{x}_B \rightarrow x_B$, which yields the well-known result $\xi = \frac{x_B}{2 - x_B}$ for the case of HEMP of light vector mesons. We also introduce a notation denoting the difference between t and its minimum, $t' = t - t_0$.

We take the meson mass to be twice that of the heavy quark mass, $m_V = 2m_q$, in accordance with the non-relativistic approximation. Another aspect of this approximation is that the quark-antiquark pair which makes up the bound quarkonium state each share equally in the meson's momentum, i.e. they each have the same momentum fraction, τ . Additionally, we employ the collinear approximation, where we neglect any transverse momentum. This is not unreasonable, given that we work in a frame where the objects have large momenta in a given direction. Since we work with light-cone coordinates, we take the case of the nucleon having a large positive momentum, with the photon and produced meson having large negative momenta. We can relate the photon and meson momenta by using conservation of momentum,

$$p + q = p' + q'; \quad (3.3)$$

additionally, the definition of ξ , Eq. (2.1), allows us to rewrite the nucleon momenta, $p^+ = (1 + \xi)P^+$ and $p'^+ = (1 - \xi)P^+$, where $P = (p + p')/2$. We can also find that $q^- \approx q'^-$. From this result, we can also determine a useful expression for the meson's momentum in the plus direction,

$$\begin{aligned} q'^2 &= m_V^2 \\ 2q'^+ q'^- &= m_V^2 \\ q'^+ &= \frac{m_V^2}{2q'^-} = \frac{m_V^2}{2q^-} \end{aligned} \tag{3.4}$$

Likewise, $q^+ = -\frac{Q^2}{2q^-}$; obviously, in photoproduction, the photon has no component of momentum in the positive light cone direction. The meson and nucleon, on the other hand, due to their nonzero masses, do have a positive component.

3.3 Production Amplitudes

Since we work with heavy quarks in the production of quarkonium, and there is negligible intrinsic content of these quarks in the nucleon, only the gluon exchange can contribute at LO. Light quark exchange does not enter until NLO.

3.3.1 Leading Order

At leading order the production amplitudes can be written down fairly easily from the relevant Feynman diagrams, see Fig. 3.1. In the figure, the bottom blob is parameterized by the gluon GPD, while the upper blob is governed by the meson distribution amplitude. In order to determine the production amplitudes for each diagram, we start by first considering the subprocess,

$$\gamma^{(*)}(q, \mu) + g(k_1, \lambda) \rightarrow V(q', \mu') + g'(k_2, \lambda'). \tag{3.5}$$

If we take Fig. 3.1, but this time focus on the subprocess, we obtain Fig. 3.2. We note that although there are a total of 6 diagrams, we will see later that only 3 of them are

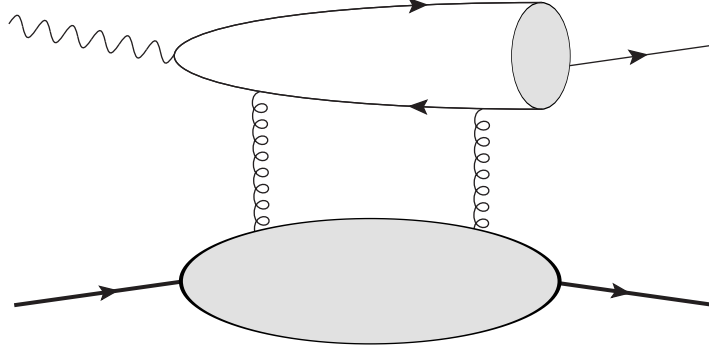


Figure 3.1: One of the 6 diagrams describing the LO gluon contribution to exclusive quarkonium production.

independent – each row in Fig. 3.2 denotes an independent result.

Since there are only 3 unique diagrams which contribute to the subprocess amplitude, it suffices to calculate the 3 independent amplitudes and double the resulting expression. There are a few things that go into calculating the amplitudes; the method we follow can be summarized into 4 steps:

1. Determine the propagator denominators for each diagram
2. Determine the trace results for each diagram
3. Combine the trace, denominator, and other prefactors from each diagram
4. Add the results together to obtain the final subprocess amplitude

Since each row in Fig. 3.2 generates a unique result, we calculate amplitudes for diagrams A, C, and E, then simply double our results. Utilizing the momenta given in (3.5), we can calculate the propagator denominators for each of the two quark propagators using the usual expression, $l^2 - m_q^2$, where l is the momentum of the relevant propagator. We are also able to simplify the resulting denominators somewhat by using the momenta of the external lines, along with the fact that we are working in the non-relativistic approximation, so that we have $\tau = 1/2$. We show an example of the denominator calculations for diagram A, where the momenta of the quark and antiquark are given by $\tau q'$ and $-\bar{\tau} q'$, respectively. We have used the notation $\bar{\tau} = 1 - \tau$; since the non-relativistic approximation

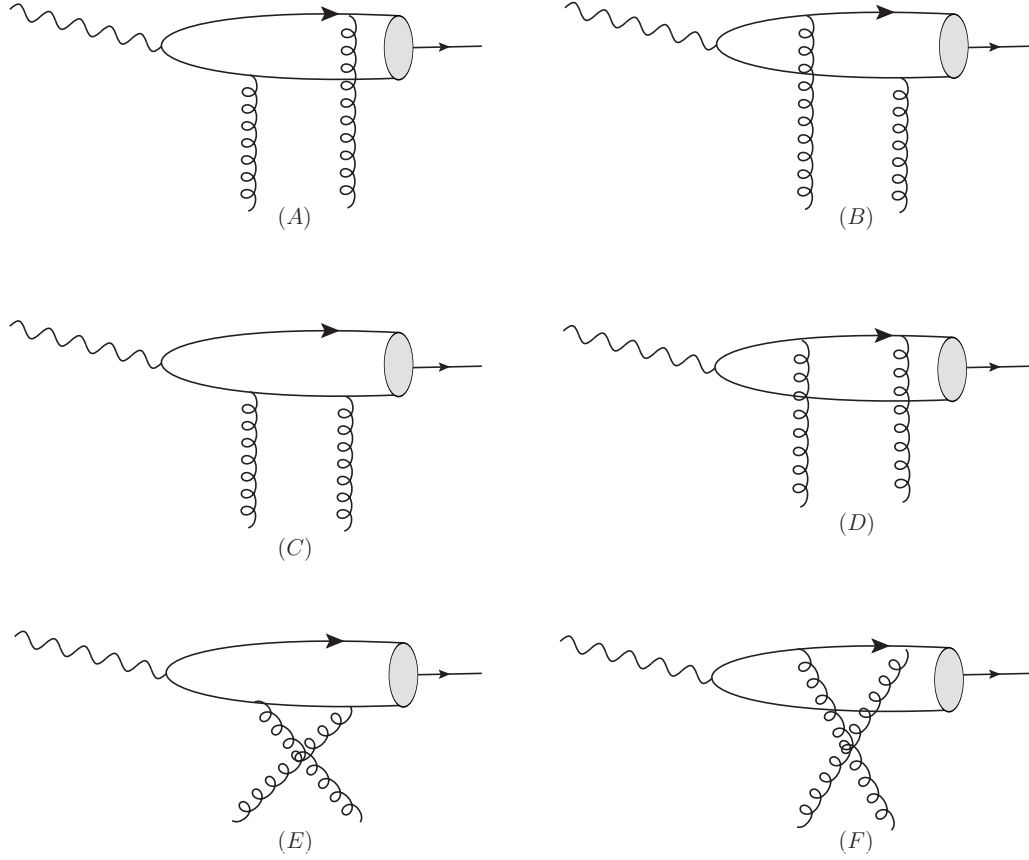


Figure 3.2: The 6 possible leading order subprocess amplitudes. The two diagrams in each row contribute an identical result to the amplitude.

requires $\tau = \bar{\tau}$, and $\tau + \bar{\tau} = 1$, we must have $\tau = 1/2$. The bottom quark propagator is

$$\begin{aligned}
 l^2 - m_q^2 &= (-\bar{\tau}q' + k_1)^2 - m_q^2 \\
 &= m_q^2 - 2\bar{\tau}q' \cdot k_1 - m_q^2 \\
 &= -2\bar{\tau}q' \cdot k_1 \\
 &= -\frac{1}{4\xi}(x + \xi)(m_V^2 + Q^2),
 \end{aligned} \tag{3.6}$$

and the top one can be calculated as

$$\begin{aligned}
l'^2 - m_q^2 &= (l + q)^2 - m_q^2 = (-\bar{\tau}q' + k_1 + q)^2 - m_q^2 \\
&= m_q^2 - Q^2 - 2\bar{\tau}q' \cdot k_1 + 2j' \cdot q + 2k_1 \cdot q - m_q^2 \\
&= -Q^2 - 2\bar{\tau}q' \cdot k_1 - 2\bar{\tau}q' \cdot q + 2k_1 \cdot q \\
&= -Q^2 + 2\tau q \cdot k_1 - 2\bar{\tau}q' \cdot q \\
&= -Q^2 + 2\tau \frac{1}{4\xi}(x + \xi)(m_V^2 + Q^2) - 2\bar{\tau} \frac{1}{2}(m_V^2 - Q^2) \\
&= \frac{1}{4\xi}(x + \xi)(m_V^2 + Q^2) - \frac{1}{2}(m_V^2 - Q^2) - Q^2 \\
&= \frac{1}{4\xi}(x + \xi)(m_V^2 + Q^2) - \frac{1}{2}(m_V^2 + Q^2) \\
&= \frac{1}{4\xi}(x - \xi)(m_V^2 + Q^2).
\end{aligned} \tag{3.7}$$

The other denominator calculations follow a similar process, the final results are

$$\begin{aligned}
\text{for diagrams A,B:} & \left[\frac{1}{4\xi}(x - \xi)(m_V^2 + Q^2) \right] \left[-\frac{1}{4\xi}(x + \xi)(m_V^2 + Q^2) \right] \\
\text{for diagrams C,D:} & \left[\frac{1}{4\xi}(x - \xi)(m_V^2 + Q^2) \right] \left[-\frac{1}{2}(m_V^2 + Q^2) \right] \\
\text{for diagrams E,F:} & \left[-\frac{1}{4\xi}(x + \xi)(m_V^2 + Q^2) \right] \left[-\frac{1}{2}(m_V^2 + Q^2) \right]
\end{aligned} \tag{3.8}$$

We can now move on to point 2, the calculation of the pertinent traces for each diagram. Each one involves the polarization vectors of the external lines, in addition to the propagator and meson momenta (and masses). Each diagram has a slightly different permutation

of polarizations/momenta, which we show below,

$$\begin{aligned}
A &= \text{Tr} \left[\not{\epsilon}_V^* (\not{q}' + m_V) \not{\epsilon}_2 (-\bar{\tau} \not{q}' + \not{k}_1 + \not{q} + m_q) \not{\epsilon}_\gamma (-\bar{\tau} \not{q}' + \not{k}_1 + m_q) \not{\epsilon}_1 \right] \\
B &= \text{Tr} \left[\not{\epsilon}_V^* (\not{q}' + m_V) \not{\epsilon}_1 (\tau \not{q}' - \not{k}_1 + m_q) \not{\epsilon}_\gamma (\tau \not{q}' - \not{k}_1 - \not{q} + m_q) \not{\epsilon}_2 \right] \\
C &= \text{Tr} \left[\not{\epsilon}_V^* (\not{q}' + m_V) \not{\epsilon}_\gamma (\tau \not{q}' - \not{q} + m_q) \not{\epsilon}_1 (\tau \not{q}' - \not{q} - \not{k}_1 + m_q) \not{\epsilon}_2 \right] \\
D &= \text{Tr} \left[\not{\epsilon}_V^* (\not{q}' + m_V) \not{\epsilon}_2 (-\bar{\tau} \not{q}' + \not{q} + \not{k}_1 + m_q) \not{\epsilon}_1 (-\bar{\tau} \not{q}' + \not{q} + m_q) \not{\epsilon}_\gamma \right] \\
E &= \text{Tr} \left[\not{\epsilon}_V^* (\not{q}' + m_V) \not{\epsilon}_\gamma (\tau \not{q}' - \not{q} + m_q) \not{\epsilon}_2 (\tau \not{q}' - \not{q} - \not{k}_2 + m_q) \not{\epsilon}_1 \right] \\
F &= \text{Tr} \left[\not{\epsilon}_V^* (\not{q}' + m_V) \not{\epsilon}_1 (-\bar{\tau} \not{q}' + \not{q} + \not{k}_2 + m_q) \not{\epsilon}_2 (-\bar{\tau} \not{q}' + \not{q} + m_q) \not{\epsilon}_\gamma \right]
\end{aligned} \tag{3.9}$$

We see that if we compare the traces corresponding to the two diagrams in each row of Fig. 3.2, one can be obtained from the other through two simple exchanges. First, we exchange the propagator momentum terms while changing the signs of the 4-vectors, and second we exchange the second polarization vector with the final one. This symmetry can be seen fairly easily from the diagrams, as well. One is able to decompose each of the above expressions according to powers of mass, which simplifies things somewhat, since one is then left with traces of an odd number of gamma matrices. Another method, which was taken here, is to use the computer algebra system, FORM [57]; this allows us to quickly compute the traces for the various possible helicities.

We also must provide the scalar products that arise from computing the traces. First, let us specify our polarization vectors, where \pm refers to positive or negative helicity, and 0 refers to a longitudinally polarized particle;

$$\begin{aligned}
\varepsilon_g^\pm &= -\frac{1}{\sqrt{2}}(0, \pm 1, i, 0) \\
\varepsilon_{\gamma/V}^\pm &= -\frac{1}{\sqrt{2}}(0, \mp 1, i, 0)
\end{aligned} \tag{3.10}$$

$$\begin{aligned}
\varepsilon_\gamma^0 &= \frac{1}{Q}(q^3, 0, 0, q^0) \\
\varepsilon_V^0 &= \frac{1}{m_V}(q^3, 0, 0, q'^0)
\end{aligned} \tag{3.11}$$

The longitudinal polarization vectors obey certain normalization conditions, viz

$$(\varepsilon_\gamma^0)^2 = 1 \quad (\varepsilon_V^0)^2 = -1 \quad (3.12)$$

And the nonzero polarization products are given by

$$\begin{aligned} \varepsilon_\gamma^\pm \cdot \varepsilon_V^\mp &= 1 & \varepsilon_g^\pm \cdot \varepsilon_g^\mp &= 1 \\ \varepsilon_\gamma^\pm \cdot \varepsilon_g^\pm &= 1 & \varepsilon_g^\pm \cdot \varepsilon_V^\pm &= 1, \end{aligned} \quad (3.13)$$

where ε_g denotes either of the two gluons. Additionally, we note that the conjugate of the transverse polarization vectors (which occur when we have a particle in the final state) obey

$$(\varepsilon^\pm)^* = -\varepsilon^\mp. \quad (3.14)$$

Obviously, if we have the product of a transverse and longitudinal polarization vector, or a transverse polarization vector and a momentum vector, the result is 0, since we neglect transverse motion of the particles, and the longitudinal polarization vectors have no transverse component. There are, however, additional products which we need to be aware of. We specify the following scalar product results (assuming that the subprocess momentum transfer $\hat{t} = 0$):

$$\begin{aligned} \varepsilon_\gamma^0 \cdot \varepsilon_M^0 &= -\frac{1}{2Qm_V} (m_V^2 - Q^2) & \varepsilon_\gamma^0 \cdot k_1 &= -\frac{1}{4\xi Q} (x + \xi) (m_V^2 + Q^2) \\ \varepsilon_\gamma^0 \cdot k_2 &= -\frac{1}{4\xi Q} (x - \xi) (m_V^2 + Q^2) & \varepsilon_\gamma^0 \cdot q' &= -\frac{1}{2Q} (m_V^2 + Q^2) \\ \varepsilon_M^0 \cdot k_1 &= -\frac{1}{4\xi m_V} (x + \xi) (m_V^2 + Q^2) & \varepsilon_M^0 \cdot k_2 &= -\frac{1}{4\xi m_V} (x - \xi) (m_V^2 + Q^2) \\ \varepsilon_M^0 \cdot q &= \frac{1}{2m_V} (m_V^2 + Q^2) & q \cdot q' &= \frac{1}{2} (m_V^2 - Q^2) \\ q \cdot k_1 &= \frac{1}{4\xi} (x + \xi) (m_V^2 + Q^2) & q \cdot k_2 &= \frac{1}{4\xi} (x - \xi) (m_V^2 + Q^2) \\ q' \cdot k_1 &= q \cdot k_1 & q' \cdot k_2 &= q \cdot k_2 \end{aligned} \quad (3.15)$$

We now have everything we need to fully calculate the traces and put them in a useful

form. In order to do so, we have to specify what the helicities of the photon, meson, and gluons. For photoproduction, the only option is to have a transversely polarized photon, and in this case, the meson must also be transversely polarized due to conservation of angular momentum. For this case, diagrams A and B do not contribute, their traces are always zero. Of the remaining four diagrams, only two ever contribute, and which two depends on the relationship among the particle polarizations. If all the polarizations are the same, then diagrams C and D contribute, with the trace being given by

$$-16m_q \frac{x - \xi}{4\xi} (m_V^2 + Q^2) \quad (3.16)$$

If, however, the photon and meson have the same polarization, which differs from that of the gluons, diagrams E and F contribute instead, yielding a trace of

$$16m_q \frac{x + \xi}{4\xi} (m_V^2 + Q^2) \quad (3.17)$$

All other combinations of transverse polarizations yield a trace which is zero. Note that these are only the traces, if we include the denominators determined earlier, we obtain the same result from either case.

If we look now at electroproduction, the photon and meson are allowed to have a longitudinal polarization, though the initial and final gluons must still have the same helicity. In this situation, every diagram contributes, with the traces being given by

$$\begin{aligned} \text{for diagrams A,B: } & \frac{(x - \xi)(x + \xi)}{2Q\xi^2} (Q^2 + m_V^2)^2 \\ \text{for diagrams C,D: } & \frac{x - \xi}{2Q\xi} (Q^2 - m_V^2) (Q^2 + m_V^2) \\ \text{for diagrams E,F: } & -\frac{x + \xi}{2Q\xi} (Q^2 - m_V^2) (Q^2 + m_V^2) \end{aligned} \quad (3.18)$$

Now that we have the traces and propagator denominators sorted out, all we have left are the other remaining prefactors. From the relevant Feynman rules, we have factors of:

- $ie_q e$, from the photon vertex

- i from each quark propagator (of which there are 2)
- $ig(T_a)_{kj}$ from the initial gluon vertex (a denotes the color index of the gluon, while k and j refer to the quark lines)
- $ig(T_b)_{ji}$ from the final gluon vertex
- $\frac{\delta_{ki}}{4N_C} f_V$ from the meson wavefunction
- $\frac{\delta_{ab}}{8}$ from the nucleon matrix element

In the above, we have introduced the meson decay constant, f_V , which can be determined from the leptonic decay width through

$$\Gamma_{l+l-} = \frac{2\pi e_q^2 \alpha^2 f_V^2}{3m_q} \quad (3.19)$$

If we combine the above terms, we obtain

$$(i)^5 e_q e g^2 (T_a)_{kj} (T_b)_{ji} \frac{\delta_{ki} f_V}{4N_C} \frac{\delta_{ab}}{8} = \frac{\pi i e_q e \alpha_s f_V}{8N_C} (T_a)_{ij} (T_a)_{ji} \quad (3.20)$$

Where we have substituted $g^2 = 4\pi\alpha_s$; finishing up, we have

$$\frac{\pi i e_q e \alpha_s f_V}{8N_C} \text{Tr}[T_a T_a] = \frac{\pi i e_q e \alpha_s f_V}{2N_C} \quad (3.21)$$

With this result, we are now ready to combine everything and write our final result for the subprocess amplitudes.

We use the notation $\mathcal{H}_{\mu'\lambda',\mu\lambda}$, where μ and μ' are the photon and meson polarizations, respectively; with λ and λ' being the initial and final gluon polarizations, respectively. Also, we have to remember that the results we gave above are for individual diagrams, while each result is for two diagrams, so we must multiply by a factor of 2. After some trivial algebra, we find that both transverse cases (all polarizations being the same, and

gluons differing from the photon/meson) give us the same result:

$$\mathcal{H}_{\mu'\lambda',\mu\lambda} = \frac{16\pi e_q e \alpha_s f_V}{N_C} \frac{m_V}{m_V^2 + Q^2} \delta_{\mu,\mu'} \delta_{\lambda,\lambda'} \quad (3.22)$$

The longitudinal result is similar,

$$\mathcal{H}_{0\lambda',0\lambda} = -\frac{16\pi e_q e \alpha_s f_V}{N_C} \frac{Q}{m_V^2 + Q^2} \delta_{\lambda,\lambda'} \quad (3.23)$$

It may seem odd at first glance that we are limited in the helicity choices we have, since *a priori* there is no reason for such a limitation. This constraint, however, can be traced back to the polarization vectors. When performing the trace calculations, we obtain the products of many combinations of these vectors. As seen above, only a few of the combinations are nonzero, which is a result of the form the vectors take, due to our use of the collinear approximation. This greatly simplifies the helicity structure of the subprocess, and restricts the GPDs which we are sensitive to, as will be made clear shortly.

Now that we have a result for the subprocess amplitude, we need to determine how it relates to the full process, which is what we will need to calculate any observables, such as the cross section. The full helicity amplitudes are given by (see, for example, [56])

$$\mathcal{M}_{\mu'\nu',\mu\nu} = \int_{-1}^1 \frac{dx}{(x + \xi - i\epsilon)(x - \xi + i\epsilon)} \sum_{\lambda,\lambda'} \mathcal{H}_{\mu'\lambda',\mu\lambda} \mathcal{A}_{\nu'\lambda',\nu\lambda}, \quad (3.24)$$

where $\mathcal{A}_{\nu'\lambda',\nu\lambda}$ are matrix elements which describe the nucleon-gluon interaction. They are defined as [58],

$$\mathcal{A}_{\nu'\lambda',\nu\lambda} = \int \frac{dz^-}{2\pi} e^{ixP^+z^-} \langle p', \nu' | \mathcal{O}_{\lambda',\lambda}(z) | p, \nu \rangle \Big|_{z^+=0, \mathbf{z}_T=0}, \quad (3.25)$$

where the operator, \mathcal{O} , depends on the helicities of the gluons. Parity invariance leads to the relation

$$\mathcal{A}_{-\nu'-\lambda',-\nu-\lambda} = (-1)^{\nu'-\lambda'-\nu+\lambda} \mathcal{A}_{\nu'\lambda',\nu\lambda}, \quad (3.26)$$

which halves the number of independent matrix elements, and means that the only relevant operator for our purposes is

$$\mathcal{O}_{+,+} = \frac{1}{2} \left[G^{+\alpha} G_{\alpha}^{+} - i G^{+\alpha} \tilde{G}_{\alpha}^{+} \right] \quad (3.27)$$

These matrix elements are calculated in a similar way to the simplification of the GPD expressions detailed in Section B, and yield

$$\begin{aligned} A_{+,+,++} &= \frac{\sqrt{1-\xi^2}}{2} \left(H^g(x, \xi, t) - \frac{\xi^2}{1-\xi^2} E^g(x, \xi, t) \right) \\ A_{+,+,-+} &= \frac{\sqrt{t'}}{4m} E^g \end{aligned} \quad (3.28)$$

for the nucleon helicity non-flip and flip elements, respectively.

Due to the restriction on the gluon helicities in the subprocess, the summation over λ' is trivial,

$$\mathcal{M}_{\mu'\nu',\mu\nu} = 2 \int_0^1 \frac{dx}{(x+\xi)(x-\xi+i\epsilon)} \sum_{\lambda} \mathcal{H}_{\mu'\lambda,\mu\lambda} \mathcal{A}_{\nu'\lambda,\nu\lambda}, \quad (3.29)$$

where we have restricted the integration range to simplify the calculations. This results in the $x + \xi$ term in the denominator no longer becoming singular within the integration range, which allows us to drop the $i\epsilon$ from that term. Since the gluon distributions are symmetric in x , we have introduced a factor of 2 to compensate for the halved integration range. Combining Eqs. (3.22) (or (3.23)) and (3.28) with Eq. (3.29), we arrive at

$$\begin{aligned} \mathcal{M}_{\pm+, \pm+} &= \mathcal{M}_{\pm-, \pm-} = \frac{8\pi e_q e \alpha_s f_V}{N_C} \frac{m_V}{m_V^2 + Q^2} \sqrt{1-\xi^2} \int_0^1 \frac{dx}{(x+\xi)(x-\xi+i\epsilon)} H_{\text{eff}}^g(x, \xi, t) \\ \mathcal{M}_{\pm-, \pm+} &= -\mathcal{M}_{\pm+, \pm-} = \frac{8\pi e_q e \alpha_s f_V}{N_C} \frac{m_V}{m_V^2 + Q^2} \frac{\sqrt{t'}}{2m} \int_0^1 \frac{dx}{(x+\xi)(x-\xi+i\epsilon)} E^g(x, \xi, t) \end{aligned}$$

where $H_{\text{eff}}^g(x, \xi, t) = H^g(x, \xi, t) - \frac{\xi^2}{1-\xi^2} E^g(x, \xi, t)$

Comparing Eqs. (3.22) and (3.23), we see that they can be simply related, leading to a simple relation between their full amplitudes as well,

$$\begin{aligned}\mathcal{M}_{0+,0+} &= \mathcal{M}_{0-,0-} = -\frac{Q}{m_V} \mathcal{M}_{\pm\pm,\pm\pm} \\ \mathcal{M}_{0-,0+} &= -\mathcal{M}_{0+,0-} = -\frac{Q}{m_V} \mathcal{M}_{\pm\pm,\pm\pm}\end{aligned}\tag{3.31}$$

This relation between the longitudinal and transverse amplitudes agrees with that found in the pioneering work on exclusive J/ψ production, [29].

The simple relations we have among the production amplitudes makes the computations easier, however, they also mean that we are sensitive only to the GPDs H and E . While it was once thought that the polarized gluon distributions might be accessible, [59], it turns out that this was simply due to a calculation error, [60]. Our results are also consistent with those of [60], where it was found that the other helicity amplitudes for the subprocess are greatly suppressed. The collinear approximation leads to not merely a suppression of these terms, but to them being zero.

3.3.2 Next to Leading Order

Next-to-Leading Order amplitudes are present in the literature for photoproduction [32]; as stated earlier, once we start looking at NLO corrections, not only do we have a gluon contribution, but also a quark one. Additionally, the gluon calculation becomes quite a bit more complicated, with the addition of 58 more diagrams necessary for the full NLO process. As an example, Fig. 3.3 shows two subprocess diagrams featuring the emission of a soft gluon from the antiquark line. Likewise, Fig. 3.4 shows the quark contribution to heavy vector meson production. For a full discussion of the details of the calculation of the NLO corrections, including a full breakdown of the needed diagrams, see [32].

The NLO corrections are applied directly to the production amplitudes, which can be

$m_q f_V^2$, leaving us with

$$\mathcal{M} = \frac{4\pi e e_q f_V (e_V^* e_\gamma)}{N_c \xi m_q} \int_{-1}^1 dx [T_g(x, \xi) F^g(x, \xi, t) + T_q(x, \xi) F^{q,S}(x, \xi, t)]. \quad (3.33)$$

T_g and T_q contain information regarding the LO and NLO contributions, given by

$$T_q(x, \xi) = \frac{\alpha_S^2(\mu_R) C_F}{2\pi} f_q \left(\frac{x - \xi + i\varepsilon}{2\xi} \right), \quad (3.34)$$

for the quarks and

$$T_g(x, \xi) = \frac{\xi}{(x - \xi + i\varepsilon)(x + \xi - i\varepsilon)} \left[\alpha_S(\mu_R) + \frac{\alpha_S^2(\mu_R)}{4\pi} f_g \left(\frac{x - \xi + i\varepsilon}{2\xi} \right) \right], \quad (3.35)$$

for the gluons. From these it can be seen that there is both a LO and a NLO contribution from gluons, but only a NLO contribution from the quark exchange. Additionally, the LO expression matches the expression found earlier, Eq. (3.30). f_g and f_q are the main results of [32]; f_q is given by

$$\begin{aligned} f_q(y) = & \left(\ln \frac{4m^2}{\mu_F^2} - 1 \right) (1 + 2y) \left(\frac{\ln(-y)}{1+y} - \frac{\ln(1+y)}{y} \right) - \pi^2 \frac{13(1+2y)}{48y(1+y)} + \frac{2 \ln 2}{1+2y} \\ & + \frac{\ln(-y) + \ln(1+y)}{1+2y} + (1+2y) \left(\frac{\ln^2(-y)}{1+y} - \frac{\ln^2(1+y)}{y} \right) \\ & + \frac{3 - 4y + 16y(1+y)}{4y(1+y)} \text{Li}_2(1+2y) - \frac{7 + 4y + 16y(1+y)}{4y(1+y)} \text{Li}_2(-1-2y), \end{aligned} \quad (3.36)$$

where $y = \frac{x - \xi + i\varepsilon}{2\xi}$. The expression for f_g is (using the same definition for y)

$$\begin{aligned} f_g(y) = & 4(c_1 - c_2)(1 + 2y(1 + y)) \left(\frac{\ln(-y)}{1+y} - \frac{\ln(1+y)}{y} \right) \left(\ln \frac{4m^2}{\mu_F^2} - 1 \right) + \beta_0 \ln \frac{\mu_R^2}{\mu_F^2} \\ & + 4(c_1 - c_2)(1 + 2y(1 + y)) \left(\frac{\ln^2(-y)}{1+y} - \frac{\ln^2(1+y)}{y} \right) - 8c_1 \\ & - \pi^2 \left(\frac{2 + y(1 + y)(25 + 88y(1 + y))}{48y^2(1 + y)^2} c_1 + \frac{10 + y(1 + y)(7 - 52y(1 + y))}{24y^2(1 + y)^2} c_2 \right) \\ & - \left[c_1 \frac{1 + 6y(1 + y)(1 + 2y(1 + y))}{y(1 + y)(1 + 2y)^2} + c_2 \frac{(1 + 2y)^2}{y(1 + y)} \right] \ln(2) \end{aligned}$$

$$\begin{aligned}
& + \pi \frac{\sqrt{-y(1+y)}}{y(1+y)} \left(\frac{7}{2}c_1 - 3c_2 \right) \\
& + 2c_2 \frac{\sqrt{-y(1+y)}}{y(1+y)} \left(\frac{1+4y}{1+y} \arctan \sqrt{\frac{-y}{1+y}} + \frac{3+4y}{y} \arctan \sqrt{\frac{1+y}{-y}} \right) \\
& - \frac{\arctan^2 \sqrt{\frac{-y}{1+y}}}{2y(1+y)} \left((7+4y)c_1 - 2 \frac{1+2y-2y^2}{1+y} c_2 \right) \\
& - \frac{\arctan^2 \sqrt{\frac{1+y}{-y}}}{2y(1+y)} \left((3-4y)c_1 - 2 \frac{3+6y+2y^2}{y} c_2 \right) \\
& + 2a_1(y) \ln(-y) + 2a_1(-1-y) \ln(1+y) \\
& + 2a_2(y) \text{Li}_2(1+2y) + 2a_2(-1-y) \text{Li}_2(-1-2y). \quad (3.37)
\end{aligned}$$

The dilogarithm, $\text{Li}_2(z)$, appears in the final two terms. This function is defined as

$$\text{Li}_2(z) = - \int_0^z \frac{\ln(1-t)}{t} dt \quad (3.38)$$

and is real-valued in the region $0 < z \leq 1$, and complex-valued for $z > 1$. Finally, the expressions a_1 and a_2 are given by

$$\begin{aligned}
a_1(y) = \frac{c_1}{4} \left(5 + 16y - \frac{6}{1+y} + \frac{1}{(1+2y)^2} - \frac{5}{1+2y} \right) \\
- \frac{c_2}{2} \left(2 + \frac{3}{y} + 8y - \frac{1}{1+y} \right), \quad (3.39)
\end{aligned}$$

and

$$\begin{aligned}
a_2(y) = \frac{c_1}{8} \left(12 + \frac{9}{y} + 64y - \frac{2}{(1+y)^2} + \frac{21}{1+y} - \frac{4}{1+2y} \right) \\
- \frac{c_2}{4} \left(8 + \frac{3}{y^2} + \frac{11}{y} + 32y - \frac{2}{(1+y)^2} + \frac{9}{1+y} \right). \quad (3.40)
\end{aligned}$$

3.3.3 Light Mesons

So far, everything has been done for the case of mesons consisting of heavy quarks, e.g. J/Ψ or Υ . It is also possible to investigate exclusive production of light vector mesons, e.g.

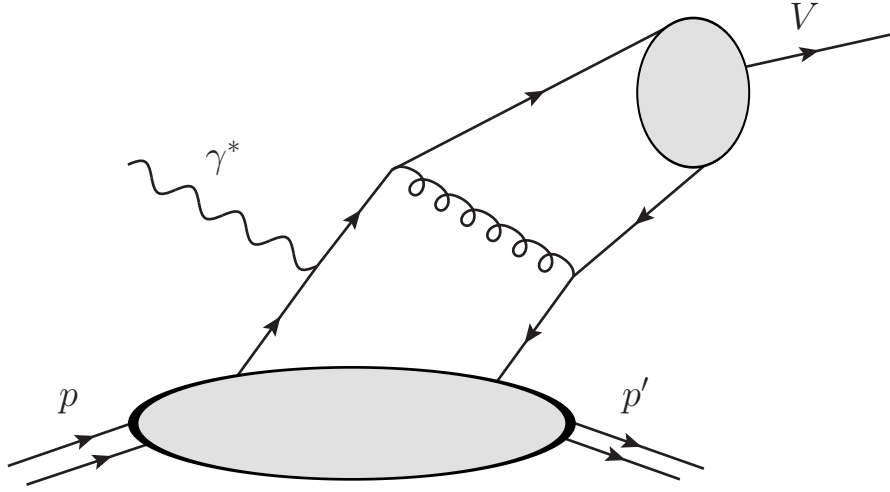


Figure 3.5: The LO quark exchange diagram for production of light vector mesons

ϕ or ρ . In this case, we can no longer use the mass of the meson as a large scale in the process, and must therefore resort to electroproduction. We require that the virtuality of the photon, Q^2 , be much larger than the meson's mass for this situation. We can directly use Eq. (3.31) if we simply set the meson mass to zero. Photoproduction of light mesons does not give access to the GPDs, which can also be seen in the fact that the transverse expressions are zero. The longitudinal amplitudes are consistent with previous determinations of light vector meson production, see, e.g. [31, 58, 61].

Additionally, we recall that at LO we did not have a quark contribution to heavy meson production since the inherent charm or bottom in the nucleon is small. This is not the case for light meson production, as even the inherent strangeness of the nucleon is non-negligible. We can therefore not ignore this contribution to the production amplitudes, given by the diagram in Fig. 3.5. - Following the same procedure as above to obtain the production amplitudes yields for ρ production

$$\mathcal{M}_{0+,0+}^q = \frac{16\pi e\alpha_s f_V}{3Q} \sum_{qq'} \int_{-1}^1 dx H_{\text{eff}}^{q'q}(x, \xi, t) \left[\frac{e_q}{(x - \xi + i\epsilon)} - \frac{e_{q'}}{(x + \xi - i\epsilon)} \right] \quad (3.41)$$

for the nonflip amplitude and

$$\mathcal{M}_{0-,0+}^q = \frac{-16\pi e\alpha_s f_V \sqrt{-t'}}{3Q} \frac{1}{2m} \sum_{qq'=-1}^1 \int dx E^{q'q}(x, \xi, t) \left[\frac{e_q}{(x - \xi + i\epsilon)} - \frac{e_{q'}}{(x + \xi - i\epsilon)} \right] \quad (3.42)$$

for the flip amplitude.

CHAPTER 4

OBSERVABLES: ANALYTICAL RESULTS

Now that the GPDs have been introduced, the kinematics specified, and the production amplitudes determined, we can move on to their applications. Since experiments cannot directly measure the production amplitudes, we have to instead determine what observables are available, and focus on those which give us access to the gluon GPD E .

4.1 Cross Sections

The most basic observable is the unpolarized cross section. The cross section can be considered as a way of describing how likely a process is to occur; a differential cross section describes this likelihood for a certain kinematical value, while the full integrated cross section describes the overall likelihood. The cross section has units of area, while the units for the differential cross section depends on what the differential variable is.

Depending on the experiment, one may be able to access the differential cross section, or only the integrated. For example, experimentally we have only integrated cross section results for Υ since the count rates are so low, while for J/ψ we also have differential cross section results.

For electroproduction, the full differential cross section in t is given by the combination

$$\frac{d\sigma}{dt} = \frac{d\sigma_T}{dt} + \varepsilon \frac{d\sigma_L}{dt}, \quad (4.1)$$

where ε is the ratio of the longitudinal to transverse photon fluxes, and the two terms de-

note the differential cross sections due to transversely or longitudinally polarized photons, respectively. We calculate each of these through

$$\frac{d\sigma}{dt} = \frac{1}{16\pi(W^2 - m^2)\sqrt{\Lambda(W^2, -Q^2, m^2)}} \sum_{\mu', \nu', \mu, \nu} |\mathcal{M}_{\mu'\nu', \mu\nu}|^2, \quad (4.2)$$

where $\Lambda(x, y, z) = x^2 + y^2 + z^2 - 2xy - 2xz - 2yz$. In our particular case, using the results for the production amplitudes (3.30), the two terms yield

$$\begin{aligned} \frac{d\sigma_T}{dt} &= \frac{1}{16\pi(W^2 - m^2)\sqrt{\Lambda(W^2, -Q^2, m^2)}} (|\mathcal{M}_{\pm\pm, \pm\pm}|^2 + |\mathcal{M}_{\pm-, \pm\pm}|^2) \\ \frac{d\sigma_L}{dt} &= \frac{1}{16\pi(W^2 - m^2)\sqrt{\Lambda(W^2, -Q^2, m^2)}} (|\mathcal{M}_{0+, 0+}|^2 + |\mathcal{M}_{0-, 0+}|^2), \end{aligned} \quad (4.3)$$

These differential cross section can be integrated over t to obtain the integrated cross sections, for which an analogous expression to (4.1) exists.

4.2 Spin Density Matrix Elements

Spin Density Matrix Elements (SDMEs) describe the angular distribution of the process. Interest in them began with the seminal work by Schilling and Wolf [62]. This work described the elements for an unpolarized, as well as both a transversely and longitudinally polarized lepton beam incident on an unpolarized target. Work by Diehl [63] extended this framework to the case of a polarized target. Diehl additionally introduced a different notation to express the SDMEs, which has the benefit of making certain symmetries more readily apparent. Most of the calculations we perform here are in Diehl's notation, since it is more general. The experimental results use the older Schilling and Wolf notation, however, so we also include relations between the two.

The SDMEs are expressed in terms of the production amplitudes, Eqs. (3.30) and (3.31). Due to the symmetries in the production amplitudes for this work, the SDMEs yield only

a small number of useful observables. The SDMEs are defined by

$$\rho_{\mu\bar{\mu},\nu\bar{\nu}}^{\mu'\bar{\mu}'} = \frac{1}{N_T + \epsilon N_L} \sum_{\nu'} \mathcal{M}_{\mu'\nu',\mu\nu} \mathcal{M}_{\bar{\mu}'\nu',\bar{\mu}\bar{\nu}}^* \quad (4.4)$$

The upper indices denote the spin density matrix of the vector meson, while the lower indices specify the γ^*p polarization state. The normalization factors, which are proportional to the differential cross sections for transverse and longitudinal photon polarization, are given by

$$N_T = \frac{1}{2} \sum_{\mu',\nu',\nu} |\mathcal{M}_{\mu'\nu',+\nu}|^2 \quad N_L = \frac{1}{2} \sum_{\mu',\nu',\nu} |\mathcal{M}_{\mu'\nu',0\nu}|^2. \quad (4.5)$$

More useful than the elements themselves, however, are combinations of them. For an unpolarized and longitudinally polarized target, respectively, we have

$$u_{\mu\bar{\mu}}^{\mu'\bar{\mu}'} = \frac{1}{2} \left(\rho_{\mu\bar{\mu},++}^{\mu'\bar{\mu}'} + \rho_{\mu\bar{\mu},--}^{\mu'\bar{\mu}'} \right) \quad l_{\mu\bar{\mu}}^{\mu'\bar{\mu}'} = \frac{1}{2} \left(\rho_{\mu\bar{\mu},++}^{\mu'\bar{\mu}'} - \rho_{\mu\bar{\mu},--}^{\mu'\bar{\mu}'} \right), \quad (4.6)$$

while for a target polarization transverse in the hadron plane ("sideways") and perpendicular to it ("normal") we have, respectively

$$s_{\mu\bar{\mu}}^{\mu'\bar{\mu}'} = \frac{1}{2} \left(\rho_{\mu\bar{\mu},+-}^{\mu'\bar{\mu}'} + \rho_{\mu\bar{\mu},-+}^{\mu'\bar{\mu}'} \right) \quad n_{\mu\bar{\mu}}^{\mu'\bar{\mu}'} = \frac{1}{2} \left(\rho_{\mu\bar{\mu},+-}^{\mu'\bar{\mu}'} - \rho_{\mu\bar{\mu},-+}^{\mu'\bar{\mu}'} \right).$$

There is one model-independent normalization constraint [63],

$$u_{++}^{++} + u_{++}^{--} + 2\epsilon u_{00}^{++} = 1 - \left(u_{++}^{00} + \epsilon u_{00}^{00} \right). \quad (4.7)$$

As an example of how to obtain a useful expression for the SDME combinations, consider

$$u_{++}^{++} = \frac{1}{2} \left(\rho_{++}^{++} + \rho_{++}^{--} \right). \quad (4.8)$$

The SDMEs can be expressed through the production amplitudes by

$$\begin{aligned}\rho_{++}^{++} &= \frac{1}{N_T + \epsilon N_L} [\mathcal{M}_{++} \mathcal{M}_{++}^* + \mathcal{M}_{+-} \mathcal{M}_{+-}^*] \\ \rho_{++}^{+-} &= \frac{1}{N_T + \epsilon N_L} [\mathcal{M}_{++} \mathcal{M}_{+-}^* + \mathcal{M}_{+-} \mathcal{M}_{++}^*].\end{aligned}\quad (4.9)$$

Until this point, we have kept the discussion completely general, now we can use the relations between the transverse production amplitudes (3.30) to write

$$u_{++}^{++} = \frac{1}{N_T + \epsilon N_L} [\mathcal{M}_{++} \mathcal{M}_{++}^* + \mathcal{M}_{+-} \mathcal{M}_{+-}^*]. \quad (4.10)$$

Due to the structure of the normalization, both the numerator and denominator can be expressed in terms of the transverse production amplitudes, and both appear in the combination $|\mathcal{M}_{++}|^2 + |\mathcal{M}_{+-}|^2$. Note that this is not a general feature, but is unique to our approach. This allows an easy simplification by using the relations among them, yielding

$$u_{++}^{++} = \frac{m_V^2}{m_V^2 + \epsilon Q^2}. \quad (4.11)$$

This expression reveals an amazing result of our approach — u_{++}^{++} has no dependence on the GPDs, only the meson mass and the photon virtuality. In fact, for photoproduction, we find that the result should be constant, and is in complete agreement with the normalization condition (4.7).

Another result of the simple amplitude relations is that there are only 8 nonzero combinations,

$$\begin{aligned}u_{++}^{++}, u_{+-}^{+-}, u_{00}^{00}, u_{0+}^{0+} \\ n_{++}^{++}, n_{+-}^{+-}, n_{00}^{00}, n_{0+}^{0+}.\end{aligned}\quad (4.12)$$

This result implies that the only nonzero effects are for transverse target polarization perpendicular to the hadron plane. Additionally, of the nonzero combinations, only two are independent, u_{++}^{++} and n_{++}^{++} ; the other 6 can be written in terms of these. Following the

same procedure outlined above, we obtain

$$\begin{aligned}
 u_{-+}^{-+} &= u_{++}^{++} \\
 u_{0+}^{0+} &= \frac{Q}{m_V} u_{++}^{++} \\
 u_{00}^{00} &= \frac{Q^2}{m_V^2} u_{++}^{++},
 \end{aligned} \tag{4.13}$$

and

$$\begin{aligned}
 n_{++}^{++} &= -2i \frac{\text{Im}(\mathcal{M}_{++,++} \mathcal{M}_{+-,++}^*)}{\left(1 + \epsilon \frac{Q^2}{m_V^2}\right) (|\mathcal{M}_{++,++}|^2 + |\mathcal{M}_{+-,++}|^2)} \\
 n_{-+}^{-+} &= n_{++}^{++} \\
 n_{0+}^{0+} &= \frac{Q}{m_V} n_{++}^{++} \\
 n_{00}^{00} &= \frac{Q^2}{m_V^2} n_{++}^{++}.
 \end{aligned} \tag{4.14}$$

Note that based on the results for the nonzero combinations, the constraint (4.7) reduces to

$$u_{++}^{++} + \epsilon u_{00}^{00} = 1, \tag{4.15}$$

which can easily be shown to be satisfied.

As previously mentioned, the current experimental data uses the older Schilling and Wolf notation. The J/ψ data currently contains results for

$$r_{00}^{04}, r_{1-1}^{04}, r_{1-1}^1, r_{00}^1 + 2r_{11}^1, \text{ and } r_{00}^5 + 2r_{11}^5. \tag{4.16}$$

Of these quantities, only 2 are nonzero in our approach, and can be written in terms of Diehl's notation through

$$\begin{aligned}
 r_{00}^{04} &= u_{++}^{00} + \epsilon u_{00}^{00} = \epsilon u_{00}^{00} \\
 r_{1-1}^1 &= \frac{1}{2} (u_{-+}^{-+} + u_{-+}^{+-}) = \frac{1}{2} u_{-+}^{-+}.
 \end{aligned}$$

After some simple algebra, we have

$$\begin{aligned} r_{00}^{04} &= \frac{\epsilon Q^2}{m_V^2 + \epsilon Q^2} \\ r_{1-1}^1 &= \frac{1}{2} \frac{m_V^2}{m_V^2 + \epsilon Q^2}. \end{aligned} \quad (4.17)$$

Our results also satisfy the expression

$$r_{1-1}^1 = \frac{1}{2} (1 - r_{00}^{04}), \quad (4.18)$$

which is valid for s -channel helicity conservation and natural parity exchange. Additionally, while there is currently no experimental data for it, we have

$$\text{Im } r_{10}^6 = -\text{Re } r_{10}^5 = \frac{1}{2\sqrt{2}} \frac{m_V Q}{m_V^2 + \epsilon Q^2} \quad (4.19)$$

While comparison of these SDMEs to data is unable to yield much information on the GPDs themselves, it can help to verify our approach. The simple relations we find among the SDMEs are straightforward checks of our method and, in particular, of the relations we obtain among the production amplitudes. We still would like to have an experimental way of constraining E^g , however, and as we can see, the SDMEs do not provide much information on this matter.

4.3 Asymmetries

The first observable which we can investigate to obtain more information about the GPD E^g is the single spin asymmetry A_N . This asymmetry is also sometimes written as A_{UT} , since it denotes an unpolarized beam and a transversely polarized target. This asymmetry is actually closely related to the SDMEs for a target polarized perpendicular to the hadron

plane, and can be written in terms of them. We start with the definition

$$A_N = \frac{1}{N_T + \varepsilon N_L} \frac{1}{2} \sum_{\mu', \nu'} [(|\mathcal{M}_{\mu'\nu',++}|^2 - |\mathcal{M}_{\mu'\nu',+-}|^2) + \varepsilon (|\mathcal{M}_{\mu'\nu',0+}|^2 - |\mathcal{M}_{\mu'\nu',0-}|^2)], \quad (4.20)$$

then simplify based on Eqs. (3.30) and (3.31), yielding

$$A_N = -2 \frac{\text{Im}(\mathcal{M}_{++,++} \mathcal{M}_{+-,++}^*) + \varepsilon \text{Im}(\mathcal{M}_{0+,0+} \mathcal{M}_{0-,0+}^*)}{|\mathcal{M}_{++,++}|^2 + |\mathcal{M}_{+-,++}|^2 + \varepsilon (|\mathcal{M}_{0+,0+}|^2 + |\mathcal{M}_{0-,0+}|^2)}. \quad (4.21)$$

Using (3.31), this can easily be reduced to

$$A_N = -2 \frac{\text{Im}(\mathcal{M}_{++,++} \mathcal{M}_{+-,++}^*)}{|\mathcal{M}_{++,++}|^2 + |\mathcal{M}_{+-,++}|^2}. \quad (4.22)$$

We immediately notice the similarity to our expression for n_{++}^{++} , and in fact, A_N can be given in terms of these SDMEs,

$$A_N = \text{Im}(n_{++}^{++} + \varepsilon n_{00}^{00}). \quad (4.23)$$

Since this asymmetry is proportional to the product of the flip and nonflip amplitudes, it is sensitive to the interference between H^g and E^g . In this way, we can gain some knowledge of E^g even if it is smaller than H^g .

With A_N being proportional to the imaginary part of the product of the flip and nonflip amplitudes, it is perhaps reasonable to wonder whether the real part of this product is able to be accessed, and whether it would even be useful to do so. There would be a definite advantage to measuring the real part of the product, since there are some indications that in the gluon sector the phase between E^g and H^g are similar, leading to a small value for the imaginary part, and therefore also A_N , even if E^g is not small compared to H^g . The real part of the product between the flip and nonflip amplitudes is harder to access experimentally, since it requires the measurement of the polarization of the recoil nucleon. The relevant double spin asymmetry can be defined if we consider objects similar to the

combinations seen above in the discussion of A_N ,

$$a_{i,f} = \frac{1}{N_T + \varepsilon N_L} \sum_{\mu'} [|\mathcal{M}_{\mu'f,+i}|^2 + \varepsilon |\mathcal{M}_{\mu'f,0i}|^2], \quad (4.24)$$

where the indices f and i indicate the final and initial polarization state of the nucleon. The same procedure as above can be followed to determine the different possibilities for $a_{i,f}$, which includes polarizations along the positive and negative axes of any of the three directions x, y , or z . For our situation, we are interested in the case of one nucleon polarized along the z direction, with the other along the x direction,

$$A_{LS} = a_{+,+x} - a_{-,+x} = 2 \frac{\text{Re}(\mathcal{M}_{++,++} \mathcal{M}_{+-,++}^*) + \varepsilon \text{Re}(\mathcal{M}_{0+,0+} \mathcal{M}_{0-,0+}^*)}{|\mathcal{M}_{++,++}|^2 + |\mathcal{M}_{+-,++}|^2 + \varepsilon (|\mathcal{M}_{0+,0+}|^2 + |\mathcal{M}_{0-,0+}|^2)}. \quad (4.25)$$

Again, we can simplify this expression using the relation between the longitudinal and transverse amplitudes (3.31),

$$A_{LS} = 2 \frac{\text{Re}(\mathcal{M}_{++,++} \mathcal{M}_{+-,++}^*)}{|\mathcal{M}_{++,++}|^2 + |\mathcal{M}_{+-,++}|^2}. \quad (4.26)$$

As mentioned above, this asymmetry could provide useful information regarding the nucleon spin-flip amplitude, and hence E^g , especially if E^g and H^g are similar in phase, leading to a small value for A_N . The square of the flip amplitude can also be accessed if both the initial and final nucleons are polarized in the z or the x direction; the reduced form reads

$$\frac{1}{2}(a_{+,-} + a_{-,+}) = \frac{1}{2}(a_{+x,-x} + a_{-x,+x}) = \frac{|\mathcal{M}_{+-,++}|^2}{|\mathcal{M}_{++,++}|^2 + |\mathcal{M}_{+-,++}|^2}. \quad (4.27)$$

While no additional interesting information can be obtained if either nucleon is polarized in the y direction, taking the unpolarized cross section, proportional to $|\mathcal{M}_{++,++}|^2 + |\mathcal{M}_{+-,++}|^2$, A_N , A_{LS} , and the observable in (4.27) gives us complete information on the real and imaginary parts of both the non-flip and spin-flip amplitudes.

4.4 Next to Leading Order

Very few changes need to be made to the expressions for any of our observables in order to include the NLO corrections. This is due to the fact that they are directly taken into account in the production amplitudes; additionally, none of the simple relations among our amplitudes are affected. We do note that the NLO results are valid only for photoproduction, so when dealing with results at NLO, no longitudinal amplitudes are considered. The only other point that requires consideration is what order in α_S we keep terms proportional to. If we look at Eqs. (3.32)-(3.35) and (4.2), we note that while the production amplitudes go up to $\mathcal{O}(\alpha_S^2)$, in order to calculate the cross section, we square the amplitude, therefore giving us terms proportional to $\mathcal{O}(\alpha_S^4)$. We borrow Diehl and Kugler's reasoning [55], and retain terms of this order. The argument is that if the corrections are not too large, then the missing terms which would come from the next-to-next-to-leading order expressions would make little difference, and if the corrections are large, then the NLO results are probably not well under control anyway.

4.5 Light Mesons

As mentioned in Section 3.3.3, when we perform our calculations for the production of light vector mesons, we neglect the meson mass. This means that we need to have another large scale in the process, which we take to be the virtuality of the photon, Q^2 , meaning that photoproduction is not allowed. Additionally, we no longer have transverse amplitudes, so the asymmetries depend now only on the longitudinal amplitudes. As for the SDMEs, we have only two combinations in Diehl's notation that are nonzero, u_{00}^{00} and n_{00}^{00} . In this case, u_{00}^{00} is trivially given by $1/\varepsilon$, while n_{00}^{00} is slightly more complicated,

$$n_{00}^{00} = -\frac{2i}{\varepsilon} \frac{\text{Im}(\mathcal{M}_{0+,0+} \mathcal{M}_{0-,0+}^*)}{|\mathcal{M}_{0+,0+}|^2 + |\mathcal{M}_{0-,0+}|^2}. \quad (4.28)$$

CHAPTER 5

OBSERVABLES: NUMERICAL RESULTS

Now that we have the analytic expressions for our observables, we can use them to obtain numerical predictions which can then be compared to experimental data. The code which we use to evolve the GPDs is fairly complex, and introduces some technical difficulties, so a description of these complexities and the ways in which they were overcome is discussed first, followed by a similar discussion for the NLO calculations, and finally a presentation of our numerical results, compared to experiment.

5.1 GPDs and Evolution

As input for the GPDs, we start with a modified version of the CTEQ6M parton distributions, developed through the work of Goloskokov and Kroll (see, for instance [37, 40–42, 53]). These are given at a starting scale of $\mu_0 = 2.0$ GeV, and are used as an input for the double distribution method as discussed in Chapter 2 and Appendix A.

As mentioned previously, we use code developed by Vinnikov [27] to perform the evolution of the GPDs. The benefit of this code is that it achieves reasonable accuracy with a very quick runtime. It is able to do this by exploiting various symmetries inherent in the GPDs themselves, e.g. the x symmetry of the gluon GPDs means that it needs to be calculated for only half the total x range. Another aspect of the code which leads to fast computation is that the points sampled are not evenly spaced in x . Rather, the x values

sampled conform to

$$\begin{aligned}
 x_i &= \delta e^{\gamma i} - \delta \\
 \gamma &= \frac{1}{n} \ln \left(\frac{1 - \xi}{\xi} \right) \\
 \delta &= \frac{\xi^2}{1 - 2\xi},
 \end{aligned} \tag{5.1}$$

where n is set at runtime, equal to the total number of data points in each evolution region, and i is a loop variable running from 0 through $2n$. Additionally, there is another parameter essential to the evolution routine, internally called m . This is similar to n in that it impacts a step size, however, in this case m governs the step size in the scale of the process. The code breaks the evolution up into a number of separate evolutions starting at the initial scale and ending with the evolved scale. As an example, if $m = 10$ and we want to evolve the GPDs from $\mu = 2$ GeV to $\mu = 4$ GeV, the evolution calculation will be performed 10 times. First the code will evolve the GPDs from $\mu = 2$ GeV to $\mu = 2.2$ GeV, then it will use the result from that and evolve it to $\mu = 2.4$ GeV, and so on, until it reaches the final scale.

An analysis was performed to determine the ideal values for n and m based on the relative difference between prospective values as compared to the runtime. The relative difference was calculated as the difference between two successive iterations divided by their average,

$$\text{Relative Difference} = 2 \frac{x_n - x_{n-1}}{x_n + x_{n-1}}. \tag{5.2}$$

Since with increasing n or m the results should converge towards the "true" value, if the relative difference shows little change between two successive iterations, then a sufficient parameter value has been achieved. The leading order and next-to-leading order amplitudes for both the initial and evolved scales were calculated for a series of n values, with m kept constant, and vice versa. All the amplitudes showed convergence as the number of steps increased. The greatest difference between successive iterations tended to be the evolved NLO amplitude. Even so, the relative difference was not large at any tested parameterization. Changing m had a much smaller effect than n , and a value of $m = 10$ was

chosen. Since the differences were so small when changing m , this choice is as much for the attractiveness of the number as it is for accuracy; increasing it any further will increase the computation time unnecessarily, while a decrease of the parameter will not garner substantial runtime benefits.

The case of changing n is slightly different. Vinnikov comments [27] that larger values of n will yield more precise results, and refers to a "careful" solution using $n = 500$. We quickly discovered that the runtime at large values of n can easily become unreasonable. A value of $n = 400$ was originally planned, since that would yield precise results, but have a shorter runtime than the $n = 500$ case. Prior to this analysis it was assumed that this value would be preferred over one closer to $n = 200$. What was found, however, is that when comparing $n = 260$ and $n = 400$ the relative difference is approximately halved, it also approximately doubles the runtime. Note that we did not compute the relative difference between $n = 400$ and $n = 260$. The relative difference was determined for $n = 400$ vs $n = 380$ and $n = 260$ vs $n = 240$. Since the percent relative difference for the evolved NLO amplitude between $n = 260$ and $n = 240$ is only about .02%, a value of $n = 260$ was deemed sufficient.

The parameterization for x leads to points spaced further apart the further one gets from the point $x = \xi$. Since the GPDs become smoother and flatter the further one goes from $x = \xi$, see Fig. 2.2, this parameterization works well. From looking at Eq. (5.1), one can see that the spacing in x is logarithmic, whereas the spacing in i is linear. While this allows greater precision close to the problem point $x = \xi$, it also introduces some difficulties with the calculations, especially the next to leading order ones.

The first obstacle to overcome is related to our numerical integration routine. The best case scenario would be to use an adaptive algorithm, allowing focus to be put on specific trouble areas, where the integrand is less smooth. However, this would require a major rewriting of the evolution code, since it generates the GPD data as a set of discrete points, as detailed above. For this reason, we resort to using Simpson's method of integration, specifically the composite Simpson's method. In this way, we can take advantage of the pre-calculated GPD data, allowing us to break up the total integration range into sets of

consecutive points. This works quite well since the GPDs are fairly smooth functions, with the area around $x = \xi$ being the most problematic.

The problem then, at first glance, with using Simpson's method is that it requires even spacing in the integration variable. The solution is to change the x integration to an integration over i . Using Eq. (5.1), we are able to determine the Jacobian for our variable change, giving us $dx_i = \gamma \delta e^{\gamma i} di$. For an arbitrary function $f(x)$, we then have

$$\int_A^B f(x) dx = \int_0^{2n} \gamma \delta e^{\gamma i} f(x_i) di. \quad (5.3)$$

The Jacobian, $\gamma \delta e^{\gamma i}$ can also be expanded to read

$$\frac{1}{n} \ln\left(\frac{1-\xi}{\xi}\right) \frac{\xi^2}{1-2\xi} \left(\frac{1-\xi}{\xi}\right)^{\frac{i}{n}}. \quad (5.4)$$

Including this term in the integral, as shown above means that we can utilize Simpson's Method to perform our integrations. Note that most of the Jacobian is independent of i , and can be computed once at the beginning of the calculation if one is concerned with optimizing the code as much as possible.

5.2 Next to Leading Order

Additional problems appear when moving to the NLO calculations, mostly due to the form these corrections take. It is important to note that evaluating the amplitude, Eq. (3.32), requires the product of the GPDs and f_g or f_q , Eqs. (3.37) and (3.36) respectively, to be integrated over x . This cannot be done numerically in a straightforward way, since just about every term becomes numerically unstable as x approaches ξ , which is contained in our integration region. Additionally, if one includes the factor of $1/(x - \xi)$ present in T_g , Eq. (3.35), there are terms which contain instabilities that go not only as $1/y$ (remembering that $y = (x - \xi)/(2\xi)$), but also $1/y^2$, and $1/y^3$. Besides these complications, there are also terms which contain both real and imaginary components which need to be integrated.

While the integrand is numerically unstable, and we loosely speak of divergences, the

integrals themselves are well defined due to the $i\epsilon$ prescription. In particular, the replacement $\xi \rightarrow \xi - i\epsilon$ yields the proper results (see, for example, the discussions following Eqs. 2.13 and 3.56 in ref. [32]). Beyond these instabilities, we also have terms which contain different branches, and the $i\epsilon$ prescription fixes also these functions by choosing the correct branch. Even with the $i\epsilon$, a numerical implementation is still problematic. A common method of dealing with integrals that have this behavior is to numerically perform a principle value integral, while also including terms which are proportional to the numerator, or a derivative of the numerator, i.e.

$$\int_a^b dx \frac{\varphi(x)}{x - \xi + i\epsilon} = -i\pi\varphi(\xi) + \mathcal{P} \int_a^b dx \frac{\varphi(x)}{x - \xi}. \quad (5.5)$$

This method is straightforward when the divergence is merely linear, but becomes more complex when the divergence increases, e.g.

$$\begin{aligned} \int_a^b dx \frac{\varphi(x)}{(x - \xi + i\epsilon)^2} &= -i\pi\varphi'(\xi) + \frac{b-a}{(a-\xi)(b-\xi)}\varphi(\xi) + \mathcal{P} \int_a^b dx \frac{\varphi(x) - \varphi(\xi)}{(x - \xi)^2} \\ \int_a^b dx \frac{\varphi(x)}{(x - \xi + i\epsilon)^3} &= -\frac{i\pi}{2}\varphi''(\xi) + \frac{(b-a)(a+b-2\xi)}{2(a-\xi)^2(b-\xi)^2}\varphi(\xi) + \frac{b-a}{(a-\xi)(b-\xi)}\varphi'(\xi) \\ &\quad + \mathcal{P} \int_a^b dx \frac{\varphi(x) - \varphi(\xi) - (x - \xi)\varphi'(\xi)}{(x - \xi)^3}. \end{aligned} \quad (5.6)$$

While more complex, these expressions are still able to be implemented without too much difficulty if ϕ is well behaved around the point $x = \xi$, i.e. if we can evaluate the function and its first (and possibly second) derivative there. This is where we run into a problem, however, since there are terms for which we cannot do this, e.g. terms proportional to $\ln(x - \xi + i\epsilon)$ or $\sqrt{x - \xi + i\epsilon}$. Additionally, the principle value integrals must have their numerators combined as seen in Eq. (5.6), which can lead to computations which are more time consuming than need be. In order to keep consistent, we instead want a method that we can apply equally well to every term, so we split the integral into three parts,

$$\int_0^1 \phi(x)dx = \int_0^{\xi-\delta_1} \phi(x)dx + \int_{\xi-\delta_1}^{\xi-\delta_2} \phi(x)dx + \int_{\xi-\delta_2}^1 \phi(x)dx. \quad (5.7)$$

We numerically integrate the first and third regions, effectively performing a principal value integration, and perform the middle integration analytically. Since the inner region is a small interval around $x = \xi$, we first expand the integrand around $x = \xi$ (or $y = 0$) to make the analytic integration feasible. Another advantage of this method, besides it being applicable to every term, is that the terms we encounter $\propto 1/y^3$ experience cancellations when we expand them around $x = \xi$. The end result of this is that the strongest divergence we have is actually $\propto 1/y^2$, which means that we need no more than the first derivative in order to fully evaluate the integral, see Appendix C.

The endpoints of the middle region hint at another issue encountered, one which is related, once again, to the evolution code. Ideally, we would have the endpoints of this region an equal distance from the center. However, due to the unequal spacing discussed above, this is not possible. Hence, the endpoints are denoted by

$$\delta_1 = x_n - x_{n-p}, \quad \delta_2 = x_{n+p} - x_n, \quad (5.8)$$

where p can be set by the user, generally the smallest value which still leaves the proper number of subintervals for Simpson's method to function, even if n is even, odd if n is odd. While it is not required for δ_1 and δ_2 to use the same value of p , we see no reason for them to differ either, and so we leave them equal. Note that having p equal does not make $\delta_1 = \delta_2$, as the spacing on either side of the point $x = \xi$ differs. This imbalance causes the expressions for the integrated terms to be significantly more complicated than they would be otherwise. As a simple example of this, consider the integral

$$\int_{\xi-\delta_1}^{\xi+\delta_2} \frac{dx}{y+i\epsilon} = 2\xi \int_{-\frac{\delta_1}{2\xi}}^{\frac{\delta_2}{2\xi}} \frac{dy}{y+i\epsilon} = 2\xi \left[\ln \left(\frac{\delta_2}{\delta_1} \right) - i\pi \right]. \quad (5.9)$$

If the endpoints of our inner region were an equal distance from ξ , the first part of the integration result, i.e. the real part, would be zero. This does not change the end result of our calculation, since the result for the middle region must compensate the two outer

regions. The mismatch between δ_1 and δ_2 simply changes the exact form this compensation takes.

The final complication comes from the endpoints of the x integration, specifically the point $x = 0$ (or $y = -\frac{1}{2}$). If we naively attempt to evaluate f_g at this point, we see that we obtain singular expressions for various terms. This can be seen fairly easily by observing that there are terms with the expression $1 + 2y$ in the denominator. However, this turns out to be a fairly minor issue, as there are multiple terms which contain this behavior, and we can show analytically that the singular terms cancel in the limit of $y \rightarrow -\frac{1}{2}$, leading to a finite result for f_g at this point. We are able, therefore, to hardcode this limit into the program which computes the expression f_g . A similar issue exists for the quark contribution, however, in that case, instead of yielding a finite result at $y = -\frac{1}{2}$, we obtain zero.

Since all of this leads to a fairly complex codebase, it was convenient to make it easy to read and debug, for this reason, each term of f_g , Eq. (3.37), is calculated separately, both for the outer and middle regions of Eq. (5.7). A detailed discussion concerning the calculation of the NLO corrections, including the expansion in the middle region, can be found in Appendix C.

5.3 Production Amplitudes

We have calculated the LO electroproduction amplitudes along with the LO and NLO photoproduction amplitudes for exclusive production of a J/ψ or an Υ , as detailed in Eqs. (3.30), (3.31), and (3.32). For consistency, unless otherwise noted, all amplitudes are calculated using variant 5 for the GPD E^g , as that one tends to reach a sort of "middle of the road" result — it's not as large as variant 4, but is generally larger than the other three variants. Figure 5.1 shows the LO and NLO non-flip amplitudes, separated into their real and imaginary parts. In order to provide a more clear picture of the importance of each component, we have divided each one by the absolute value of the total amplitude. To be precise, we take $|\mathcal{M}| = \sqrt{\text{Re}[\mathcal{M}]^2 + \text{Im}[\mathcal{M}]^2}$. For the NLO normalization, we use the full NLO amplitude, i.e. $\mathcal{M}_{LO} + \mathcal{M}_{NLO}^g + \mathcal{M}_{NLO}^q$, while for the LO one, we take only the LO

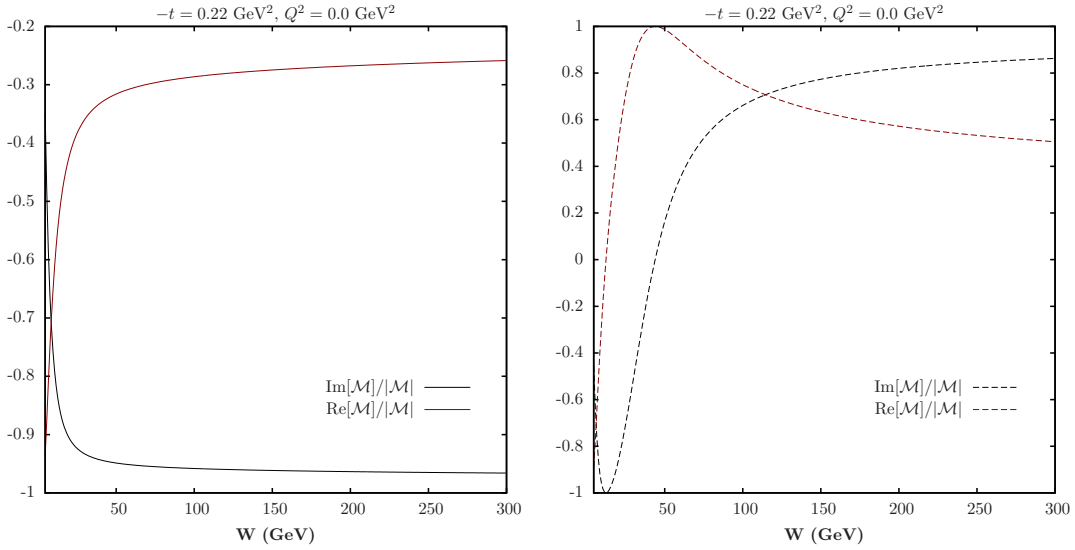


Figure 5.1: LO (left) and NLO (right) non-flip amplitudes for production of a J/ψ , separated into real and imaginary components. There is a negligible effect due to the variant of E^g chosen, here we take variant 5. See text for details on the calculations.

contribution. For plots which show only the LO or NLO results, e.g. the left or right plots in Figs. 5.1 and 5.3, we use the respective normalizations — LO for the LO plots and NLO for the NLO plots. The plots which contain both LO and NLO results, on the other hand, always use the NLO normalization, e.g. Figs. 5.2 and 5.4. These choices were made with an eye towards a meaningful comparison within each plot. For example, in Fig. 5.1 we can focus on either the left or the right plot and immediately read off the relative strength of the imaginary and real components. Accordingly, in the NLO decomposition plots, Figs. 5.2 and 5.4, we can easily determine the strength of the LO term as compared to the NLO ones.

We see from Fig. 5.1 that for the LO results, the imaginary contribution dominates the amplitude above $W \approx 25$ GeV. Additionally, at NLO, the real part dominates the amplitude at energies between approximately 25 and 60 GeV, while above this the imaginary part slowly begins to take over, dominating only at high energies.

This behavior can be explained by looking at Fig. 5.2, which shows the NLO results decomposed into the various terms that make them up — LO, gluon NLO, and quark NLO. For both the real and imaginary contributions, the LO term is generally of opposite

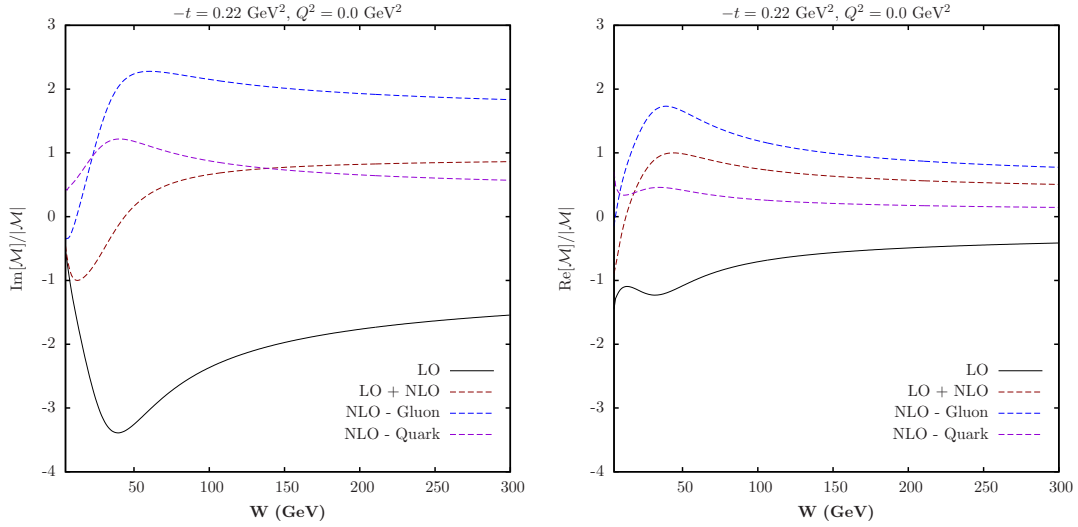


Figure 5.2: Imaginary (left) and Real (right) parts of the NLO non-flip amplitude for J/ψ photoproduction, separated into the various contributions to the full NLO result.

sign to both the quark and gluon NLO terms; however, in the case of the real contribution, the LO amplitude is smaller when compared to the gluon and quark NLO terms than in the imaginary case. While it is not enough to bring the real contribution up to the same level of the imaginary, it is able to enhance it so that one is no longer able to neglect the real amplitude at large energies.

Figure 5.3 compares the real and imaginary contributions to the spin-flip amplitude for LO and NLO. The LO results are similar to what we see for the non-flip amplitudes, but the NLO results differ slightly. In this case, the imaginary part dominates below energies of approximately 200 GeV, while above this point both contributions are important. Again, the cause of this is due to the relative magnitudes of the individual terms which make up the NLO results, as shown in Fig. 5.4. We see that for the spin-flip amplitudes the LO term is not necessarily of the opposite sign to both the NLO terms. In general, the gluon NLO term is of opposite sign to the other two contributions for both the real and imaginary parts and the relative size of this contribution is in large part what determines how important the real or imaginary parts are.

Since the spin-flip amplitudes depend directly on the GPD E^g , the chosen variant should have a much greater effect on the amplitude than in the non-flip case — where

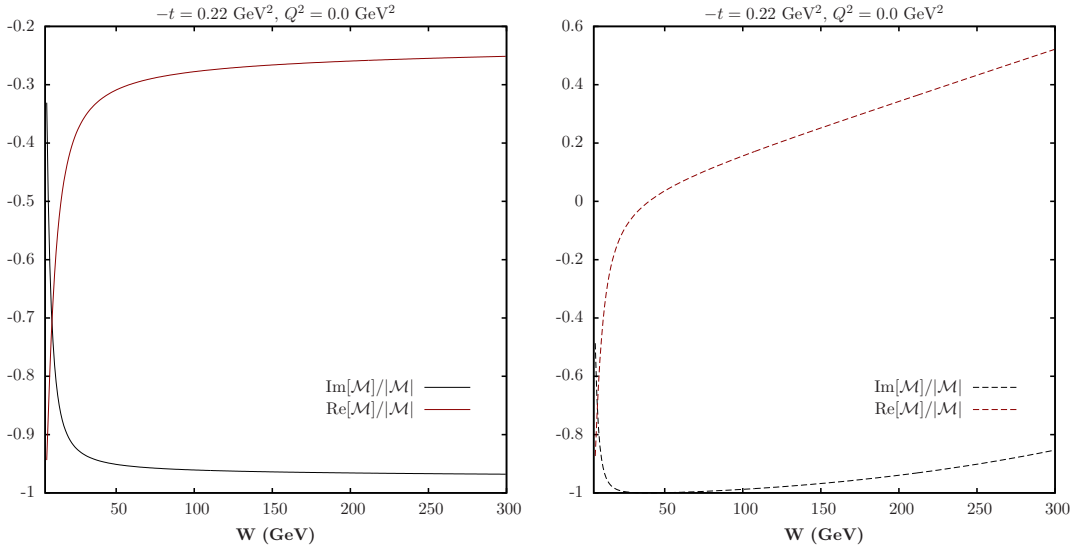


Figure 5.3: LO (left) and NLO (right) spin-flip amplitudes for production of a J/ψ , separated into real and imaginary components. See text for details on the calculations.

the variant has a negligible effect due in large part to it entering the non-flip amplitude with a prefactor of $\xi^2/(1 - \xi^2)$. Figures 5.5 and 5.6 show the LO and NLO amplitudes, respectively, for each of the five variants chosen. At LO, there is not much of a change in the overall relations between the imaginary and real contributions, except in two cases. The main differentiating factor between variant 4 and the other variants at LO is that variant 4 is of opposite sign. Additionally, in variant 1, we see the real part taking a more prominent role than in the others. At NLO, these behaviors change somewhat. Variants 2, 3, and 5 are still quite similar, and variants 1 and 4 have the greatest changes. For the imaginary part, variant 1 now is of the opposite sign as compared with the three similar variants, though the magnitude is not much different. The real part of variant 1, however, starts off with the opposite sign, but never crosses the x -axis, whereas every other variant does so. Additionally, at lower energies, variant 1 seems to have a larger real part than the others. Variant 4, on the other hand, behaves completely differently than the other variants. While the other four variants seem to reach an approximately stable ratio at fairly low energies, variant 4 has significant change above even 200 GeV.

The non-flip amplitudes for Υ production, which can be seen in Figs. 5.7 and 5.8, do not show the same drastic changes when going from LO to NLO that we see in the J/ψ cal-

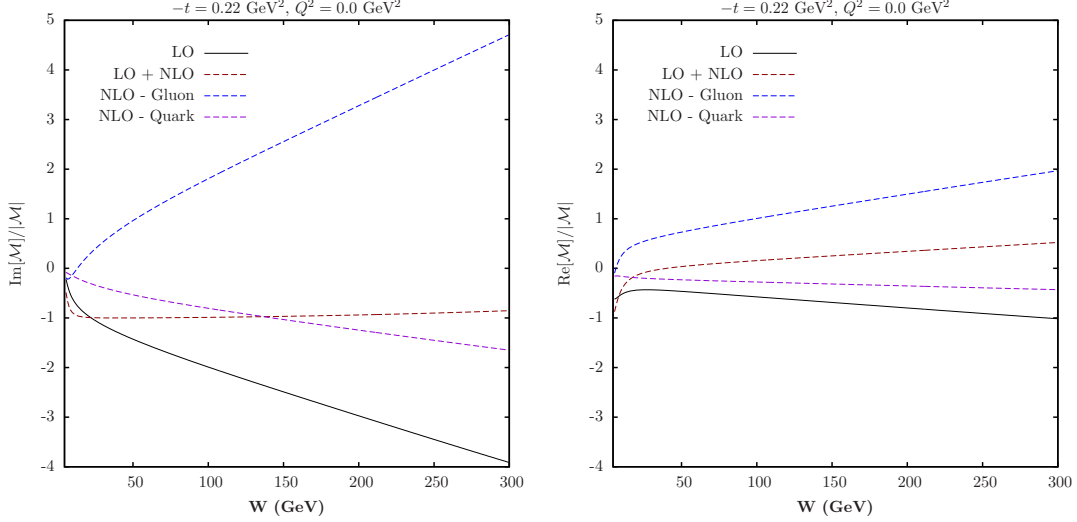


Figure 5.4: Imaginary (left) and Real (right) parts of the NLO spin-flip amplitude for J/ψ photoproduction, separated into the various contributions to the full NLO result.

ulation. At NLO, the imaginary contribution to the amplitude becomes more important, though even at LO the real part is significantly less than the imaginary, at least above 100 GeV or so. As for the various contributions to the full NLO result, Fig. 5.8 shows that the LO term is the largest, in direct contrast with the J/ψ results. The NLO gluon contribution tends to be fairly large, though still smaller than the LO one. These all lead to a conclusion that the NLO corrections for the J/ψ are not well under control, most likely due to the mass not being large enough to act as a hard scale for the process.

The stark differences seen are interesting since the meson mass is the predominant change in the calculation when going from J/ψ to Υ production. Obviously, it enters our calculation for $\alpha_S(\mu)$, where as mentioned previously, we evolve to the scale $\mu = \sqrt{Q^2 + m_V^2}$, which for photoproduction is clearly $\mu = m_V$. The results for $\alpha_S(\mu)$ at the two evolved scales are

$$\begin{aligned}\alpha_S(\mu_{J/\psi}) &= 0.251960 \\ \alpha_S(\mu_\Upsilon) &= 0.176952.\end{aligned}\tag{5.10}$$

The similar values of the coupling constant at the two scales implies that this cannot be the only factor in the instability of the J/ψ NLO correction. In the case of $W^2 \gg m_V^2$, or the limit of small ξ , the LO and NLO amplitudes simplify considerably [32] and we see that

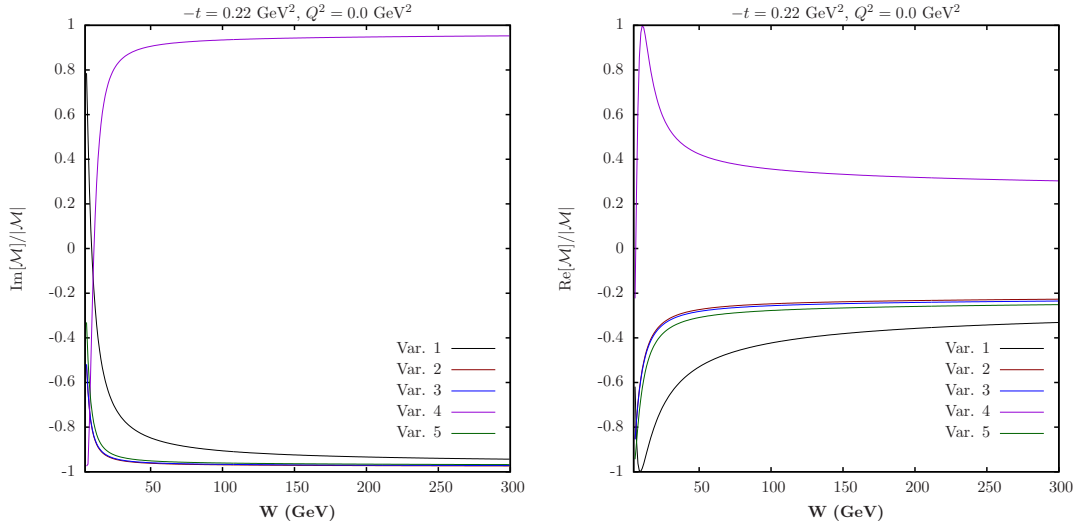


Figure 5.5: Effect of chosen variant on LO spin-flip amplitudes for J/ψ photoproduction. The Imaginary (left) and Real (right) contributions, divided by their absolute value, for the 5 investigated variants.

the NLO terms are proportional to $\log \frac{1}{\xi}$. Taking this together with the values of α_S implies that the NLO corrections for Υ are approximately half those for J/ψ production over the range we investigate.

The spin-flip amplitudes for Υ production are shown in Figs. 5.9-5.12, and once again they show a much more stable NLO result than for the J/ψ . We again see that the imaginary component becomes more prominent after including the NLO corrections, especially at energies above 75 GeV. Also, we see a similar comparison to the J/ψ results when it comes to the differences among the spin-flip amplitudes due to the variants. Variant 4, once again, varies significantly from the other four variants, while at LO variant 1 is not too different from the other three. At NLO, however, the first variant develops some characteristics which differentiates it from the other amplitudes, especially at low energies.

Due to the complexities inherent in the NLO gluon calculation, a crosscheck of the result was desired. This check was performed using the Mathematica software package [64]. Since the GPD evolution and presence of the GPD E^g will not change the basics of the check, we were able to, without loss of generality, perform the cross check at the initial

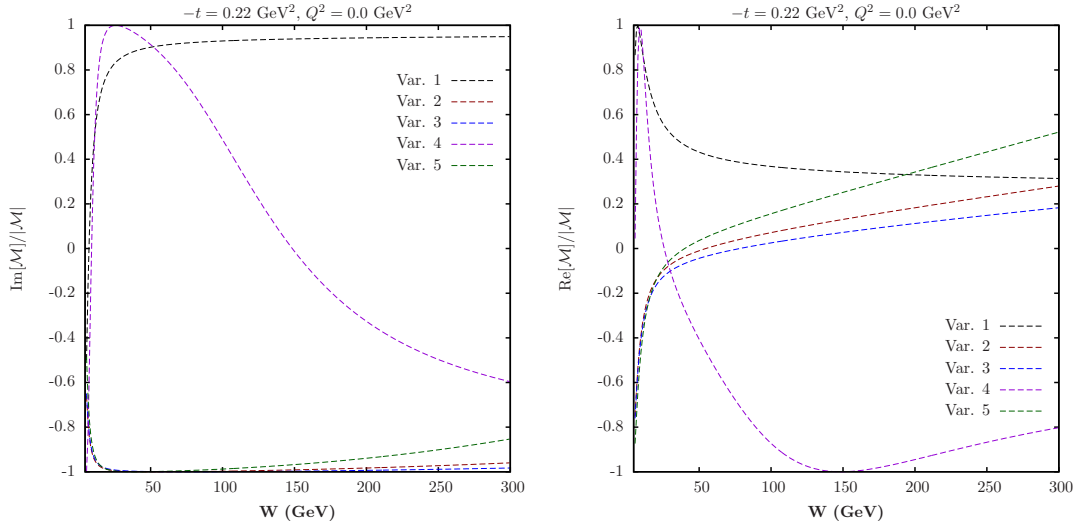


Figure 5.6: Effect of chosen variant on NLO spin-flip amplitudes for J/ψ photoproduction. The Imaginary (left) and Real (right) contributions, divided by their absolute value, for the 5 investigated variants.

scale, for the simple case of $E^g = 0$, i.e. $H_{\text{eff}}^g = H^g$. Instead of having Mathematica generate the GPD values itself, which would have taken a considerable amount of programming and runtime, we generated, via the main code, a large array, ~ 2000 points total, of values for H^g and instructed Mathematica to fit an interpolating function that describes the data. The interpolating function was generated via a 4th order spline interpolation. This provided a good description of the GPD data, and checks of the integral and derivative of the GPD at various points were performed to satisfactory results.

The next step was to verify that our method of performing the NLO integrals was appropriate. Calculations of the LO and NLO amplitudes at the initial scale were performed both in Mathematica and with the main code. The main code uses the method of separating the integrals into three distinct regions, as detailed above, while Mathematica does not. We utilize Mathematica's numeric integration routine, which requires the entire expression to evaluate to a numeric value, so we set ϵ to be a small, but positive, number, approximately $10^{-5} - 10^{-6}$. In this way, we eliminated our approximation of the terms in f_g and performed the integrals as straightforwardly as possible. We saw an agreement between the two methods on the percent level, confirming the method we use to calculate

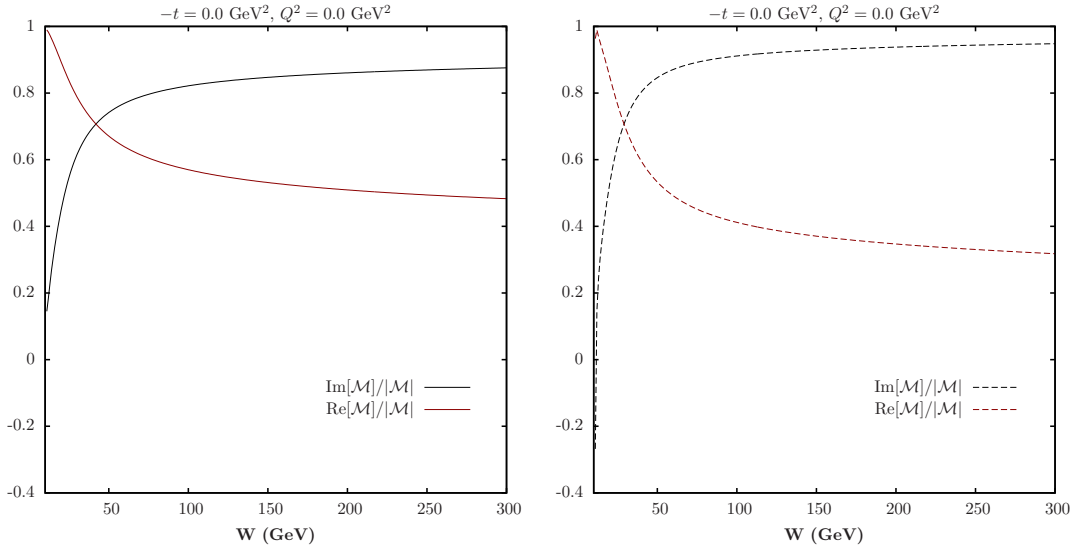


Figure 5.7: LO (left) and NLO (right) non-flip amplitudes for production of a Υ , separated into real and imaginary components. There is a negligible effect due to the variant of E^g chosen, here we take variant 5. See text for details on the calculations.

the amplitudes.

A comparison was also performed between our amplitude results and those present in the literature [32]. Figures 5.1 and 5.2 were compared to the corresponding plots in Fig. 17 of [32]. We note there are some apparent differences between the related plots. First, the right plot of Fig. 5.1 can be compared to the upper right plot of Fig. 17 in [32]. We see that in our case the real part decreases slower and remains larger than in [32], while our imaginary part increases faster but remains slightly smaller than what can be seen in [32].

Additionally, we compared Fig. 5.2 to the bottom plots in Figure 17 of [32]. If we look at the decomposition of the imaginary part into the various LO and NLO terms, we see that the overall trend is similar, but the magnitudes are slightly different. Our LO results are slightly larger in magnitude, as are our quark and gluon NLO contributions. The total result, however, is not much different in magnitude than that shown in [32]. Our real part, however, behaves significantly different. The LO result never crosses the x -axis, and its low energy behavior is quite different. Our gluon NLO contribution is larger, and again does not cross the x -axis, as it does in [32]. Finally, our quark NLO term is smaller, and has a slightly different behavior than seen in Fig. 17 of [32]. Despite the differences seen in

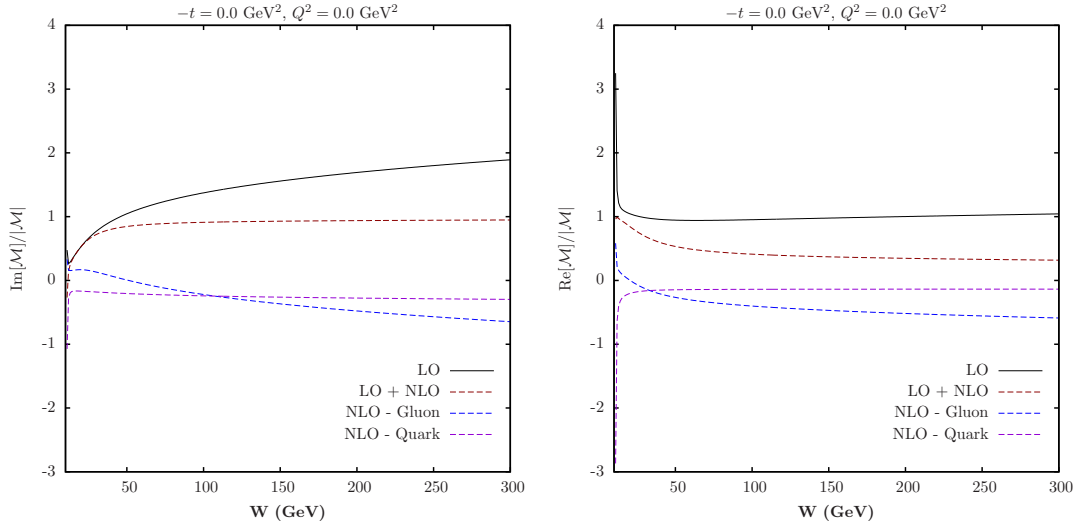


Figure 5.8: Imaginary (left) and Real (right) parts of the NLO non-flip amplitude for Υ photoproduction, separated into the various contributions to the full NLO result.

the amplitudes, we are confident that they do not spoil the overall rough agreement seen between the results of [32] and our own. The most likely cause of the discrepancies is due to the GPD model taken in each case. In [32], they utilize the results from [65], while we build on the models developed in [41, 42]. It is not unreasonable that differences in the models could lead to the observed differences. Additionally, strange behavior can be seen in the LO cross section results of [32] at low energies, while no such behavior appears in ours, strengthening the argument that the differences are due to GPD model differences.

The fact that we are looking at the ratio of the amplitudes to their absolute value, as explained at the beginning of this section, can perhaps explain why the total imaginary part is similar while the individual terms are larger than in [32]. Since our real parts are smaller than those seen in [32], it is possible that the excess seen in the imaginary part is offset by the smaller values of the real contributions.

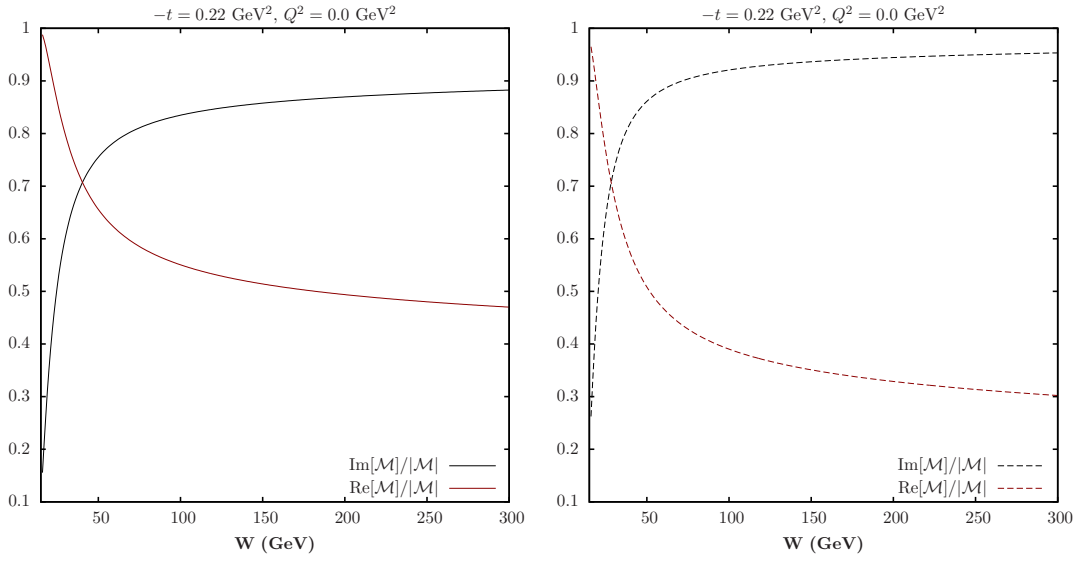


Figure 5.9: LO (left) and NLO (right) spin-flip amplitudes for production of a Υ , separated into real and imaginary components.

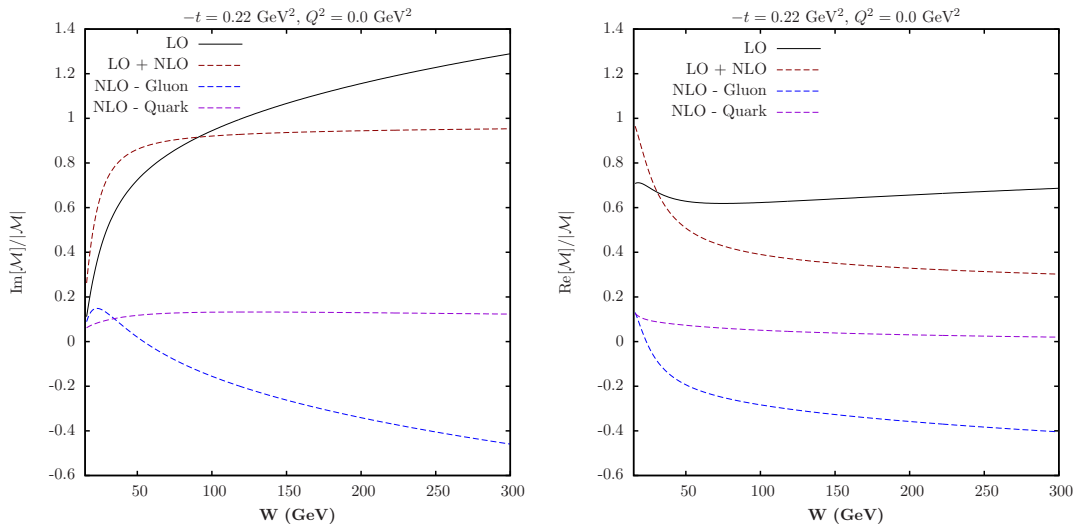


Figure 5.10: Imaginary (left) and Real (right) parts of the NLO spin-flip amplitude for Υ photoproduction, separated into the various contributions to the full NLO result.

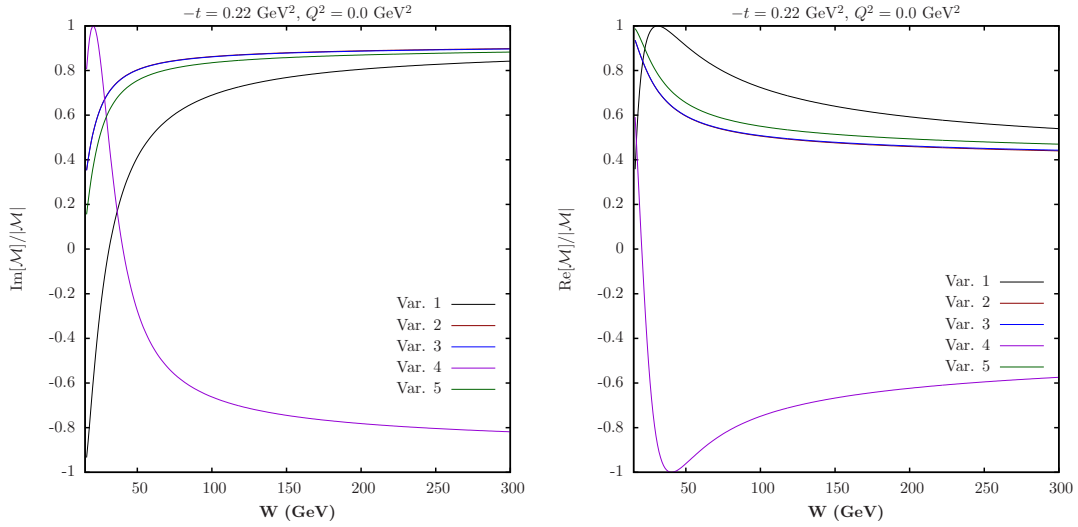


Figure 5.11: Effect of chosen variant on LO spin-flip amplitudes for Υ photoproduction. The Imaginary (left) and Real (right) contributions, divided by their absolute value, for the 5 investigated variants.

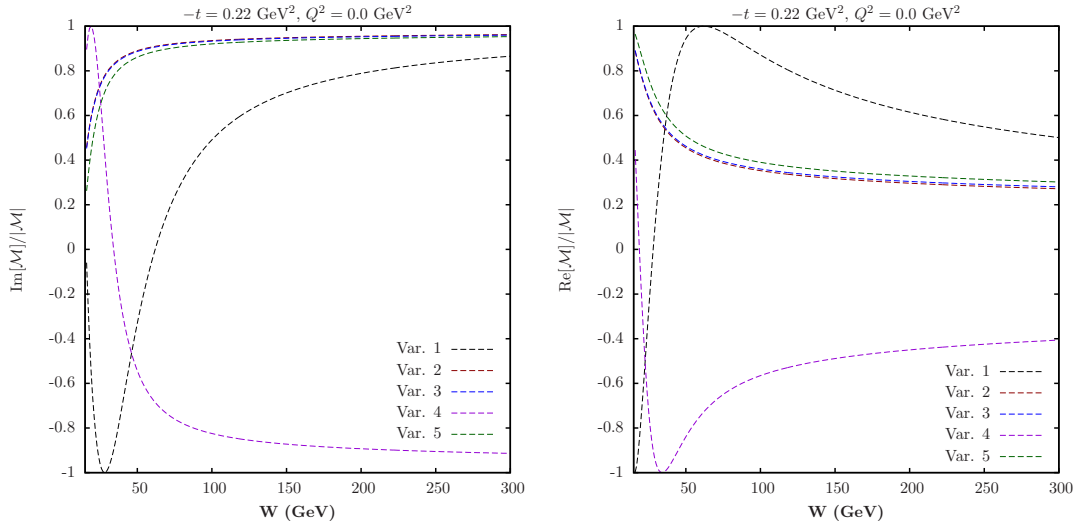


Figure 5.12: Effect of chosen variant on NLO spin-flip amplitudes for Υ photoproduction. The Imaginary (left) and Real (right) contributions, divided by their absolute value, for the 5 investigated variants.

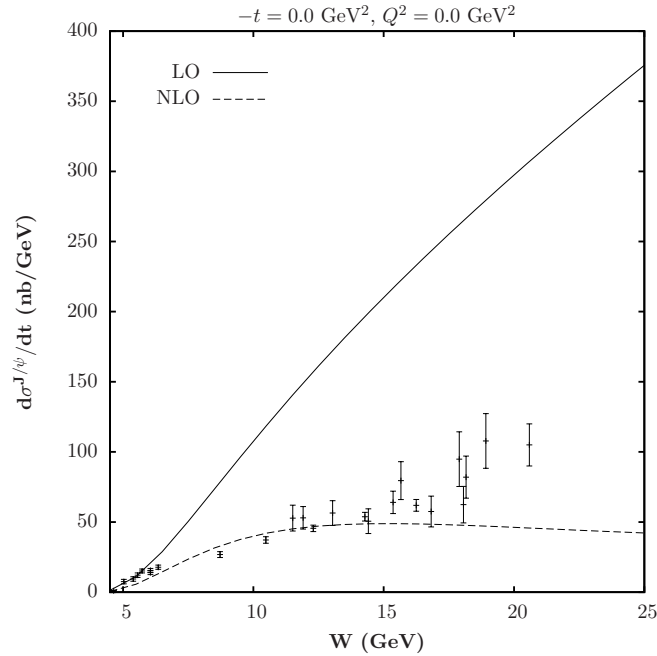


Figure 5.13: LO (solid) and NLO (dashed) results for J/ψ photoproduction at $t = 0$. Experimental data from various experiments up through 1985 [66].

5.4 Cross Sections

We will begin by inspecting the differential and integrated cross sections for exclusive production of a J/ψ in addition to the integrated cross section for Υ photoproduction. After the data has been presented, we will proceed to discuss the results. Since the unpolarized cross section is only marginally sensitive to the variant of E^g used, all plots are shown using Variant 5 because its amplitudes lie approximately between the other variants. Additionally, all results are shown at the evolved scale, given by $\mu = \sqrt{Q^2 + m_V^2}$.

Figure 5.13 shows the LO and NLO results for photoproduction with $t = 0$. We note that at LO, the calculations lie well above the experimental data, which are taken from [66], while the NLO results provide a good description below $W \approx 15$ GeV, and tend to fall below the data with increasing energy. It is worth pointing out that Ref. [66] is a review of the experimental data for J/ψ photoproduction at the time, and so contains all the cross section data available up to 1985. We also show photoproduction data in Fig. 5.14, but this time at higher energies, and for three different values of t . The experimental data in

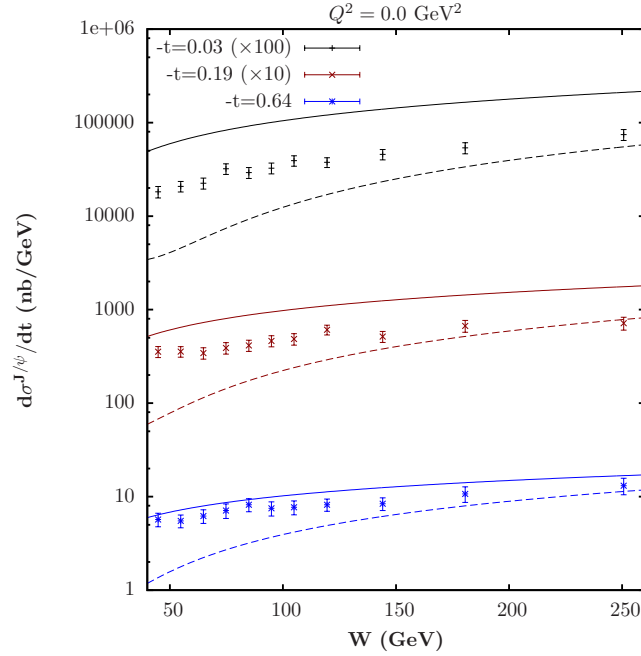


Figure 5.14: LO (solid) and NLO (dashed) results for J/ψ photoproduction at 3 different t values. Note that two sets of data have been scaled, in order to make the comparison more clear. Experimental data is from H1 [67].

this plot is from the H1 experiment, published in [67]. We again see the trend that the LO results are above the data, while the NLO ones are below. This time, however, as we increase in energy, the NLO results become a better match for the experimental data. Since these results are for larger energies, it seems that at very low (below about 15 GeV) and high (above about 200 GeV) energies, the NLO results are reasonable, while in the intermediate region it seems to underestimate the cross section. Figure 5.14 also shows that with increasing $|t|$, the theoretical calculations come more in line with experiment. Additionally, all of our results are in line with the well-known t and Q^2 dependence of the cross section, viz. as either one increases, the cross section decreases.

It is important to note that in the development of the GPDs which we use, the fitting of free parameters was done for production of light mesons. This could have an impact on the agreement for heavier mesons. For example, since the light mesons have a different t dependence than the J/ψ , it is possible that changing the t dependence of the GPDs may improve the agreement for J/ψ production.

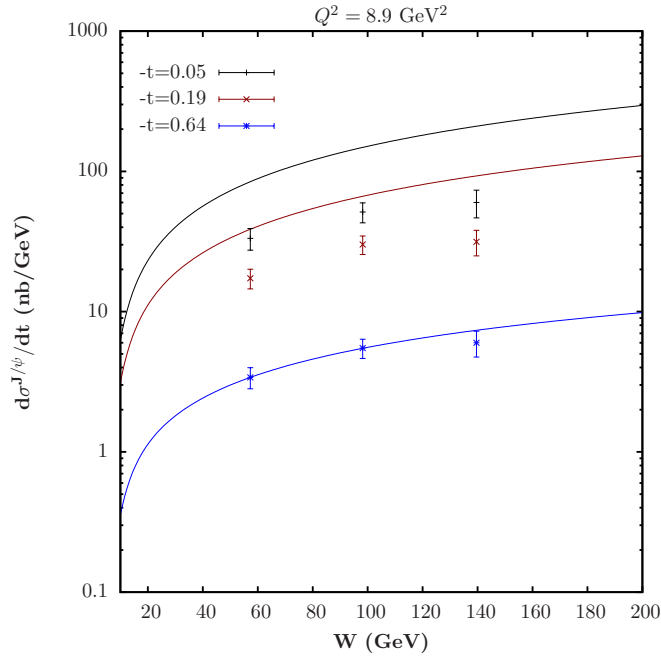


Figure 5.15: Differential J/ψ electroproduction as a function of cm-energy for 3 different values of t . LO results are for $Q^2 = 8.9 \text{ GeV}^2$, and 3 different values of t . Experimental data once again from H1 [67].

If we now turn our attention to electroproduction, i.e. nonzero values of Q^2 , we first recall that the NLO expressions are no longer valid, and so only LO results are shown. Figure 5.15 shows the results at $Q^2 = 8.9 \text{ GeV}^2$, and three different values of t .

We are also interested in how the cross section changes with a change in Q^2 . Figure 5.16 shows that as Q^2 increases, the cross section decreases, in agreement with experiment. As above, we also see that increasing $|t|$ decreases the cross section, and we have better agreement for larger values of $|t|$.

We have seen some indication of how the cross section depends on the momentum transfer to the nucleon, t , but we would like to investigate this further, as well. Figure 5.17 shows both the LO and NLO results as a function of t for two different cm-energies. Additionally, the NLO results come in under the experimental data, which agrees with the observation above, since the two energy values are in the intermediate range where the NLO results are much below the experimental data. We note that while the experimental data has a nonzero Q^2 , the value is small enough such that we can apply the NLO cor-

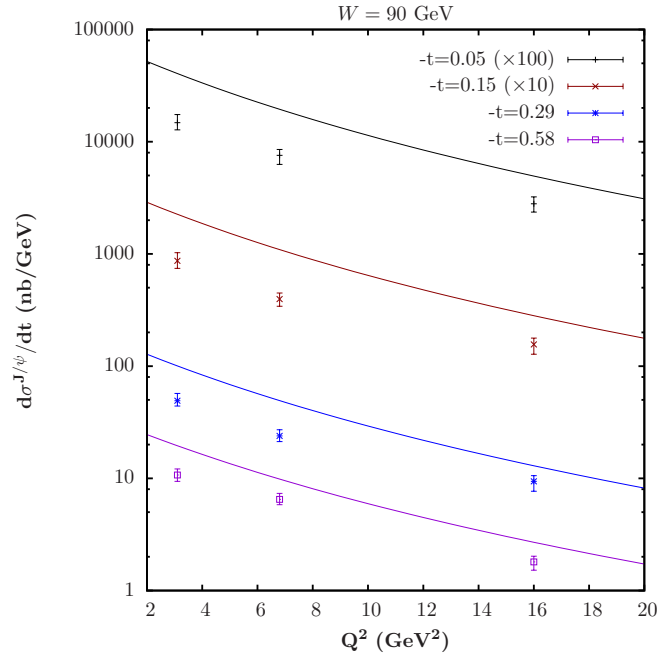


Figure 5.16: LO differential cross section results for J/ψ production as a function of Q^2 at $W = 90$ GeV and 4 different values of t . Experimental data is from ZEUS [68].

rections to this case. The longitudinal cross section is negligible, being about 0.1% of the transverse, while the expression for the amplitude would change by only about 1% if we were to include the Q^2 value of 0.1 GeV². The differential cross section for electroproduction as a function of $-t$ is shown in Fig. 5.18 along with experimental data from ZEUS [68]. We see the same behavior of a better agreement with experiment at larger values of Q^2 .

We now move on to a discussion of the integrated cross section for J/ψ production. Once again, we present results as functions of both the cm-energy W , and the photon virtuality Q^2 . Unsurprisingly, Figure 5.19 shows the same trend for the NLO results we noted earlier, viz. reasonable agreement between theory and experiment at high and very low energies, while in the intermediate region experiment is larger than theory. Additionally, Figs. 5.20 and 5.21 show a trend similar to what we saw above — as Q^2 increases, the agreement with experiment increases and we obtain reasonable agreement for the highest values of Q^2 .

Finally, we also look at Υ production, as shown in Fig. 5.22. Unfortunately, the existing experimental data is very limited — what little data there is exists only for the integrated

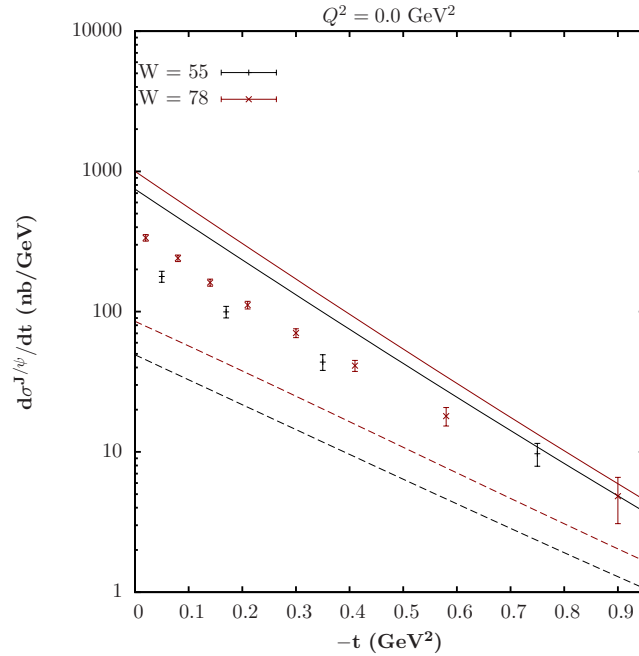


Figure 5.17: LO (solid) and NLO (dashed) differential cross section results for photoproduction as a function of $-t$. Experimental data is at a Q^2 of 0.1 GeV^2 , and is taken from H1 [69]. More details regarding the value of Q^2 can be found in the text.

cross section for photoproduction. We see right away that the LO results are in fairly good agreement with the experimental data, while the NLO results are too low. This could also be at least partly due to the different t dependence for the heavier mesons as compared with the lighter mesons for which the GPDs were fit. It is also worth noting that our Υ cross section results are in line with what was found in [32].

As noted above, the general trend we see for the J/ψ cross section with respect to the center of mass energy, W , is that at LO the photoproduction cross section is quite a bit larger than the experimental data, especially at intermediate to high energies. This disparity decreases if the momentum transferred to the proton, $|t|$, increases. At the same time, if the photon virtuality Q^2 increases, we see the same qualitative trend — the theoretical results approach the experimental data and become reasonable at large Q^2 . This comparison with experiment can seem reasonable if we recall that in perturbative QCD we perform an expansion in orders of α_S , which has a scale dependence. In the case of J/ψ , we take the mass of the meson to be this hard scale, ensuring that α_S remains small. A problem,

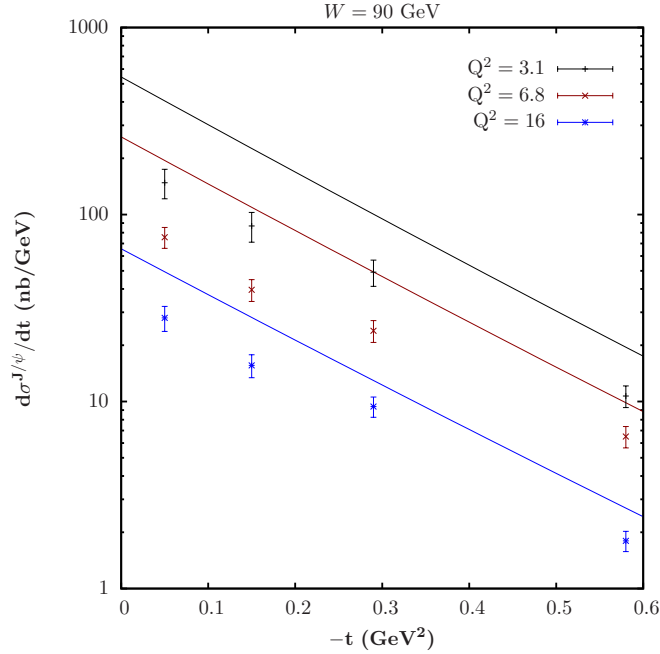


Figure 5.18: Differential J/ψ photoproduction as a function of the momentum transfer to the nucleon at $W = 90$ GeV, for 3 different values of photon virtuality. Experimental data from ZEUS [68].

however, might be that the J/ψ mass is not quite large enough to keep α_S at a reasonable size. Having a large Q^2 , then, could help to solve this issue, since it could then serve as a hard scale in place of the meson mass. As α_S decreases, the NLO corrections would start to become less and less important, and the LO results would start to come more in line with the experimental data. This could also help to explain the large NLO corrections that we see in the photoproduction results. In fact, this has been pointed out previously [32], however, it is still not clear whether this can fully account for the large NLO corrections. As the discussion in the previous section relates, the α_S values for J/ψ and Υ do not seem to differ enough to account for their very different NLO behavior.

If we do trust in the NLO results, we see that they are smaller than the LO ones, generally even falling below the experimental data. Including the corrections, however, tends to improve the agreement with experiment, especially at high energies.

The case for Υ production is not as straightforward, due to the lack of experimental data on it. It can be seen, however, that the LO results are already fairly well in line with

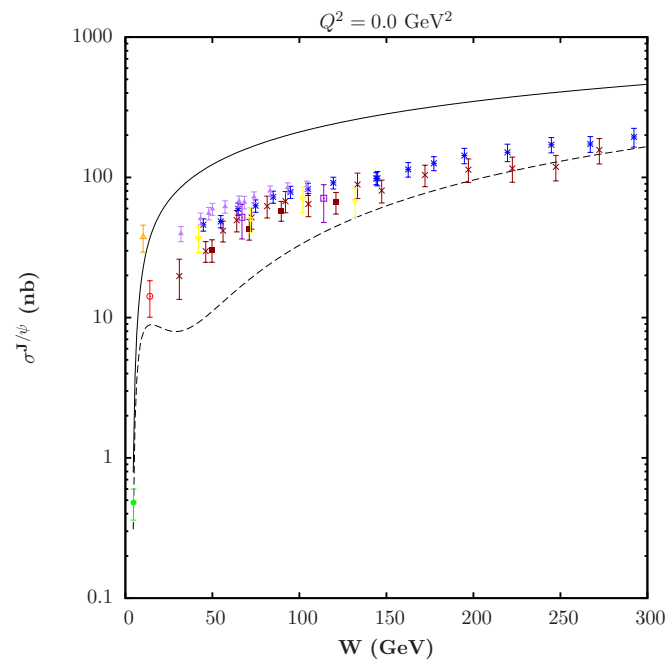


Figure 5.19: LO (solid) and NLO (dashed) integrated cross section results for J/ψ photoproduction along with experimental data from [67, 69–76].

the experimental data, while the NLO corrections cause this agreement to become worse. These corrections, however, are not as large as they are for the J/ψ , lending credence to the idea that the J/ψ mass is not quite large enough to serve as a hard scale.

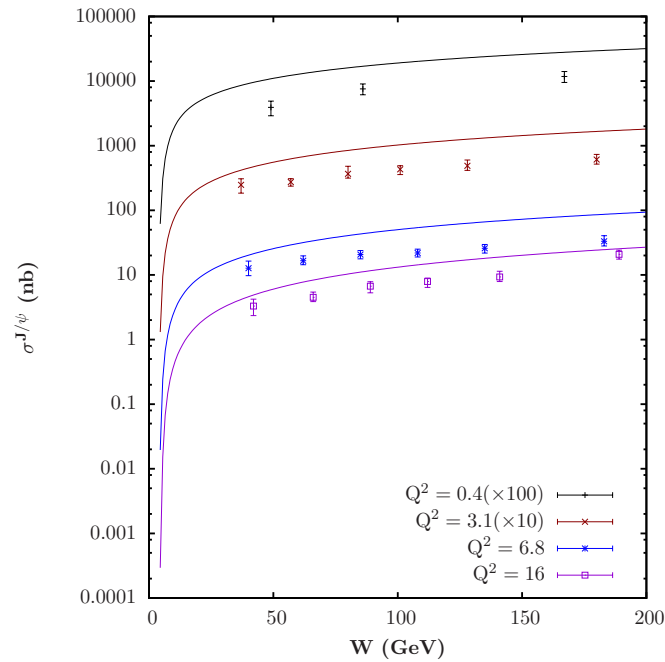


Figure 5.20: LO integrated cross section results for J/ψ production at 4 different values of Q^2 . Experimental data from ZEUS [68].

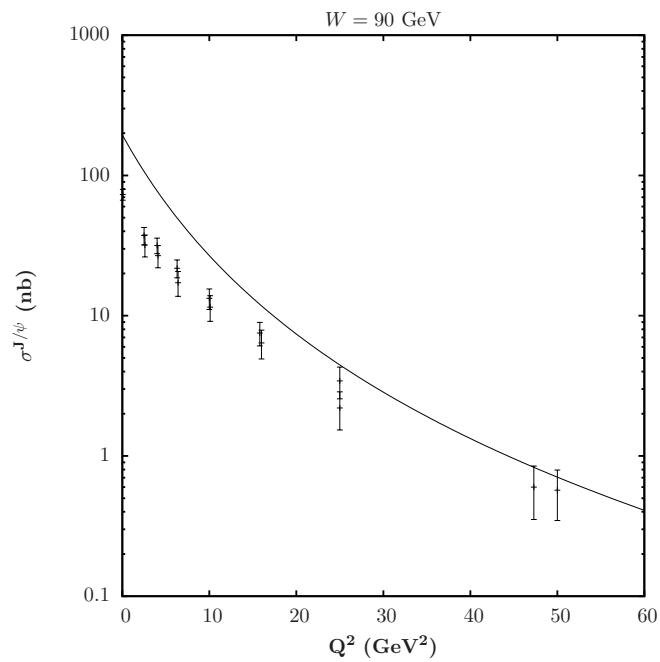


Figure 5.21: LO integrated cross section results for J/ψ electroproduction as a function of Q^2 . Experimental data from H1 [67,77].

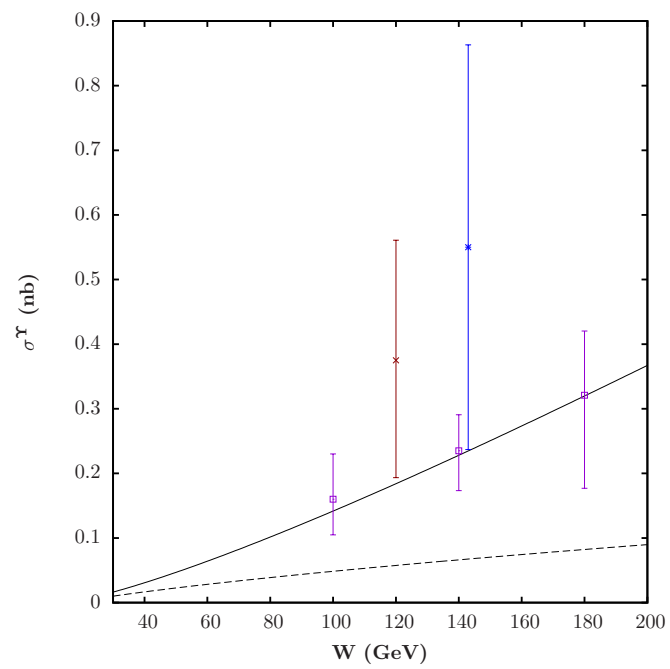


Figure 5.22: LO (solid) and NLO (dashed) integrated cross section results for photoproduction of Υ as a function of W . Experimental data is from [76,78,79]

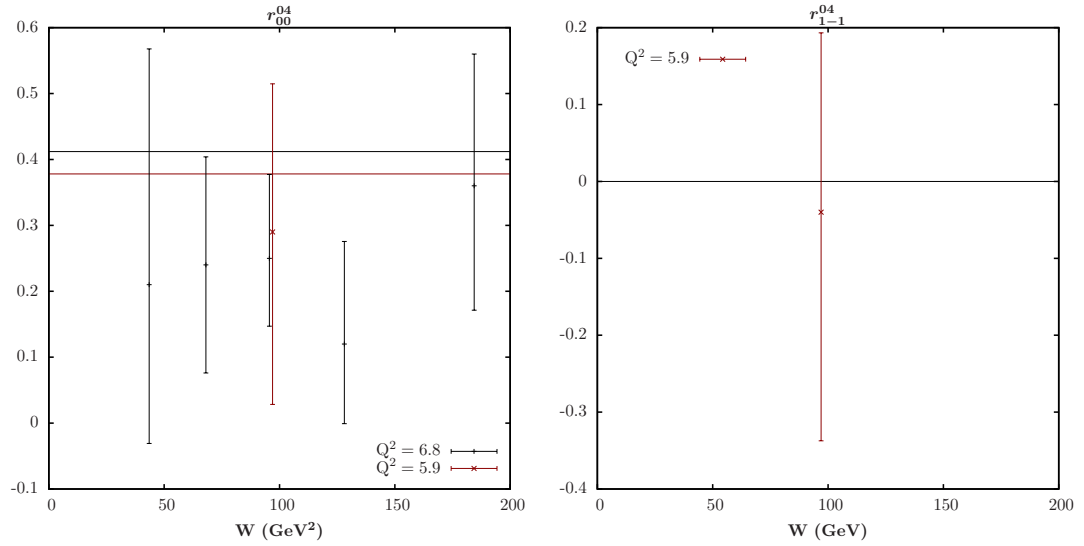


Figure 5.23: W dependence of two SDMEs for which there is experimental data available [68,80]. We predict nonzero results for r_{00}^{04} (left), and we show predictions for two different Q^2 values, corresponding to the data shown. For r_{1-1}^{04} (right), the value of Q^2 does not affect our prediction of zero.

5.5 Spin Density Matrix Elements

It is important to remember from the previous chapter that there are only two nonzero SDMEs, r_{00}^{04} and r_{1-1}^{04} as defined in (4.17) (in the notation of Schilling and Wolf [62]), in our situation. Additionally, since our predictions depend only on the photon virtuality and meson mass, plots of the SDMEs as functions of either the center of mass energy W or the momentum transfer t to the proton should both have a zero slope. This is evident in both Figs. 5.23 and 5.25, where we compare existing experimental data to our predictions at various Q^2 values. Figure 5.25 shows the t dependence of the same elements as in Fig. 5.24, which shows their Q^2 dependence. All plots are labeled in the older notation of Schilling and Wolf [62] since the experiments were conducted prior to the introduction of the newer notation by Diehl [63]. Finally, for our comparisons with experiment, we do not take NLO corrections into account, since in our situation the introduction of the NLO terms does not affect the simple relations which we obtain between the transverse production amplitudes, as seen in (3.30), and we do not have a method for computing the NLO calculations for longitudinal ones.

In general, the agreement we see between our predictions and the experimental data are reasonable, with a few exceptions, though it is important to note that the experimental data have large error bars. The W dependence shown in Fig. 5.23 is not refuted by experiment, and our results lie close to the existing data points. The results at $Q^2 = 5.9 \text{ GeV}^2$ fall within the error bounds, while the theoretical calculation at $Q^2 = 6.8 \text{ GeV}^2$ does not pass through all the data points, it does fall close to them while passing through the two points at the lowest and highest energies.

A comparison of the theoretical and experimental results for the Q^2 dependence, as seen in Fig. 5.24, does show decent agreement, with a notable exception. The Q^2 dependence of r_{1-1}^1 exhibits a behavior which is not supported by the experimental data; however, the large error bars in the data mean that there is still a bit of uncertainty, and does not give cause to reject our predictions outright. The remaining plots show a favorable comparison between theory and experiment, with most of the experimental data points lying along the theoretical curves.

The t dependence shown in Fig. 5.25 again yields a reasonable agreement with current experimental results. With the exception of r_{00}^{04} , the experimental data fall close to the theoretical predictions, with the theoretical curves often passing through the data. At very low Q^2 , $Q^2 = 0.05 \text{ GeV}^2$, the agreement is excellent; at the larger Q^2 values, however, the agreement is not as good. For these two Q^2 levels, we see that the theoretical predictions are generally above the experimental points, though there are one or two data points which seem to agree.

The level of agreement that we find between our results and experiment are expected since we find no dependence on the amplitudes in the respective SDME expressions. Instead, we find simple ratios of two basic kinematic variables — the meson mass and the photon virtuality. Again, these results do not necessarily hold in general, leading to another check of our method. Since these expressions are independent of α_S , the appropriateness of the J/ψ mass as a hard scale is not relevant. The question, then, is why we see differences at all between our predictions and experimental results. This can best be explained by the approximations we have made early on in our calculations, e.g. the non-

relativistic and collinear approximations. Relaxing these approximations would lead to production amplitudes which no longer behave according to the simple relations we find, thereby yielding more complex expressions for the SDMEs, and a dependence on the order of the calculation. Despite all this, we emphasize that for the most part, the experimental results are well described by our predictions, implying that these approximations are not unreasonable at all.

For all three cases, it is worth noting again that the error bars on the experimental data are quite large. If future experimental efforts are able to reduce these errors, it might be possible to extract some sort of kinematic dependence, which at this point is not feasible. If possible, consistency could also be determined for our predictions of a lack of W and t dependence, along with our zero-valued SDME results.

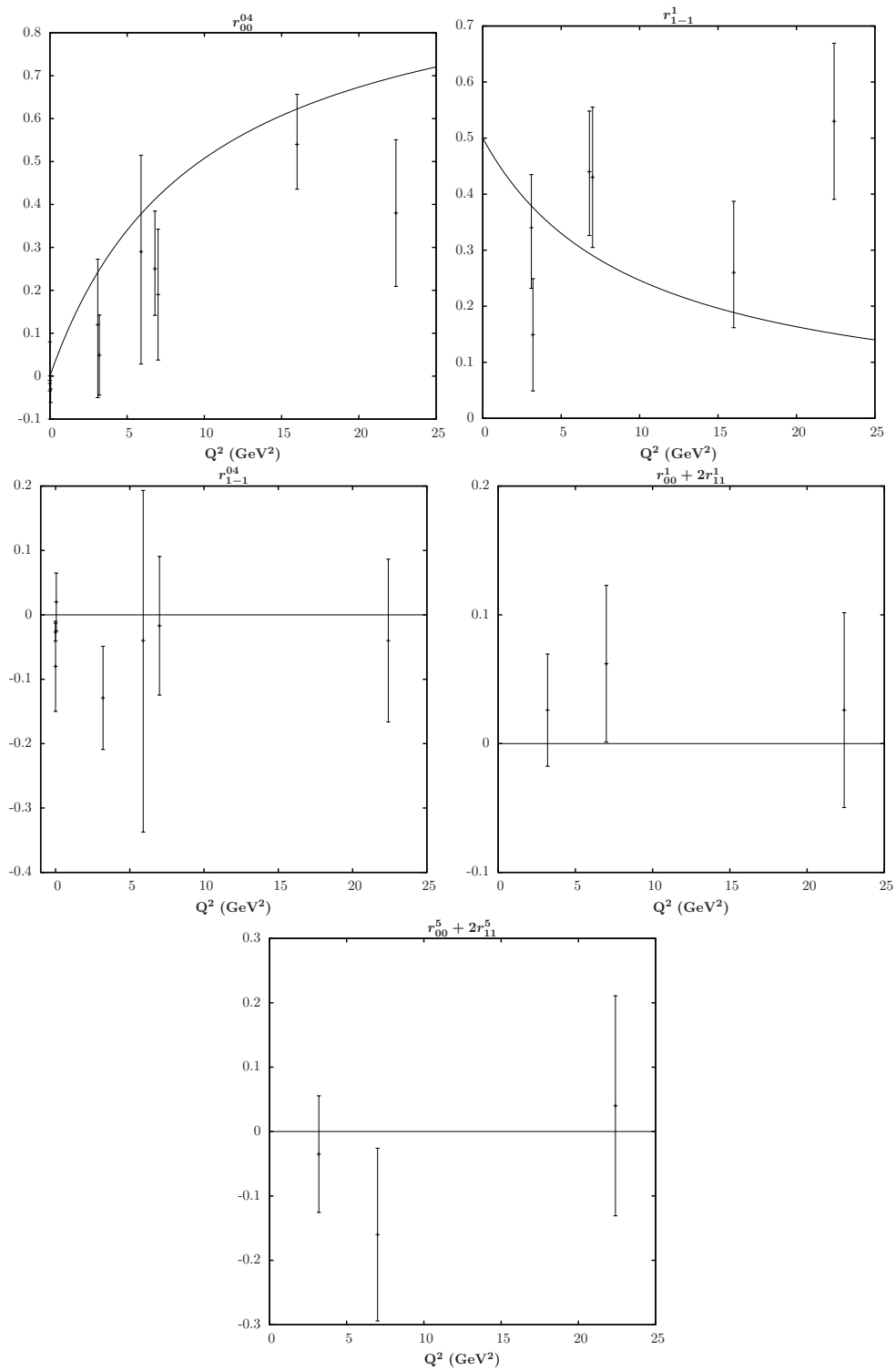


Figure 5.24: Q^2 dependence of five SDMEs for which there is experimental data available [67,68,75,78,81]. Note that for only the top two plots do we predict nonzero results.

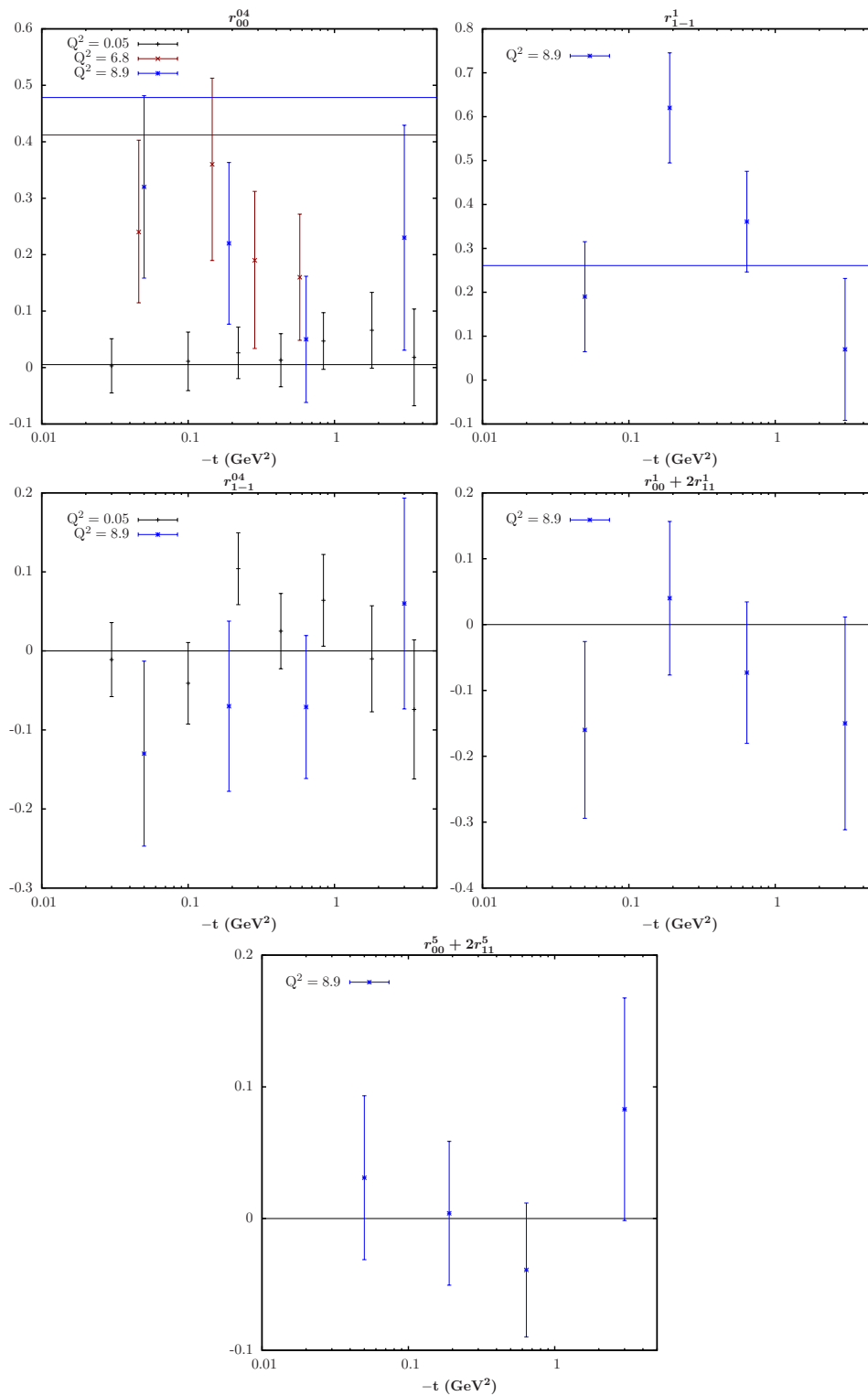


Figure 5.25: t dependence of five SDMEs for which there is experimental data available [67,68]. The magnitude of Q^2 affects only those predictions which yield nonzero results, viz. r_{00}^{04} and r_{1-1}^1 .

	A_N
Exp.	-0.05 ± 0.12
Var. 1	-0.012
Var. 2	0.053
Var. 3	0.065
Var. 4	0.196
Var. 5	0.054

Table 5.1: Results for the SSA A_N for ϕ electroproduction with $W = 4.5$ GeV, $Q^2 = 1.9$ GeV², and integrated over t from 0 to -0.5 GeV². Experimental result is from HERMES [82,83].

5.6 Asymmetries

We start off a discussion regarding the spin asymmetries by noting that there is currently no data for A_N or A_{LS} for the heavy mesons we investigate. We do, however, have some constraints on our variants in the form of existing A_N data for light mesons, though there is not currently much, and the error bands are large. There is currently a single data point for the SSA A_N for exclusive ϕ production [82,83]. Table 5.1 shows this result, along with our predictions for each variant. Additionally, there are two experimental results for ρ^0 production, one integrated over t [84], the other for a single kinematic point [85]. The results for each of these two cases can be found in Tables 5.2 and 5.3, respectively. Note that in these cases the meson has a small mass, insufficient to serve as a hard scale, so that we must go to electroproduction and are therefore unable to compute NLO corrections. The amplitudes are therefore completely determined on the basis of Eqs. (3.41) and (3.42).

All three cases tend to yield favorable results when compared with experiment. This is surprising if we note the low value of Q^2 for which the measurements are performed, similar to or even smaller than the J/ψ mass. We would expect that if the J/ψ mass is arguably too small to successfully employ a perturbative approach, then so too would these low Q^2 values be. Instead, what we find is that the theoretical predictions fall within the error bands of the experimental results, with the exception of one, excessively large, variant for E^g . Despite this contradiction with the data, we do not discard this variant, on the basis that these are mostly preliminary data points

	A_N
Exp.	-0.033 ± 0.058
Var. 1	-0.0309
Var. 2	0.0027
Var. 3	0.0089
Var. 4	0.1035
Var. 5	-0.0038

Table 5.2: Results for A_N for ρ^0 production, integrated over t . $W = 5$ Gev, $Q^2 = 3.07$ GeV², and $\int_{t_{\min}}^{-0.4} dt$. Experimental data from HERMES [84].

	A_N
Exp.	-0.035 ± 0.103
Var. 1	-0.0488
Var. 2	0.0149
Var. 3	0.0251
Var. 4	0.2330
Var. 5	0.0029

Table 5.3: Results for A_N for ρ^0 production for a single kinematic point. $W = 5$ Gev, $Q^2 = 1.95$ GeV², and $t = -0.13$ GeV². Experimental data from HERMES [85].

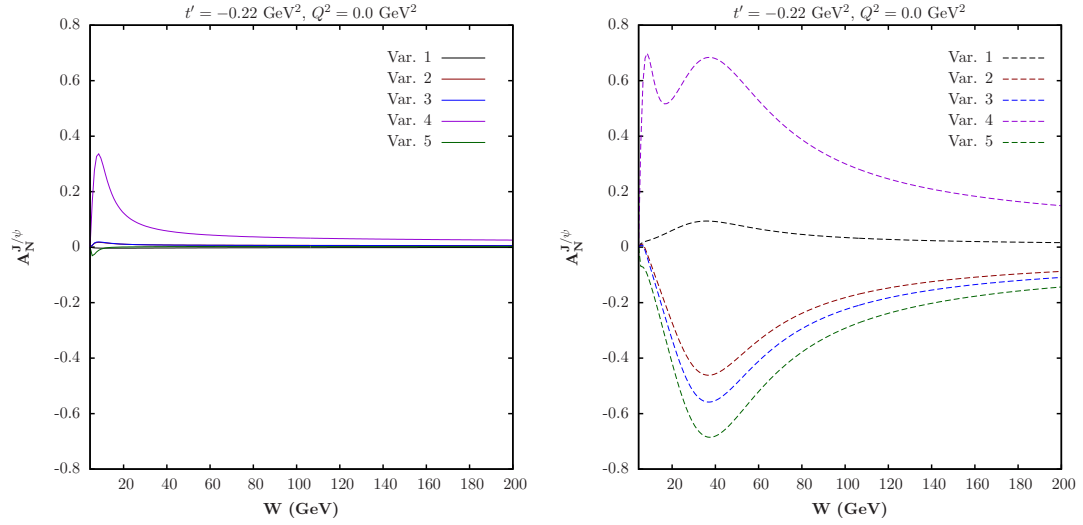


Figure 5.26: LO (left) and NLO (right) SSA A_N results for J/ψ photoproduction as a function of W .

Figure 5.26 shows both LO and NLO A_N results for J/ψ photoproduction. These were obtained at a momentum transfer of $-t = 0.22$ for a range of center of mass energies W . At LO, all the variants yield small asymmetries over much of the energy range. They grow in magnitude slightly at smaller energies, other than Variant 4, which shows a large increase below about 20 GeV. Still, if the goal is to measure A_N in order to obtain information about E^g , the LO results do not give much hope. The picture changes, however, when we look at the NLO calculations. We see that the different variants are easy to distinguish at most energies, and their magnitudes are much larger, with a maximum around 40 GeV. Throughout our discussion of J/ψ production, we note that the NLO corrections are quite large, which is what we also saw in the amplitude and cross section results. The fact that the asymmetries change so much, however, was not a foregone conclusion since higher order corrections often tend to be less significant in asymmetries. This, clearly, is not the case here; the NLO corrections to the asymmetries are at least as large as those to the cross sections. For this reason, while we still discuss the NLO results in terms of the advantages of one asymmetry over the other, for J/ψ at least, we trust the LO results more than the NLO ones.

Figure 5.27 is the same as 5.26, but for the DSA A_{LS} . The LO results are more promising

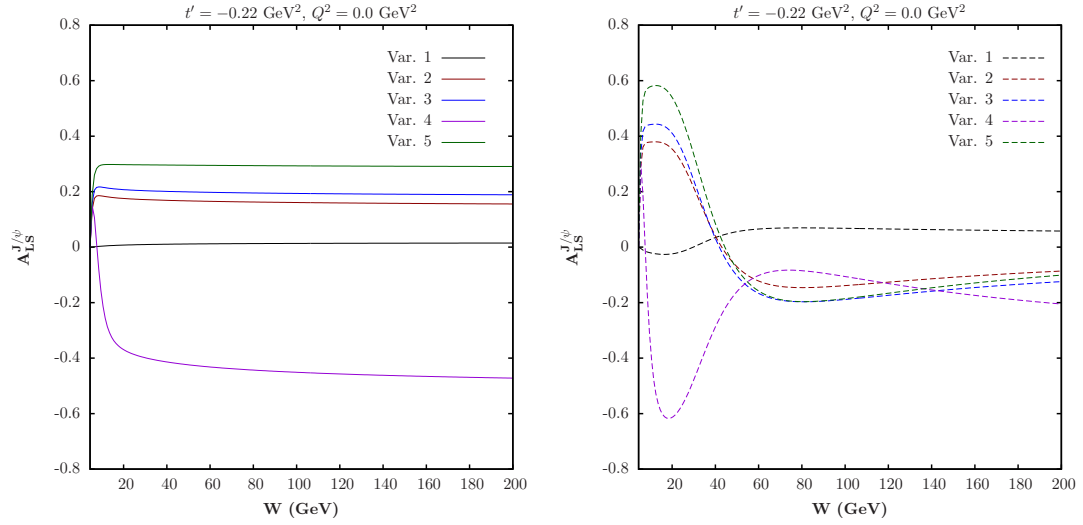


Figure 5.27: LO (left) and NLO (right) DSA A_{LS} results for J/ψ photoproduction as a function of W .

than those for A_N — not only are the magnitudes for all the variants larger, but it is possible to distinguish among them, especially at higher energies. The NLO results, then, add a bit of confusion to the picture. For a large range of energies, it is harder to distinguish among the different variants, and we get little to no increase in the magnitudes. The exception is for low energies, around 20 GeV and lower the asymmetry becomes larger than at LO, and it becomes easier to distinguish among the variants.

If we turn now to inspect how the asymmetries appear as function of the momentum transfer to the proton t , we see a similar change going from LO to NLO. For A_N , we get Fig. 5.28, and we see that just as in the case above, at LO the magnitudes are small and we cannot distinguish among the different variants. Going to NLO rectifies this situation — not only are the magnitudes of the different variants larger, but it is possible to distinguish among them. Additionally, we see that at LO, the higher we go in $|t|$, the better off we are, while at NLO an ideal value would be around $-t = .5 \text{ GeV}^2$. Beyond this point, the different variants do not diverge from one another, but the magnitudes do decrease.

Again, comparing A_{LS} to A_N yields a similar conclusion here as it does for the W dependence. From Fig. 5.29, we see that at LO A_{LS} gives, without question, an easier way to distinguish among the 5 variants, in addition to larger magnitudes. At NLO, however,

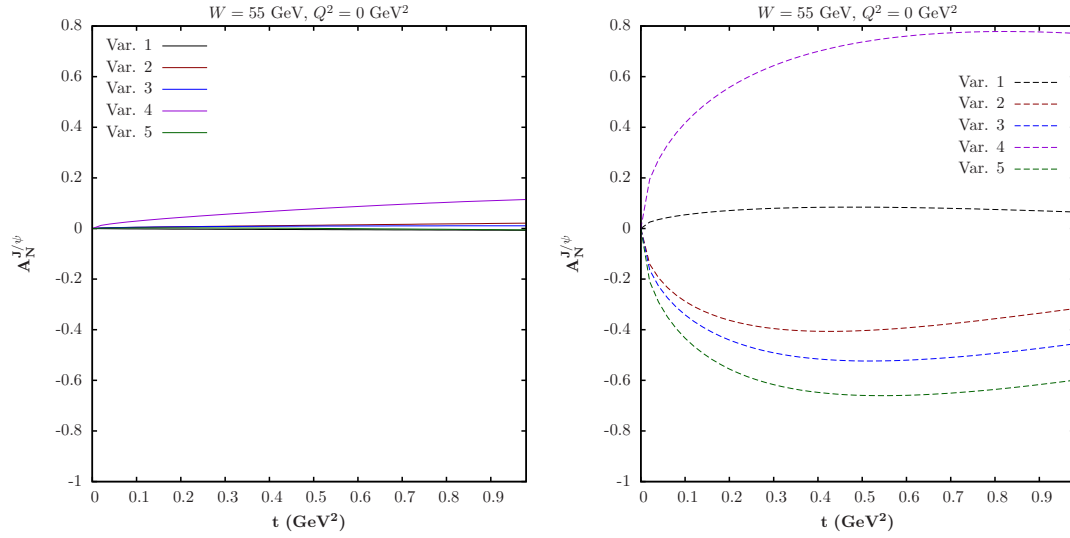


Figure 5.28: LO (left) and NLO (right) SSA A_N results for J/ψ photoproduction as a function of t .

things are not as clear; every variant displays a smaller asymmetry, and it is harder to distinguish among them, especially variants 3 and 5.

If we now look at the asymmetries for J/ψ production as a function of Q^2 , we see the same qualitative comparison between A_N and A_{LS} . From Fig. 5.30, it seems clear that A_N is a poor choice when compared with A_{LS} — the magnitudes for each variant are quite small, and because of this, it is hard to distinguish among them.

It seems clear that the NLO corrections are considerable when it comes to the asymmetries. As we will see shortly below, the dramatic change that occurs for J/ψ production is not replicated when we look at Υ production. This lends some credence to the idea that the J/ψ mass may not be quite large enough to serve as a hard scale. If this is the case, then going to high Q^2 electroproduction may yield results which are more well behaved and provide a better testing ground for experiment. In this case, A_{LS} is a better probe of E^g , if the experimental errors can be kept to a reasonable level. Not only are the magnitudes greater, but since there is a greater separation among the five variants, A_{LS} would provide greater constraints on E^g .

As for the ideal kinematics for a potential experiment, A_N would benefit most from a measurement at lower center of mass energies. On the basis of the NLO results, a W

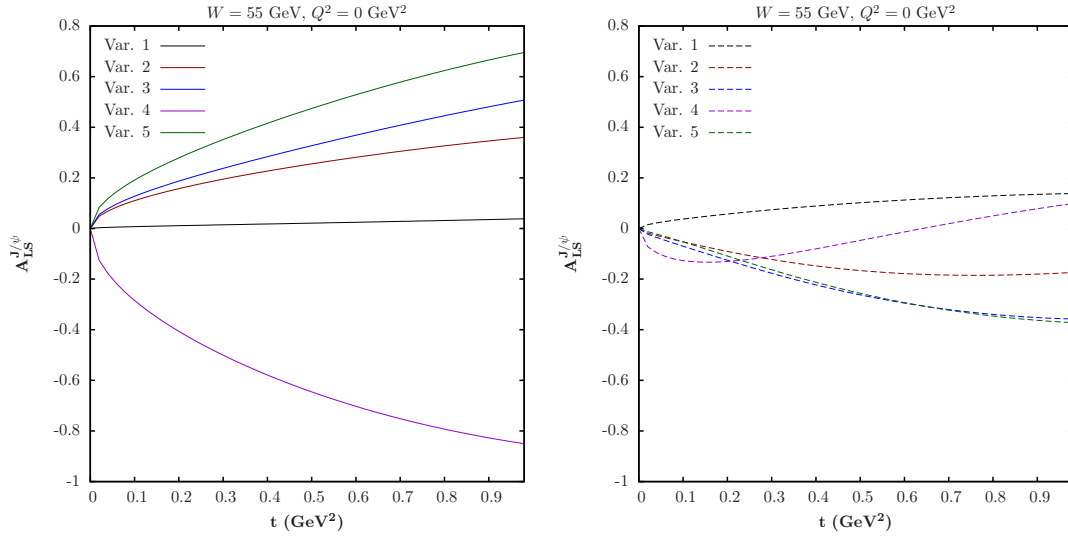


Figure 5.29: LO (left) and NLO (right) DSA $A_{LS}^{J/\psi}$ results for J/ψ photoproduction as a function of t .

around 40 GeV would be ideal — the asymmetry is largest here, and a change in the model parameters leads to a large change in the magnitude. Even if one does not trust the NLO results, going lower in W would still lead to useful constraints. In this region, variant 4 is much larger than the other variants; a small value for A_N would remove the possibility of E^g being this large, while a large value would recommend it. This would also serve as a check of the results for the ρ^0 and ϕ asymmetries, which found that variant 4 was not favored. If possible with the experimental setup, a measurement of A_{LS} would be even better. In this case, a center of mass energy around 20 GeV would be ideal, both the LO and NLO results yield fairly large asymmetries at this point, with a large separation among the variants. For both asymmetries, additional measurements at larger energies could possibly serve to determine the behavior of the W dependence, which could be another indication of whether the NLO results are not to be trusted.

The t dependence of both asymmetries shows the same trend at LO — as $|t|$ increases, so too does the asymmetry. This is reasonable since the flip amplitude directly depends on this quantity. At NLO, the same trend can be seen for A_N , but for A_{LS} it depends on the variant. Additionally, the NLO results for A_N are larger than the LO ones, while the opposite is true of A_{LS} . Despite these differences, a measurement of either asymmetry at

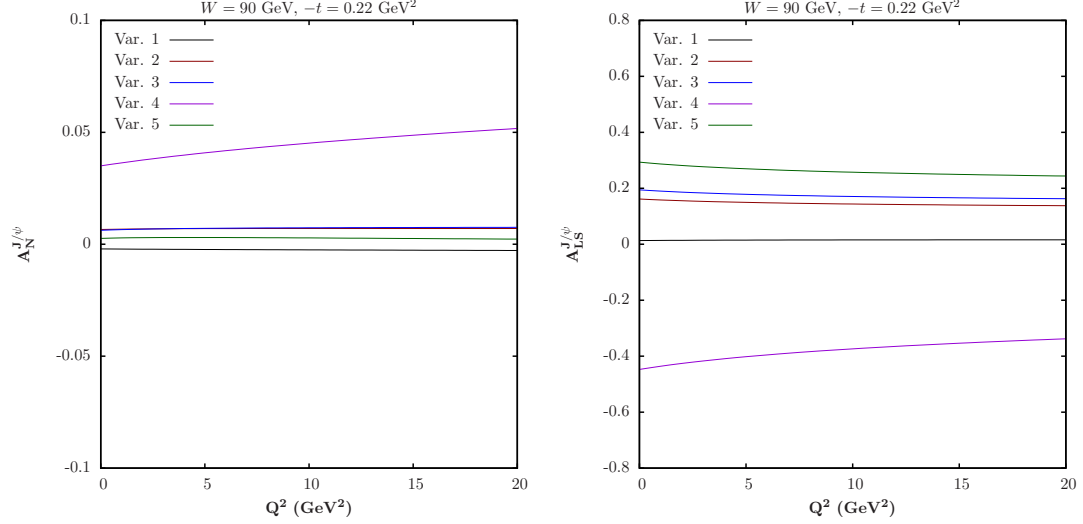


Figure 5.30: A_N (left) and A_{LS} (right) results for J/ψ production as a function of Q^2 . Note that the scale of the two plots are different.

a $|t|$ of about 0.6 GeV^2 would yield the greatest constraint on E^g . For A_N , this would also potentially yield the largest magnitude, while for A_{LS} , even though the magnitude may be greater at larger $|t|$, the separation of the variants is not as clear. Additionally, the apparent $|t|$ dependence of the asymmetries means that measurements at various $|t|$ values may not always yield more constraints, though it could eliminate E^g models similar to variant 4, which shows a different t dependence than the other ones.

Unfortunately, the NLO expressions are valid only for photoproduction, so we cannot compare the LO and NLO results for arbitrary Q^2 . If we believe that at higher Q^2 the NLO corrections should become less important, however, measurements at large Q^2 would be ideal from a theoretical point of view. There is only a slight decrease in the magnitude of A_{LS} for each variant, and A_N sees an increase in magnitude for most variants. Again, A_{LS} is an attractive prospect due to the much larger magnitudes, which also lead to greater separation among the variants, and therefore, greater constraint on E^g .

Figures 5.31 and 5.32 show the LO and NLO results for both asymmetries for Υ photoproduction. In contrast to the J/ψ case, the LO and NLO results are much more similar. When comparing the LO and NLO results, we see the same general curve for each variant, the NLO results are simply larger. We also see in Figs. 5.33 and 5.34 that the t dependence

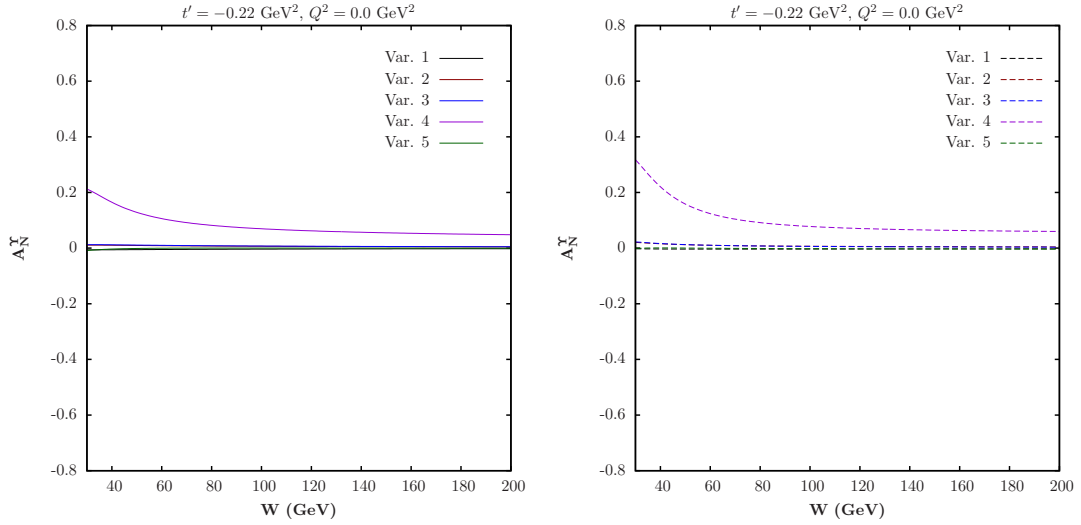


Figure 5.31: LO (left) and NLO (right) SSA A_N results for Υ photoproduction as a function of W .

of the asymmetries does not change much when going to NLO for Υ production, in contrast with the J/ψ case.

We clearly see that Υ photoproduction yields results which are much more well behaved than for the J/ψ when comparing the LO and NLO calculations. This is not that surprising based on the results for the amplitudes, since for the J/ψ case the total amplitude is dominated by the NLO terms, especially the quark contribution; while for Υ the LO term is the dominant one, leading to NLO results which are more in line with the LO ones.

While the magnitudes of the asymmetries increase when going to NLO, the W dependence does not, showing that the NLO corrections are well under control for Υ production. Measurements of A_N would best be performed at small center of mass energies, even as low as 30 GeV. At this point, data could rule out the possibility of either a large value for E^g , as in variant 4, or a small to medium value, as in the other variants. Measurements of A_{LS} , however, would be more illustrative of the importance of E^g . In this case, going to larger energies would be preferred, as the magnitudes are expected to be greater, and the separation of the variants is greater, meaning a greater constraint on E^g . Additionally, a large $-t$ is preferred, as the asymmetries increase with increasing $-t$, while for A_{LS} the

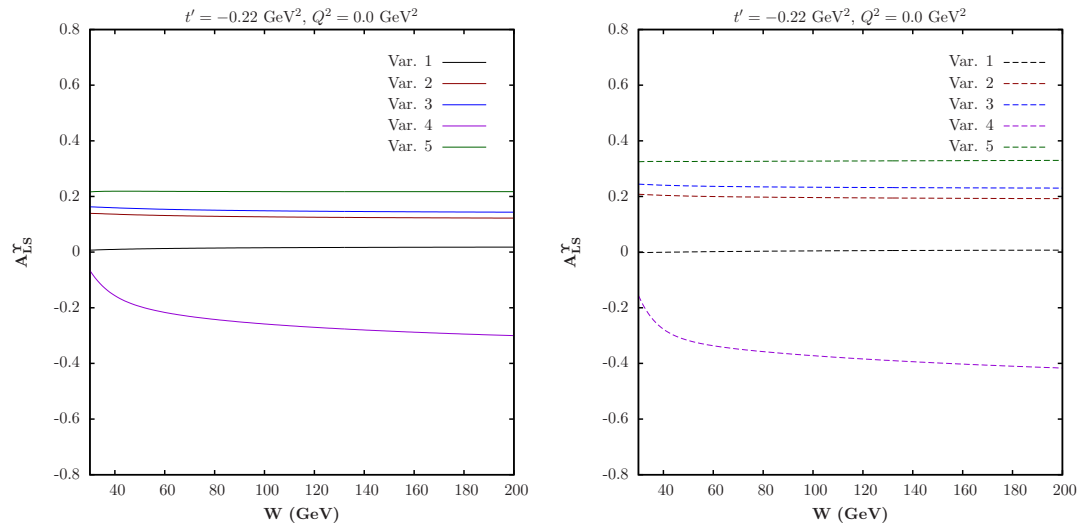


Figure 5.32: LO (left) and NLO (right) DSA A_{LS} results for Υ photoproduction as a function of W .

variants are still easily distinguishable.

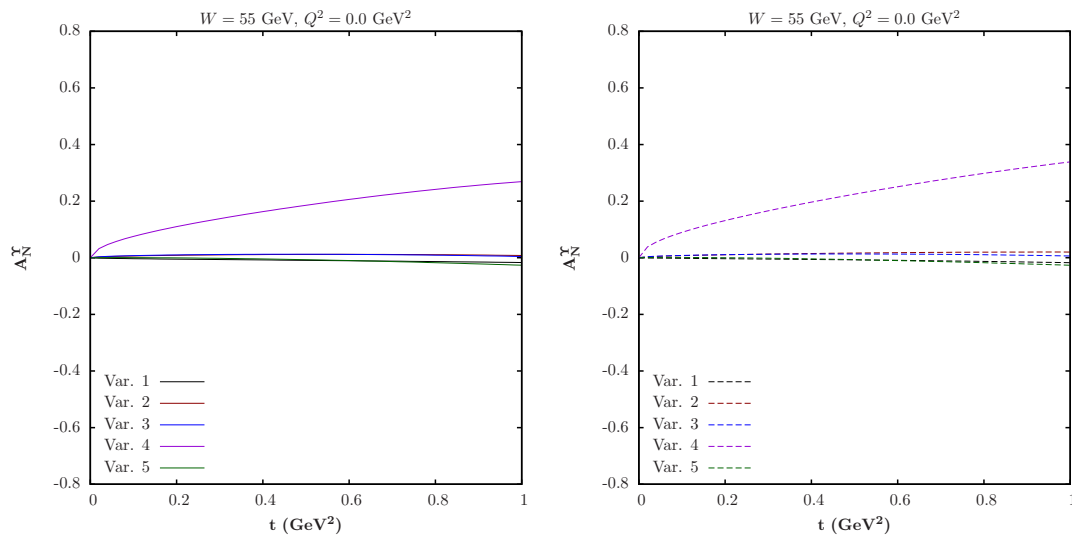


Figure 5.33: LO (left) and NLO (right) SSA A_N^γ results for Υ photoproduction as a function of t .

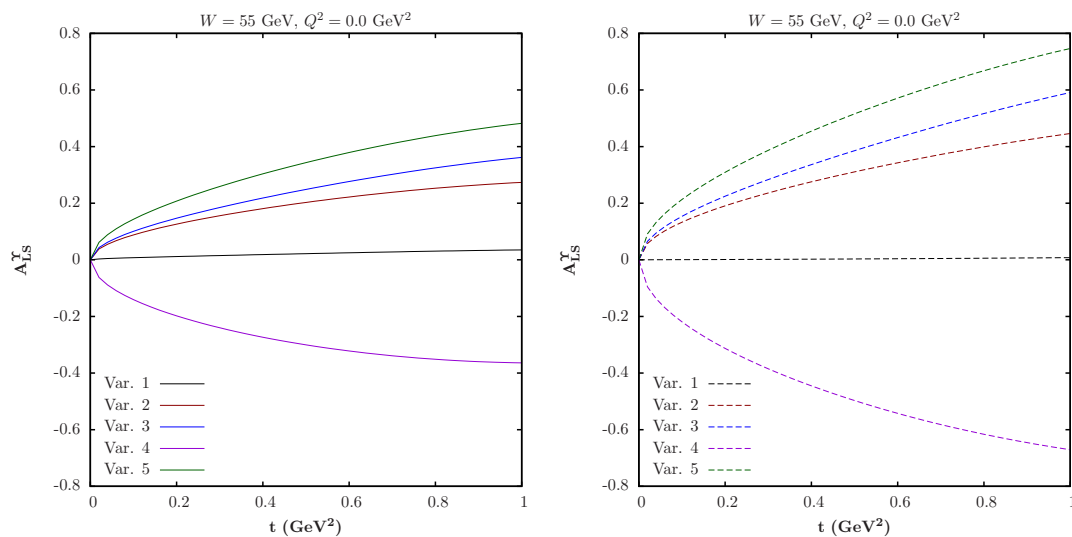


Figure 5.34: LO (left) and NLO (right) DSA A_{LS}^γ results for Υ photoproduction as a function of t .

CHAPTER 6

CONCLUSION

We have investigated exclusive photo- and electroproduction of quarkonia (J/ψ and Υ) off the nucleon in the framework of collinear factorization and GPDs. This process is generally considered to be a very good probe for the gluon structure of the nucleon. Our particular focus has been on the GPD E^g , which plays an important role in Ji's spin sum rule of the nucleon and for the 3-dimensional imaging of the nucleon. Since there is hardly any concrete information on this GPD up to now, we have developed a number of variants using double distributions as starting point, and taking all the existing model-independent constraints into account. Three of the variants for E^g are rather "traditional", while the other two are more unconventional, including a node at a certain point in x . Also, we have analytically calculated the LO amplitudes for exclusive quarkonium production, confirming previous work [31], in particular the result that the gluon helicity distribution and the distribution of linearly polarized gluons in an unpolarized nucleon, which is expected to be large, is not probed.

We evolved the GPDs using existing code by Vinnikov [27]. One interesting result of the evolution was that our first variant of E^g , which we initialize to zero, develops a node upon evolution. While this finding does not imply that a node is necessary, it does add substance to the idea that a node is physically possible. Additionally, we find no evidence that the inclusion of a node automatically disqualifies a variant based on existing data, though the location of the node has a large impact on the size of the GPD. In fact, based on existing asymmetry data for ϕ and ρ electroproduction, we determine that one

of our variants with a node yields results that are larger than the experimental. While this at present does not mean that it can be disqualified completely, it does raise concerns regarding its size.

Numerical results for the unpolarized cross section were compared with experimental data for the production of J/ψ and Υ . The LO cross section data for J/ψ is clearly larger than the experimental data, while for photoproduction the NLO corrections overcompensate and cause the results to underestimate the data. The fact that the NLO corrections are so large suggests that higher order corrections are not well under control. This finding confirms the verdict reached by Ivanov *et al* [32] though there are some discrepancies between our numerical results, which most likely are caused by the different input for the GPD H^g . For Υ production the perturbative expansion for the unpolarized cross section behaves somewhat better. This improvement should mainly be due to the larger scale implied by the heavy mass of the Υ meson. Overall, the results are concerning because at present J/ψ production is theoretically not under control, but on the experimental side J/ψ production is much easier than Υ . Nevertheless, with a new generation high luminosity electron ion collider (EIC) [54, 86] one should be able to also obtain sufficiently accurate data for the latter process.

Two spin asymmetries were investigated with an eye towards gaining information about the GPD E^g . Since this GPD is related to the spin-flip amplitude and only enters the non-flip amplitude proportional to $\xi^2/(1 - \xi^2)$, the unpolarized cross section is a poor probe of it. The transverse SSA A_N , however, is generally considered useful in obtaining knowledge on this distribution. When investigated, though, we find that the asymmetry tends to be very small, except for a very "peculiar" variant for E^g which is not favored by present data on ρ and ϕ production as discussed above. Also, there is generally not much change observed when changing the variant, so measurements of this observable would hardly constrain E^g . Our newly defined DSA A_{LS} is a much better prospect in this situation, since the magnitudes tend to be larger and the variants show a greater spread. Potential measurements would then yield useful constraints on E^g . Unfortunately, this is experimentally challenging, since A_{LS} requires measurement of the polarization of the recoil

nucleon. In any case, the most likely case for testing these predictions is at the EIC [54,86].

We also investigated SDMEs for an unpolarized target, which in general describe the angular distribution of the process. For our LO calculation in the non-relativistic approximation, we find only a very few SDMEs that are nonzero, and even fewer which are independent. There is experimental data for exclusive J/ψ production, which in general agrees with our numerical results, though the experimental error bars are large. These SDMEs in our approach have a very simple dependence on the kinematics, and in particular do not depend on the GPDs at all. The NLO results for photoproduction in Ref. [32] do not modify those simple expressions. However, one has to keep in mind that right now it is not clear if this is a general result, since in [32] only the contribution of H^g and E^g was explored, while generally other gluon GPDs may enter at NLO, which then could spoil the simple results obtained for the SDMEs. Also, going beyond the non-relativistic approximation would lead to more complicated expressions. On the other hand, existing phenomenology does not allow ruling out any of the used approximations.

There are several open points for future investigations:

- As discussed, overall our numerical results do not agree very well with existing data. However, one has to keep in mind that those data were not included in a fit, but we rather took in particular the GPD H^g extracted from data on light vector meson production as given in Refs. [40–42]. The theoretical framework used in those papers is different from the one used here. The authors exploit the so-called modified hard scattering approach in which one partly keeps transverse parton momenta. It would be worthwhile to aim at a global analysis of data for light and heavy vector mesons using collinear factorization at NLO accuracy throughout the calculation. In this context one has to keep in mind that occasionally a perturbation series becomes more stable once going beyond NLO even though for quarkonium production at present we have no evidence for such a behavior.
- Because of the importance of the topic at hand it would be mandatory to perform a totally independent calculation of the NLO corrections for photoproduction in order

to check the result obtained in [32]. In fact, very recently it was pointed out that there is actually an error in the NLO expression of that paper [87]. This applies only to the quark NLO amplitude, and based on preliminary calculations we have found that while it does lead to a non-negligible change in the numerics, the general results are not changed — the J/ψ results are still not well under control, while the Υ results are better behaved. When doing a new NLO calculation one can also address the aforementioned question of whether at NLO any gluon GPD beyond H^g and E^g enters.

- Future work should also look at electroproduction of quarkonia at NLO. The behavior that we see when going from LO to NLO in J/ψ production is expected to change in this case, with the NLO results becoming more stable as we increase the photon virtuality. In general, the higher Q^2 the better the convergence of the perturbation series. Of course, for increasing Q^2 the count rate decreases, and in practice one will have to try to find an optimal value for the photon virtuality.
- Large logarithms of the type $\ln 1/\xi$ are most likely a major cause of the large higher order corrections [32]. If those logarithms can be re-summed to arbitrary order in perturbation theory, as has been done in several other related situations, one can expect the framework to become much more robust.
- It would be very interesting to go beyond the non-relativistic approximation for the quarkonia. While for the Υ this approximation should be very accurate, in the case of J/ψ the situation is less clear. Such a study would be particularly interesting if indeed at NLO no GPD other than H^g and E^g enters in the non-relativistic approximation. It has been pointed out that this simple situation changes once relativistic corrections are included [88], and we have been able to confirm this finding. This would then imply further nonzero observables which depend on additional GPDs.

BIBLIOGRAPHY

- [1] J. Thomson, *Phil. Mag.* **44**, 293 (1897).
- [2] E. Rutherford, *Phil. Mag.* **21**, 669 (1911).
- [3] W. Heisenberg, *Z. Phys.* **77**, 1 (1932).
- [4] Y. Ne'eman, *Nucl. Phys.* **26**, 222 (1961).
- [5] M. Gell-Mann, *Phys. Lett.* **8**, 214 (1964).
- [6] G. Zweig, CERN-TH-401 (1964).
- [7] G. Zweig, CERN-TH-412 (1964).
- [8] O. Greenberg, *Phys. Rev. Lett.* **13**, 598 (1964).
- [9] M. Han and Y. Nambu, *Phys. Rev.* **139**, B1006 (1965).
- [10] E. D. Bloom *et al.*, *Phys. Rev. Lett.* **23**, 930 (1969).
- [11] M. Breidenbach *et al.*, *Phys. Rev. Lett.* **23**, 935 (1969).
- [12] H. Fritzsch and M. Gell-Mann, eConf **C720906V2**, 135 (1972), hep-ph/0208010.
- [13] H. Fritzsch, M. Gell-Mann, and H. Leutwyler, *Phys. Lett.* **B47**, 365 (1973).
- [14] D. J. Gross and F. Wilczek, *Phys. Rev. Lett.* **30**, 1343 (1973).
- [15] H. D. Politzer, *Phys. Rev. Lett.* **30**, 1346 (1973).
- [16] D. Gross and F. Wilczek, *Phys. Rev.* **D8**, 3633 (1973).
- [17] H. D. Politzer, *Phys. Rept.* **14**, 129 (1974).
- [18] J. C. Collins, D. E. Soper, and G. F. Sterman, *Phys. Lett.* **B109**, 388 (1982).
- [19] D. Müller, D. Robaschik, B. Geyer, F.-M. Dittes, and J. Hořejši, *Fortsch. Phys.* **42**, 101 (1994), hep-ph/9812448.
- [20] X.-D. Ji, *Phys. Rev. Lett.* **78**, 610 (1997), hep-ph/9603249.
- [21] A. Radyushkin, *Phys. Lett.* **B380**, 417 (1996), hep-ph/9604317.
- [22] A. Radyushkin, *Phys. Lett.* **B385**, 333 (1996), hep-ph/9605431.

- [23] X.-D. Ji, Phys. Rev. **D55**, 7114 (1997), hep-ph/9609381.
- [24] K. Goeke, M. V. Polyakov, and M. Vanderhaeghen, Prog. Part. Nucl. Phys. **47**, 401 (2001), hep-ph/0106012.
- [25] M. Diehl, Phys. Rept. **388**, 41 (2003), hep-ph/0307382.
- [26] M. Burkardt, Phys. Rev. **D62**, 071503 (2000), hep-ph/0005108.
- [27] A. Vinnikov, hep-ph/0604248.
- [28] J. Koempel, P. Kroll, A. Metz, and J. Zhou, Phys. Rev. **D85**, 051502 (2012), arxiv:1112.1334 [hep-ph].
- [29] M. Ryskin, Z. Phys. **C57**, 89 (1993).
- [30] S. J. Brodsky, L. Frankfurt, J. Gunion, A. H. Mueller, and M. Strikman, Phys. Rev. **D50**, 3134 (1994), hep-ph/9402283.
- [31] L. Mankiewicz, G. Piller, and T. Weigl, Eur. Phys. J. **C5**, 119 (1998), hep-ph/9711227.
- [32] D. Y. Ivanov, A. Schafer, L. Szymanowski, and G. Krasnikov, Eur. Phys. J. **C34**, 297 (2004), hep-ph/0401131.
- [33] X.-D. Ji, J. Phys. **G24**, 1181 (1998), hep-ph/9807358.
- [34] P. Kroll, Nuovo Cim. **C036**, 167 (2013), arxiv:1303.6433 [hep-ph].
- [35] I. Balitsky and X.-D. Ji, Phys. Rev. Lett. **79**, 1225 (1997), hep-ph/9702277.
- [36] V. Barone, T. Calarco, and A. Drago, Phys. Lett. **B431**, 405 (1998), hep-ph/9801281.
- [37] S. Goloskokov and P. Kroll, Eur. Phys. J. **C59**, 809 (2009), arxiv:0809.4126 [hep-ph].
- [38] European Muon Collaboration, J. Ashman *et al.*, Phys. Lett. **B206**, 364 (1988).
- [39] M. Burkardt, Int. J. Mod. Phys. **A18**, 173 (2003), hep-ph/0207047.
- [40] S. Goloskokov and P. Kroll, Eur. Phys. J. **C42**, 281 (2005), hep-ph/0501242.
- [41] S. Goloskokov and P. Kroll, Eur. Phys. J. **C50**, 829 (2007), hep-ph/0611290.
- [42] S. Goloskokov and P. Kroll, Eur. Phys. J. **C53**, 367 (2008), arxiv:0708.3569 [hep-ph].
- [43] J. Blumlein, B. Geyer, and D. Robaschik, Phys. Lett. **B406**, 161 (1997), hep-ph/9705264.
- [44] V. Gribov and L. Lipatov, Sov. J. Nucl. Phys. **15**, 438 (1972).
- [45] L. Lipatov, Sov. J. Nucl. Phys. **20**, 94 (1975).
- [46] Y. L. Dokshitzer, Sov. Phys. JETP **46**, 641 (1977).
- [47] G. Altarelli and G. Parisi, Nucl. Phys. **B126**, 298 (1977).
- [48] G. P. Lepage and S. J. Brodsky, Phys. Lett. **B87**, 359 (1979).

- [49] A. Efremov and A. Radyushkin, Phys. Lett. **B94**, 245 (1980).
- [50] I. Musatov and A. Radyushkin, Phys. Rev. **D61**, 074027 (2000), hep-ph/9905376.
- [51] A. Radyushkin, Phys. Lett. **B449**, 81 (1999), hep-ph/9810466.
- [52] M. Diehl, T. Feldmann, R. Jakob, and P. Kroll, Eur. Phys. J. **C39**, 1 (2005), hep-ph/0408173.
- [53] M. Diehl and P. Kroll, Eur. Phys. J. **C73**, 2397 (2013), arxiv:1302.4604 [hep-ph].
- [54] D. Boer *et al.*, (2011), arxiv:1108.1713 [nucl-th].
- [55] M. Diehl and W. Kugler, Eur. Phys. J. **C52**, 933 (2007), arxiv:0708.1121 [hep-ph].
- [56] J. C. Collins, L. Frankfurt, and M. Strikman, Phys. Rev. **D56**, 2982 (1997), hep-ph/9611433.
- [57] J. Vermaseren, math-ph/0010025.
- [58] M. Diehl, Eur. Phys. J. **C19**, 485 (2001), hep-ph/0101335.
- [59] M. Ryskin, Phys. Lett. **B403**, 335 (1997).
- [60] M. Vanttinen and L. Mankiewicz, Phys. Lett. **B434**, 141 (1998), hep-ph/9805338.
- [61] M. Vanderhaeghen, P. A. Guichon, and M. Guidal, Phys. Rev. Lett. **80**, 5064 (1998).
- [62] K. Schilling and G. Wolf, Nucl. Phys. **B61**, 381 (1973).
- [63] M. Diehl, JHEP **0709**, 064 (2007), arxiv:0704.1565 [hep-ph].
- [64] Wolfram Research, Inc., Mathematica, Version 8.0, (2010).
- [65] A. Freund, M. McDermott, and M. Strikman, Phys. Rev. **D67**, 036001 (2003), hep-ph/0208160.
- [66] S. D. Holmes, W.-Y. Lee, and J. Wiss, Ann. Rev. Nucl. Part. Sci. **35**, 397 (1985).
- [67] H1 Collaboration, A. Aktas *et al.*, Eur. Phys. J. **C46**, 585 (2006), hep-ex/0510016.
- [68] ZEUS Collaboration, S. Chekanov *et al.*, Nucl. Phys. **B695**, 3 (2004), hep-ex/0404008.
- [69] H1 Collaboration, C. Alexa *et al.*, Eur. Phys. J. **C73**, 2466 (2013), arxiv:1304.5162 [hep-ex].
- [70] B. Gittelmann *et al.*, Phys. Rev. Lett. **35**, 1616 (1975).
- [71] T. Nash *et al.*, Phys. Rev. Lett. **36**, 1233 (1976).
- [72] B. H. Denby *et al.*, Phys.Rev.Lett. **52**, 795 (1984).
- [73] ZEUS Collaboration, M. Derrick *et al.*, Phys. Lett. **B350**, 120 (1995), hep-ex/9503015.
- [74] H1 Collaboration, S. Aid *et al.*, Nucl.Phys. **B472**, 3 (1996), hep-ex/9603005.

- [75] ZEUS Collaboration, J. Breitweg *et al.*, *Z. Phys.* **C75**, 215 (1997), hep-ex/9704013.
- [76] H1 Collaboration, C. Adloff *et al.*, *Phys. Lett.* **B483**, 23 (2000), hep-ex/0003020.
- [77] H1 Collaboration, C. Adloff *et al.*, *Eur. Phys. J.* **C10**, 373 (1999), hep-ex/9903008.
- [78] ZEUS Collaboration, J. Breitweg *et al.*, *Phys. Lett.* **B437**, 432 (1998), hep-ex/9807020.
- [79] ZEUS Collaboration, S. Chekanov *et al.*, *Phys. Lett.* **B680**, 4 (2009), arxiv:0903.4205 [hep-ex].
- [80] ZEUS Collaboration, J. Breitweg *et al.*, *Eur. Phys. J.* **C6**, 603 (1999), hep-ex/9808020.
- [81] ZEUS Collaboration, S. Chekanov *et al.*, *Eur. Phys. J.* **C24**, 345 (2002), hep-ex/0201043.
- [82] W. Augustyniak, A. Borissov, and S. Manayenkov, arxiv:0808.0669 [hep-ex].
- [83] W. Augustyniak, PoS **DIS2010**, 283 (2010).
- [84] HERMES Collaboration, A. Rostomyan and J. Dreschler, arxiv:0707.2486 [hep-ex].
- [85] HERMES Collaboration, A. Airapetian *et al.*, *Phys. Lett.* **B679**, 100 (2009), arxiv:0906.5160 [hep-ex].
- [86] A. Accardi *et al.*, arxiv:1212.1701 [nucl-ex].
- [87] D. Y. Ivanov, B. Pire, L. Szymanowski, and J. Wagner, arxiv:1411.3750 [hep-ph].
- [88] M. Vanttinen and L. Mankiewicz, *Phys. Lett.* **B440**, 157 (1998), hep-ph/9807287.
- [89] M. Galassi *et al.*, *GNU Scientific Library Reference Manual*, Third ed. (Network Theory Ltd., 2009).

APPENDIX A

MODELING H

The same basic method is used to model both E and H , therefore, the double distribution approach outlined in Chapter 2 is used for both. As a reminder, we have

$$F^i(x, \xi, t) = \int_{-1}^1 d\beta \int_{-1+|\beta|}^{1-|\beta|} d\alpha \delta(\beta + \xi\alpha - x) f^i(\beta, \alpha, t) \quad (\text{A.1})$$

$$f^i(\beta, \alpha, t) = F^i(|\beta|, 0, 0) e^{bt} |\beta|^{-\alpha' t} \frac{\Gamma(2n_i + 2)}{2^{2n_i+1} \Gamma^2(n_i + 1)} \frac{[(1 - |\beta|)^2 - \alpha^2]^{n_i}}{(1 - |\beta|)^{2n_i+1}}. \quad (\text{A.2})$$

Where we use [41,51]

$$\begin{aligned} H_{val}^q(|\beta|, 0, 0) &= q^{val}(\beta) \quad n_{val} = 1 \\ H_{sea}^q(|\beta|, 0, 0) &= q^{sea}(\beta) \quad n_{sea} = 2 \\ H^g(|\beta|, 0, 0) &= |\beta| g(\beta) \quad n_g = 2. \end{aligned} \quad (\text{A.3})$$

We follow [37,41,42] in our choice of b and α' , where we have for gluons and sea quarks:

$$b = 2.58 \text{ GeV}^{-2} + 0.25 \text{ GeV}^{-2} \ln \frac{m_n^2}{\mu_0^2 + m_n^2} \quad (\text{A.4})$$

and $\alpha' = 0.15$. For the valence quarks, we use $b = 0$ and $\alpha' = 0.9$. We use the previously determined parameterizations [42] (based on the CTEQ6M PDFs) for the forward distribution of H ($\beta > 0$):

$$H^i(\beta, 0, 0) = -\beta^{-\delta_i} (1 - \beta)^{2n_i+1} \sum_{j=0}^3 c_{ij} \beta^{j/2} \quad (\text{A.5})$$

	gluon	strange	u_{val}	d_{val}
δ	.1	1.1	0.48	0.48
c_0	2.23	0.123	1.52	0.76
c_1	5.43	-3.27	2.88	3.11
c_2	-34.0	0.692	-0.095	-3.99
c_3	40.6	-0.486	0	0

Table A.1: Parameters of q_{val}^a , q^s , and g at the scale $\mu = 2$ GeV. Note that δ^s is defined as $1 + \delta^g$.

where the values of δ and the c_{ij} are given in Table A.1. Based on previous work, we use a simple method to break the flavor symmetry of the sea for H [41]

$$H^{\bar{u}} = H^{\bar{d}} = \kappa_s H^{\bar{s}} = \kappa_s H^s, \quad (\text{A.6})$$

where $\kappa_s = 1.68$. In this way, we have a full model for calculating H for gluons, along with the valence and sea quark distributions which are needed for evolution.

APPENDIX B

SPINOR ALGEBRA

As stated in Section 2.1, GPDs are defined as matrix elements of quark and gluon operators. The relevant definitions for our purposes are those containing the quark and gluon GPDs H and E ,

$$\begin{aligned}
 F^q &= \frac{1}{2} \int \frac{dz^-}{2\pi} e^{ixP^+z^-} \left\langle p' \left| \bar{q} \left(-\frac{1}{2}z \right) \gamma^+ q \left(\frac{1}{2}z \right) \right| p \right\rangle \Big|_{z^+=0, \mathbf{z}=0} \\
 &= \frac{1}{2P^+} \left[H^q(x, \xi, t) \bar{u}(p') \gamma^+ u(p) + E^q(x, \xi, t) \bar{u}(p') \frac{i\sigma^{+\alpha} \Delta_\alpha}{2m} u(p) \right] \quad (\text{B.1})
 \end{aligned}$$

$$\begin{aligned}
 F^g &= \frac{1}{P^+} \int \frac{dz^-}{2\pi} e^{ixP^+z^-} \left\langle p' \left| G^{+\mu} \left(-\frac{1}{2}z \right) G_{\mu}^+ \left(\frac{1}{2}z \right) \right| p \right\rangle \Big|_{z^+=0, \mathbf{z}=0} \\
 &= \frac{1}{2P^+} \left[H^g(x, \xi, t) \bar{u}(p') \gamma^+ u(p) + E^g(x, \xi, t) \bar{u}(p') \frac{i\sigma^{+\alpha} \Delta_\alpha}{2m} u(p) \right]. \quad (\text{B.2})
 \end{aligned}$$

In order to make the definitions more convenient, we must perform some spinor algebra to simplify terms containing the helicity spinors $u(p)$ and $\bar{u}(p')$. We note that the spinor products are the same for both the quarks and gluons, so going through the procedure for one case is sufficient to solve it for both.

First, we need to specify a few kinematics. We work with a nucleon which has a large plus momentum, and consider the transverse momentum to be negligible. Next we define the spinor, utilizing light cone momenta as defined in Eq. (2.2) and, without loss of

generality, assume that the nucleon has a positive helicity:

$$u(p) = \frac{1}{\sqrt{2}\sqrt{2p^+}} \begin{pmatrix} \sqrt{2}p^+ + m \\ p^1 + ip^2 \\ \sqrt{2}p^+ - m \\ p^1 + ip^2 \end{pmatrix}. \quad (\text{B.3})$$

We can then evaluate the first product, which appears along with H , where I is the 2×2 unit matrix and σ^3 is a 2×2 Pauli matrix,

$$\begin{aligned} \bar{u}(p')\gamma^+u(p) &= \bar{u}(p')\frac{1}{\sqrt{2}}(\gamma^0 + \gamma^3)u(p) = \frac{1}{\sqrt{2}}\bar{u}(p') \begin{pmatrix} I & \sigma^3 \\ -\sigma^3 & -I \end{pmatrix} u(p) \\ &= \frac{1}{4\sqrt{p^+p'^+}} (\sqrt{2}p'^+ + m, 0, -\sqrt{2}p'^+ + m, 0) \begin{pmatrix} I & \sigma^3 \\ -\sigma^3 & -I \end{pmatrix} \begin{pmatrix} \sqrt{2}p^+ + m \\ 0 \\ \sqrt{2}p^+ - m \\ 0 \end{pmatrix} \\ &= \frac{1}{4\sqrt{p^+p'^+}} (\sqrt{2}p'^+ + m, 0, -\sqrt{2}p'^+ + m, 0) \begin{pmatrix} 2\sqrt{2}p^+ \\ 0 \\ -2\sqrt{2}p^+ \\ 0 \end{pmatrix} \\ &= \frac{1}{4\sqrt{p^+p'^+}} [4p'^+p^+ + 2\sqrt{2}mp^+ + 4p'^+p^+ - 2\sqrt{2}mp^+] = 2\sqrt{p'^+p^+} \\ &= 2P^+ \sqrt{1 - \xi^2} \end{aligned} \quad (\text{B.4})$$

Where the last step exploited the ξ symmetry of the nucleon momenta, i.e. $p^+ = (1 + \xi)P^+$ and $p'^+ = (1 - \xi)P^+$.

Evaluating the other product more of the same, noting that $\sigma^{\mu\nu} = \frac{i}{2} [\gamma^\mu, \gamma^\nu]$

$$\begin{aligned} \bar{u}(p') \frac{i\sigma^{+\alpha} \Delta_\alpha}{2m} u(p) &= \bar{u}(p') \frac{i\Delta_+ \frac{i}{2} (\gamma^+ \gamma^- - \gamma^- \gamma^+)}{2m} u(p) = \bar{u}(p') \frac{\Delta_+}{2m} \begin{pmatrix} 0 & \sigma^3 \\ \sigma^3 & 0 \end{pmatrix} u(p) \\ &= \frac{\Delta_+(p^+ - p'^+)}{2\sqrt{p^+ p'^+}} = -2P^+ \sqrt{1 - \xi^2} \frac{\xi^2}{1 - \xi^2}. \end{aligned} \quad (\text{B.5})$$

Where in the first step we used the fact that $\sigma^{++} \propto [\gamma^+, \gamma^+] = 0$, which leaves only the term containing Δ_+ .

Inserting results (B.4) and (B.5) into (B.1) and (B.2), we are left with

$$\begin{aligned} F^q &= \frac{1}{2} \int \frac{dz^-}{2\pi} e^{ixP^+ z^-} \left\langle p' \left| \bar{q} \left(-\frac{1}{2}z \right) \gamma^+ q \left(\frac{1}{2}z \right) \right| p \right\rangle \Big|_{z^+=0, \mathbf{z}=0} \\ &= \sqrt{1 - \xi^2} \left[H^q(x, \xi, t) - \frac{\xi^2}{1 - \xi^2} E^q(x, \xi, t) \right] \end{aligned} \quad (\text{B.6})$$

$$\begin{aligned} F^g &= \frac{1}{P^+} \int \frac{dz^-}{2\pi} e^{ixP^+ z^-} \left\langle p' \left| G^{+\mu} \left(-\frac{1}{2}z \right) G_{\mu^+} \left(\frac{1}{2}z \right) \right| p \right\rangle \Big|_{z^+=0, \mathbf{z}=0} \\ &= \sqrt{1 - \xi^2} \left[H^g(x, \xi, t) - \frac{\xi^2}{1 - \xi^2} E^g(x, \xi, t) \right]. \end{aligned} \quad (\text{B.7})$$

APPENDIX C

NEXT TO LEADING ORDER

The next to leading order (NLO) corrections are nontrivial to calculate numerically. In addition to the overall length of the expressions, there are also several complications which arise simply from wanting to do things numerically. This appendix is meant as a guide to the method used to obtain NLO results.

C.1 Gluon Amplitude

As discussed in Chapter 5, when evaluating the NLO amplitude, Eq. (3.32), we require the product of the GPDs and f_g , Eq. (3.37), to be integrated over x . The resulting expression is not well behaved numerically, and requires some special handling in the unstable regions. Another major complication is that the evolution code used presents the GPD results as a pre-calculated array of values; however, many advanced integration routines require the integrand to be a function, so that it can dynamically choose at which points it performs evaluations. See, for example, the numerical integration routines contained in the GNU Scientific Library (GSL) [89], which is a free numerical library for C and C++ programmers. Because of this, and the fact that the points at which the GPDs are evaluated are unevenly spaced in x , a method had to be developed that could handle the constraints.

Making the code easy to debug and alter is important, so in order to facilitate readability and modularity, f_g , Eq. (3.37), was implemented on a term by term basis, i.e. each term is computed separately, and then the results are all added together before being passed to

the integration routine. Additionally, since singularities appear proportional to different powers of $1/y$, the terms were also separated according to these divergences. A decomposition of the complex expressions into real and imaginary components was also performed. The point of $y = -1/2$ was handled slightly differently since there are individual terms which diverge at this point, but analytically these divergences cancel. The integrand was analytically evaluated at this point and the resulting expression was then hardcoded in.

Note that in the following discussion, the factor of $1/y$ present in T_g , Eq. (3.35), is included. Also, in order to refer to the different terms, the notation $f_{g,n}$ is used to refer to the n^{th} term of f_g . Additionally, care must be used in evaluating the expressions to make sure that one is on the correct branch, e.g. $\ln(-(y + i\epsilon)) = \ln(-x + \xi - i\epsilon) = \ln|y| - i\pi$.

As a reminder, in order to avoid numerical issues in integrating over the interval $0 \leq x \leq 1$, we split the integral into three parts,

$$\int_0^1 \phi(x) dx = \int_0^{\xi-\delta_1} \phi(x) dx + \int_{\xi-\delta_1}^{\xi-\delta_2} \phi(x) dx + \int_{\xi-\delta_2}^1 \phi(x) dx. \quad (\text{C.1})$$

We numerically integrate the first and third regions, effectively performing a principal value integration, and perform the middle integration analytically. Since the inner region is a small interval around $x = \xi$, we first expand the integrand around this point to make the analytic integration feasible.

We note that only a dozen different integrals need to be evaluated in order to obtain all the necessary expressions. Since we write the expressions in terms of y , we also need to change the limits of integration, $-\delta_1/(2\xi)$ and $\delta_2/(2\xi)$ for the lower and upper limits, respectively:

$$\int \frac{\ln[-y]}{y^2} dy = -\frac{(2\xi)^2 \left(\delta_1 + \delta_2 + \delta_2 \ln \left[\frac{\delta_1}{2\xi} \right] + \delta_1 \ln \left[\frac{\delta_2}{2\xi} \right] \right)}{\delta_1 \delta_2} + i \frac{(2\xi)^2 \pi}{\delta_2} \quad (\text{C.2})$$

$$\int \frac{1}{y^2} dy = -\frac{(2\xi)^2 (\delta_1 + \delta_2)}{\delta_1 \delta_2} \quad (\text{C.3})$$

$$\int \frac{\sqrt{-y}}{y^2} dy = i2\xi \frac{2\sqrt{2\xi} (\sqrt{\delta_1} + i\sqrt{\delta_2})}{\sqrt{\delta_1 \delta_2}} \quad (\text{C.4})$$

$$\int \frac{\ln[-y]^2}{y} dy = 2\xi \left\{ -\pi^2 \ln \left[\frac{\delta_2}{2\xi} \right] + \frac{1}{3} \left(\ln^3 \left[\frac{\delta_2}{2\xi} \right] - \ln^3 \left[\frac{\delta_1}{2\xi} \right] \right) \right\} + i2\xi \left(\frac{\pi^3}{3} - \pi \ln^2 \left[\frac{\delta_2}{2\xi} \right] \right) \quad (\text{C.5})$$

$$\int \frac{\ln[-y]}{y} dy = \xi \left(-\pi^2 + \ln \left[\frac{\delta_2}{\delta_1} \right] \ln \left[\frac{\delta_2 \delta_1}{4\xi^2} \right] \right) - i2\pi\xi \ln \left[\frac{\delta_2}{2\xi} \right] \quad (\text{C.6})$$

$$\int \frac{\ln[-2y]}{y} dy = \xi \left(-\pi^2 + \ln \left[\frac{\delta_2}{\delta_1} \right] \ln \left[\frac{\delta_2 \delta_1}{\xi^2} \right] \right) - i2\pi\xi \ln \left[\frac{\delta_2}{\xi} \right] \quad (\text{C.7})$$

$$\int \frac{1}{y} dy = 2\xi \left(\ln \left[\frac{\delta_2}{\delta_1} \right] - i\pi \right) \quad (\text{C.8})$$

$$\int \frac{\sqrt{-y}}{y} dy = -2\sqrt{2\xi} \left(\sqrt{\delta_1} + i\sqrt{\delta_2} \right) \quad (\text{C.9})$$

$$\int \ln[-y]^2 dy = 2(\delta_1 + \delta_2) - \pi^2 \delta_2 - \delta_1 \ln \left[\frac{\delta_1}{2\xi} \right] \left(2 - \ln \left[\frac{\delta_1}{2\xi} \right] \right) - \delta_2 \ln \left[\frac{\delta_2}{2\xi} \right] \left(2 - \ln \left[\frac{\delta_2}{2\xi} \right] \right) + i2\pi\delta_2 \left(1 - \ln \left[\frac{\delta_2}{2\xi} \right] \right) \quad (\text{C.10})$$

$$\int \ln[-y] dy = - \left(\delta_1 + \delta_2 - \delta_1 \ln \left[\frac{\delta_1}{2\xi} \right] - \delta_2 \ln \left[\frac{\delta_2}{2\xi} \right] \right) - i\pi\delta_2 \quad (\text{C.11})$$

$$\int \ln[-2y] dy = - \left(\delta_1 + \delta_2 - \delta_1 \ln \left[\frac{\delta_1}{\xi} \right] - \delta_2 \ln \left[\frac{\delta_2}{\xi} \right] \right) - i\pi\delta_2 \quad (\text{C.12})$$

$$\int 1 dy = \delta_1 + \delta_2 \quad (\text{C.13})$$

In the expressions which follow, we will simply refer to these integrals, instead of reproducing them where they are needed. This is the same approach which is taken in the code, so that they need to be computed only once. In the code, we make use of the complex arithmetic library. We write each integral as a complex value, and utilize those expressions in the terms of f_g . Once we add everything together, we then separate the real and imaginary components.

In addition to integrating the terms which compose f_g , Eq. (3.37), we also need to include the factor included in T_g (3.35) and the GPD itself. Since we already include the extra factor of $1/y$ in the following, the only remaining x dependence that must be taken into account is $F^g(x)/(x+\xi)$; this too, we expand (leaving things in terms of y for convenience),

$$\frac{F^g(x)}{x+\xi} = \frac{F^g(\xi(1+2y))}{2\xi(1+y)} \approx \frac{1}{2\xi} [F^g(\xi) - y \{F^g(\xi) - 2\xi F^{g'}(\xi)\}] \quad (\text{C.14})$$

Now that we have everything in place, we can look at the individual terms. As is hinted at in the integrals above, when expanding the integrands, we keep terms which, in powers of δ , are at most $\propto \delta$. Terms proportional to greater powers of δ are sufficiently small to warrant this cutoff.

$f_{g,1}$

We start off with

$$\frac{f_{g,1}}{y} = 4(c_1 - c_2)(1 + 2y(1 + y)) \left(\frac{\ln(-y)}{y(1 + y)} - \frac{\ln(1 + y)}{y^2} \right) \left(\ln \frac{4m^2}{\mu_F^2} - 1 \right), \quad (\text{C.15})$$

which, when we expand around $y = 0$, yields

$$\frac{f_{g,1}}{y} \approx 4(c_1 - c_2) \left(\ln \frac{4m^2}{\mu_F^2} - 1 \right) \left[\frac{\ln(-y)}{y} - \frac{1}{y} + \ln(-y) - \frac{3}{2} \right]. \quad (\text{C.16})$$

Including the expansion of the GPD and the remaining factor of $1/(x + \xi)$ (C.14), we have

$$\begin{aligned} \int dy \frac{f_{g,1}}{y} \frac{F^g(\xi(1 + 2y))}{2\xi(1 + y)} &\approx \frac{2(c_1 - c_2) \left(\ln \frac{4m^2}{\mu_F^2} - 1 \right)}{\xi} \\ &\times \int \left\{ F^g(\xi) \left[\frac{\ln(-y)}{y} - \frac{1}{y} + \ln(-y) - \frac{3}{2} \right] \right. \\ &\quad \left. - [F^g(\xi) - 2\xi F^{g'}(\xi)] [\ln(-y) - 1] \right\} dy. \end{aligned} \quad (\text{C.17})$$

We can simplify this expression somewhat, leading to our final result (for this term) of

$$\begin{aligned} \int dy \frac{f_{g,1}}{y} \frac{F^g(\xi(1 + 2y))}{2\xi(1 + y)} &\approx \frac{2(c_1 - c_2) \left(\ln \frac{4m^2}{\mu_F^2} - 1 \right)}{\xi} \\ &\times \int \left\{ F^g(\xi) \left[\frac{\ln(-y)}{y} - \frac{1}{y} - \frac{1}{2} \right] + 2\xi F^{g'}(\xi) [\ln(-y) - 1] \right\} dy. \end{aligned} \quad (\text{C.18})$$

The procedure performed here is duplicated for each term in f_g , so from here on we will simply state the term and the final result, unless additional commentary is necessary.

$f_{g,2}$

$$\frac{f_{g,2}}{y} = \frac{\beta_0}{y} \ln \frac{\mu_R^2}{\mu_F^2}. \quad (\text{C.19})$$

$$\int dy \frac{f_{g,2}}{y} \frac{F^g(\xi(1+2y))}{2\xi(1+y)} \approx \frac{\beta_0}{2\xi} \ln \frac{\mu_R^2}{\mu_F^2} \int \left\{ F^g(\xi) \frac{1}{y} - [F^g(\xi) - 2\xi F^{g'}(\xi)] \right\} dy \quad (\text{C.20})$$

 $f_{g,3}$

$$\frac{f_{g,3}}{y} = 4(c_1 - c_2)(1 + 2y(1 + y)) \left(\frac{\ln^2(-y)}{y(1+y)} - \frac{\ln^2(1+y)}{y^2} \right). \quad (\text{C.21})$$

$$\int dy \frac{f_{g,3}}{y} \frac{F^g(\xi(1+2y))}{2\xi(1+y)} \approx \frac{2(c_1 - c_2)}{\xi} \int \left\{ F^g(\xi) \left[\frac{\ln^2(-y)}{y} - 1 \right] + 2\xi F^{g'}(\xi) \ln^2(-y) \right\} dy \quad (\text{C.22})$$

 $f_{g,4}$

$$\frac{f_{g,4}}{y} = -\frac{8c_1}{y}. \quad (\text{C.23})$$

$$\int dy \frac{f_{g,4}}{y} \frac{F^g(\xi(1+2y))}{2\xi(1+y)} \approx -\frac{4c_1}{\xi} \int \left\{ F^g(\xi) \frac{1}{y} - [F^g(\xi) - 2\xi F^{g'}(\xi)] \right\} dy \quad (\text{C.24})$$

 $f_{g,5}$

This term has an added complication that has not appeared yet, we start off with

$$\frac{f_{g,5}}{y} = -\pi^2 \left(\frac{2 + y(1+y)(25 + 88y(1+y))}{48y^3(1+y)^2} c_1 + \frac{10 + y(1+y)(7 - 52y(1+y))}{24y^3(1+y)^2} c_2 \right). \quad (\text{C.25})$$

Factoring this expression leaves us with

$$\begin{aligned} \frac{f_{g,5}}{y} = -\pi^2 & \left[\left(\frac{1}{24y^3(1+y)^2} + \frac{25}{48y^2(1+y)} + \frac{11}{6y} \right) c_1 \right. \\ & \left. + \left(\frac{5}{12y^3(1+y)^2} + \frac{7}{24y^2(1+y)} - \frac{13}{6y} \right) c_2 \right]. \end{aligned} \quad (\text{C.26})$$

We see that this is the first expression which contains terms proportional to $\frac{1}{y^3}$; since we expect a cancellation of these terms, starting now we will leave out any term with a y^3 in the denominator and combine them at the end. Doing so, and expanding what is left yields

$$-\pi^2 \left\{ \left[\left(\frac{1}{y^2} - \frac{1}{y} + 1 \right) + \frac{11}{6} \frac{1}{y} \right] c_1 + \left[\frac{7}{24} \left(\frac{1}{y^2} - \frac{1}{y} + 1 \right) - \frac{13}{6} \frac{1}{y} \right] c_2 \right\} \quad (\text{C.27})$$

Finally, including (C.14) and separating according to powers of y leaves us with the integral

$$\begin{aligned} \int dy \frac{f_{g,5}}{y} \frac{F^g(\xi(1+2y))}{2\xi(1+y)} \approx -\frac{\pi^2}{2\xi} \int \left\{ F^g(\xi) \left[\frac{1}{y^2} \left(\frac{25c_1}{48} + \frac{7c_2}{24} \right) \right. \right. \\ \left. \left. + \frac{1}{y} \left(\frac{19c_1}{24} - \frac{11c_2}{4} \right) + \frac{19c_1}{24} + \frac{11c_2}{4} \right] \right. \\ \left. + \xi F^{g'}(\xi) \left[\frac{1}{y} \left(\frac{25c_1}{24} + \frac{7c_2}{12} \right) + \frac{21c_1}{8} - \frac{59c_2}{12} \right] \right\} dy \end{aligned} \quad (\text{C.28})$$

$f_{g,6}$

$$\frac{f_{g,6}}{y} = -\ln(2) \left[c_1 \frac{1+6y(1+y)(1+2y(1+y))}{y^2(1+y)(1+2y)^2} + c_2 \frac{(1+2y)^2}{y^2(1+y)} \right]. \quad (\text{C.29})$$

$$\begin{aligned} \int dy \frac{f_{g,6}}{y} \frac{F^g(\xi(1+2y))}{2\xi(1+y)} \approx -\frac{\ln(2)}{2\xi} \int \left\{ F^g(\xi) \left[\frac{c_1+c_2}{y^2} + \frac{2c_2}{y} + 4c_1 - 2c_2 \right] \right. \\ \left. + 2\xi F^{g'}(\xi) \left[\frac{c_1+c_2}{y} + c_1 + 3c_2 \right] \right\} dy \end{aligned} \quad (\text{C.30})$$

$f_{g,7}$

$$\frac{f_{g,7}}{y} = \pi \frac{\sqrt{-y(1+y)}}{y^2(1+y)} \left(\frac{7}{2}c_1 - 3c_2 \right) \quad (\text{C.31})$$

$$\int dy \frac{f_{g,7}}{y} \frac{F^g(\xi(1+2y))}{2\xi(1+y)} \approx \frac{\pi(7c_1 - 6c_2)}{4\xi} \int \left\{ F^g(\xi) \left[\frac{\sqrt{-y}}{y^2} - \frac{3\sqrt{-y}}{2y} \right] + 2\xi F^{g'}(\xi) \frac{\sqrt{-y}}{y} \right\} dy \quad (\text{C.32})$$

 $f_{g,8}$

$$\frac{f_{g,8}}{y} = 2c_2 \frac{\sqrt{-y(1+y)}}{y^2(1+y)} \left(\frac{1+4y}{1+y} \arctan \sqrt{\frac{-y}{1+y}} + \frac{3+4y}{y} \arctan \sqrt{\frac{1+y}{-y}} \right) \quad (\text{C.33})$$

$$\int dy \frac{f_{g,8}}{y} \frac{F^g(\xi(1+2y))}{2\xi(1+y)} \approx \frac{c_2}{\xi} \int \left\{ F^g(\xi) \left[2\pi \frac{\sqrt{-y}}{y^2} + \frac{3}{y} - 3\pi \frac{\sqrt{-y}}{y} - 8 \right] + 2\xi F^{g'}(\xi) \left[2\pi \frac{\sqrt{-y}}{y} + 3 \right] \right\} dy \quad (\text{C.34})$$

 $f_{g,9}$

$$\frac{f_{g,9}}{y} = -\frac{\arctan^2 \sqrt{\frac{-y}{1+y}}}{2y^2(1+y)} \left((7+4y)c_1 - 2\frac{1+2y-2y^2}{1+y}c_2 \right) \quad (\text{C.35})$$

$$\int dy \frac{f_{g,9}}{y} \frac{F^g(\xi(1+2y))}{2\xi(1+y)} \approx \frac{1}{2\xi} \int \left\{ F^g(\xi) \left[\frac{1}{y} \left(\frac{7}{2}c_1 - c_2 \right) - \frac{8}{3}c_1 + \frac{1}{3}c_2 \right] - [F^g(\xi) - 2\xi F^{g'}(\xi)] \left[\frac{7}{2}c_1 - c_2 \right] \right\} dy \quad (\text{C.36})$$

 $f_{g,10}$

$$\frac{f_{g,10}}{y} = -\frac{\arctan^2 \sqrt{\frac{1+y}{-y}}}{2y^2(1+y)} \left((3-4y)c_1 - 2c_2 \frac{3+6y+2y^2}{y} \right) \quad (\text{C.37})$$

$$\begin{aligned}
\int dy \frac{f_{g,10}}{y} \frac{F^g(\xi(1+2y))}{2\xi(1+y)} \approx & -\frac{1}{4\xi} \int \left\{ F^g(\xi) \left[\frac{3\pi^2}{y^2} \left(\frac{1}{4}c_1 - c_2 \right) - 3\pi \frac{\sqrt{-y}}{y^2} (c_1 - 4c_2) \right. \right. \\
& - \frac{1}{y} \left[\left(3 + \frac{5\pi^2}{2} \right) c_1 - 4(3 + \pi^2) c_2 \right] \\
& \left. \left. + \frac{\sqrt{-y}}{y} \left(\frac{21\pi}{2}c_1 - 22\pi c_2 \right) + 5c_1 - 4\pi^2 c_2 \right] \right. \\
& + 2\xi F^{g'}(\xi) \left[\frac{3\pi^2}{y} \left(\frac{1}{4}c_1 - c_2 \right) - 3\pi \frac{\sqrt{-y}}{y} (c_1 - 4c_2) \right. \\
& \left. \left. - \left(3 + \frac{7\pi^2}{4} \right) c_1 + 2(6 - \pi^2) c_2 \right] \right\} dy
\end{aligned} \tag{C.38}$$

$f_{g,11}$

$$\frac{f_{g,11}}{y} = \frac{2}{y} a_1(y) \ln(-y) \tag{C.39}$$

whith $a_1(y)$ given by

$$\begin{aligned}
a_1(y) = \frac{c_1}{4} \left(5 + 16y - \frac{6}{1+y} + \frac{1}{(1+2y)^2} - \frac{5}{1+2y} \right) \\
- \frac{c_2}{2} \left(2 + \frac{3}{y} + 8y - \frac{1}{1+y} \right). \tag{C.40}
\end{aligned}$$

$$\begin{aligned}
\int dy \frac{f_{g,11}}{y} \frac{F^g(\xi(1+2y))}{2\xi(1+y)} \approx & \frac{1}{2\xi} \int \left\{ F^g(\xi) \left[-3c_2 \frac{\ln(-y)}{y^2} \right. \right. \\
& \left. \left. - \frac{\ln(-y)}{y} \left(\frac{5c_1}{2} + c_2 \right) + \ln(-y)(14c_1 - 9c_2) \right] \right. \\
& - [F^g(\xi) - 2\xi F^{g'}(\xi)] \left[-3c_2 \frac{\ln(-y)}{y} \right. \\
& \left. \left. - \ln(-y) \left(\frac{5c_1}{2} + c_2 \right) \right] \right\} dy
\end{aligned} \tag{C.41}$$

$f_{g,12}$

$$\frac{f_{g,12}}{y} = \frac{2}{y} a_1(-1-y) \ln(1+y) \tag{C.42}$$

$$\int dy \frac{f_{g,12}}{y} \frac{F^g(\xi(1+2y))}{2\xi(1+y)} \approx \frac{1}{2\xi} \int \left\{ F^g(\xi) \left[\frac{1}{y}(3c_1 - c_2) - \frac{1}{2}(14c_1 - 21c_2) \right] + 2\xi F^{g'}(\xi)(3c_1 - c_2) \right\} dy \quad (\text{C.43})$$

$f_{g,13}$

$$\frac{f_{g,13}}{y} = \frac{2}{y} a_2(y) \text{Li}_2(1+2y) \quad (\text{C.44})$$

with $a_2(y)$ given by

$$a_2(y) = \frac{c_1}{8} \left(12 + \frac{9}{y} + 64y - \frac{2}{(1+y)^2} + \frac{21}{1+y} - \frac{4}{1+2y} \right) - \frac{c_2}{4} \left(8 + \frac{3}{y^2} + \frac{11}{y} + 32y - \frac{2}{(1+y)^2} + \frac{9}{1+y} \right). \quad (\text{C.45})$$

$$\begin{aligned} \int dy \frac{f_{g,13}}{y} \frac{F^g(\xi(1+2y))}{2\xi(1+y)} \approx \frac{1}{2\xi} \int \left\{ F^g(\xi) \left[\frac{1}{y^2} \left(\frac{3\pi^2}{8} c_1 - \frac{11\pi^2}{12} c_2 \right) \right. \right. \\ + \frac{1}{y} \left[\frac{1}{8} (36 + 6\pi^2) c_1 - \left(11 + \frac{\pi^2}{3} \right) c_2 \right] \\ - \frac{\ln(-2y)}{y} \left(\frac{9}{2} c_1 - 11c_2 \right) - \ln(-2y) \left(\frac{9}{2} c_1 - 7c_2 \right) \\ + \left(27 + \frac{14\pi^2}{3} \right) \frac{c_1}{4} - (3 + 2\pi^2) \frac{c_2}{2} \left. \right] \\ - [F^g(\xi) - 2\xi F^{g'}(\xi)] \left[\frac{1}{y} \left(\frac{3\pi^2}{8} c_1 - \frac{11\pi^2}{12} c_2 \right) \right. \\ - \ln(-2y) \left(\frac{9}{2} c_1 - 11c_2 \right) \\ + \left. \left. \left[\frac{1}{8} (36 + 9\pi^2) c_1 - \frac{1}{4} (44 + 5\pi^2) c_2 \right] \right] \right\} dy \quad (\text{C.46}) \end{aligned}$$

$f_{g,14}$

$$\frac{f_{g,14}}{y} = \frac{2}{y} a_2(-1-y) \text{Li}_2(-1-2y) \quad (\text{C.47})$$

$$\begin{aligned}
\int dy \frac{f_{g,14}}{y} \frac{F^g(\xi(1+2y))}{2\xi(1+y)} \approx \int \left\{ F^g(\xi) \left[\frac{f_{g,14}}{y} \approx \frac{1}{y^2} \frac{\pi^2}{8} \left(\frac{7}{2}c_1 - 3c_2 \right) \right. \right. \\
+ \frac{1}{y} \left[\frac{c_1}{4} \left(42 \ln 2 + \frac{19\pi^2}{4} \right) - c_2 \left(9 \ln 2 + \frac{4\pi^2}{3} \right) \right] \\
+ \left(1 + \frac{\pi^2}{4} \right) \left(\frac{21c_1}{4} - \frac{9c_2}{2} \right) + \ln 2(18c_1 - 23c_2) \left. \right] \\
- [F^g(\xi) - 2\xi F^{g'}(\xi)] \left[\frac{1}{y} \frac{\pi^2}{8} \left(\frac{7}{2}c_1 - 3c_2 \right) \right. \\
+ \left. \left. \left[\frac{c_1}{4} \left(42 \ln 2 + \frac{19\pi^2}{4} \right) - c_2 \left(9 \ln 2 + \frac{4\pi^2}{3} \right) \right] \right] \right\} dy
\end{aligned} \tag{C.48}$$

Terms $\propto 1/y^3$

Throughout the above, there have been components of a few of the terms (specifically, terms $f_{g,5}$, $f_{g,8}$, $f_{g,10}$, $f_{g,13}$, and $f_{g,14}$) which diverge as $1/y^3$. These components were not included in the above analysis, since if one combines all these $1/y^3$ components and expands around $y = 0$, there are cancellations leading to the strongest divergence becoming $1/y^2$. This is advantageous since if one is to properly account for the $1/y^3$ divergence, one would need to evaluate the GPD's second derivative, but for $1/y^2$ divergences, the first derivative is sufficient, which saves computational time. If we add the $1/y^3$ components and expand, we are left with,

$$\begin{aligned}
\frac{f_{g,y^3}}{y} \approx c_1 \left[\frac{1}{y^2} \left(\frac{\pi^2}{12} + \ln 2 \right) + \frac{1}{y} \left(\frac{1}{2} - \ln 2 - \frac{\pi^2}{8} \right) + \frac{1}{6} (\pi^2 - 6 + 8 \ln 2) \right] \\
+ c_2 \left[\frac{1}{y^2} \left(\frac{\pi^2}{12} + \ln 2 \right) + 3 \frac{\ln(-y)}{y^2} + 2\pi \frac{\sqrt{-y}}{y^2} - \frac{1}{y} \left(\frac{\pi^2}{2} - \frac{1}{2} + \ln 2 \right) \right. \\
\left. - 3 \frac{\ln(-y)}{y} - \frac{13\pi}{5} \frac{\sqrt{-y}}{y} + 4 \ln(-y) + \frac{11\pi^2}{12} - 1 + \frac{4}{3} \ln 2 \right]
\end{aligned} \tag{C.49}$$

We end, including the GPD, with

$$\begin{aligned}
\int dy \frac{f_{g,y^3} F^g(\xi(1+2y))}{y 2\xi(1+y)} \approx \frac{c_1}{2\xi} \int \left\{ F^g(\xi) \left[\frac{1}{y^2} \left(\frac{\pi^2}{12} + \ln 2 \right) + \frac{1}{y} \left(\frac{1}{2} - \ln 2 - \frac{\pi^2}{8} \right) \right. \right. \\
\left. \left. + \frac{1}{6} (\pi^2 - 6 + 8 \ln 2) \right] \right. \\
\left. - [F^g(\xi) - 2\xi F^{g'}(\xi)] \left[\frac{1}{y} \left(\frac{\pi^2}{12} + \ln 2 \right) \right. \right. \\
\left. \left. + \frac{1}{8} (4 - 8 \ln 2 - \pi^2) \right] \right. \\
+ \frac{c_2}{2\xi} F^g(\xi) \left[\frac{1}{y^2} \left(\frac{\pi^2}{12} + \ln 2 \right) + 3 \frac{\ln(-y)}{y^2} + 2\pi \frac{\sqrt{-y}}{y^2} \right. \\
\left. - \frac{1}{y} \left(\frac{\pi^2}{2} - \frac{1}{2} + \ln 2 \right) - 3 \frac{\ln(-y)}{y} - \frac{13\pi}{5} \frac{\sqrt{-y}}{y} \right. \\
\left. + 4 \ln(-y) + \frac{11\pi^2}{12} - 1 + \frac{4}{3} \ln 2 \right] \\
\left. - [F^g(\xi) - 2\xi F^{g'}(\xi)] \left[\frac{1}{y} \left(\frac{\pi^2}{12} + \ln 2 \right) + 3 \frac{\ln(-y)}{y} \right. \right. \\
\left. \left. + 2\pi \frac{\sqrt{-y}}{y} - 3 \ln(-y) - \frac{1}{2} (\pi^2 - 1 + 2 \ln 2) \right] \right\} dy
\end{aligned} \tag{C.50}$$

C.2 Quark Amplitude

As one can see by comparing T_q with T_g , Eqs. (3.34) and (3.35), along with f_q and f_g , Eqs. (3.36) and (3.37), the quark calculation will be simpler than the NLO gluon one, e.g. there is no divergence greater than $1/y$, unlike the gluon case. Despite this simplification, we still perform the integration using the same method, i.e. splitting the integration into 3 regions, performing the integration in the middle region analytically. We again expand in the middle region and keep terms up to $\mathcal{O}(\delta)$. Additionally, we can refer back to the same integrals given in Section C.1; since we do not have a factor of $1/(x+\xi)$, when we expand the GPD, we simply have

$$F^g(x) = F^g(\xi(1+2y)) \approx F^g(\xi) + 2\xi F^{g'}(\xi) y. \tag{C.51}$$

Fortunately, upon performing the expansion, all terms $\propto F^{q'}(\xi)$ cancel, so we do not need to evaluate the derivative of the quark GPDs in order to obtain our results.

Since the expression for f_q is so much simpler than f_g , there is no need to expand and integrate each term individually, we instead look at it as a whole. If we expand f_q , Eq. (3.36), around $y = 0$, and include Eq. (C.51), we obtain

$$\begin{aligned}
F^q(x)f_q(y) &\approx F^q(\xi) \left(\log \frac{4m^2}{\mu_F^2} - 1 \right) (\log[-y] - 1) - \frac{13\pi^2}{48} \left(\frac{F^q(\xi)}{y} + F^q(\xi) + 2\xi F^{q'}(\xi) \right) \\
&\quad + 2 \log(2)F^q(\xi) + \log[-y]F^q(\xi) + \log^2[-y]F^q(\xi) + \frac{\pi^2 F^q(\xi)}{8y} + \frac{7\pi^2 F^q(\xi)}{48y} \\
&\quad + \frac{1}{8} [12F^q(\xi) + 3\pi^2 F^q(\xi) - 12 \log[-2y]F^q(\xi) + 2\pi^2 \xi F^{q'}(\xi)] \\
&\quad + \frac{1}{48} [13\pi^2 F^q(\xi) + 168 \log(2)F^q(\xi) + 14\pi^2 \xi F^{q'}(\xi)]
\end{aligned} \tag{C.52}$$

We see that the terms containing the derivative of the GPD cancel, along with some other terms, leaving us with (remembering that this is the entire integrand)

$$\begin{aligned}
&\int F^q(x)f_q(y)dy \approx \\
&\int F^q(\xi) \left\{ \log^2[-y] + \log[-y] \left(\log \frac{4m^2}{\mu_F^2} - \frac{3}{2} \right) + 4 \log(2) - \log \frac{4m^2}{\mu_F^2} + \frac{5}{2} + \frac{3}{8}\pi^2 \right\} dy
\end{aligned} \tag{C.53}$$